

# Gravitational Collapse in Anti-de Sitter Spacetime

by

Bradley Stuart Cownden

A Thesis submitted to the Faculty of Graduate Studies of  
The University of Manitoba  
in partial fulfillment of the requirements for the degree of

DOCTOR OF PHILOSOPHY

Department of Physics and Astronomy  
University of Manitoba  
Winnipeg

© 2020 by Bradley Stuart Cownden

*For Kyla.*

## Acknowledgments

I would like to thank the University of Winnipeg's Physics Department for fostering a supportive and intellectually challenging environment during my graduate studies. I am a better researcher and person for knowing the faculty, staff, and students there.

I would also like to specifically thank my supervisor, Andrew Frey, for guiding my development as a researcher through both my MSc and PhD. Because of him, I have been lucky enough to pursue my dream of studying physics.

My family – mother Lori, father Kevin, and brothers Alex, Matthew, and Jon – have been the bedrock of my support for my entire life, and I am eternally grateful and humbled by their encouragement and patience during my studies. I am also incredibly lucky to have many amazing friends that have always believed in me. Dani, Becky, and Danielle: thank you from the bottom of my heart.

Most of all, I would like to thank my wife Kyla, for the faith she has in me and for the many ways that she lights up my life.

## Abstract

The gravitational collapse of a minimally coupled scalar field in  $(d + 1)$ -dimensional Anti-de Sitter spacetime is examined via a collection of manuscripts that are, or are in the process of, being published. First, the results of the numerical evolution of the 5-dimensional nonlinear Einstein equations are used to construct a phase diagram of collapse behaviours, taking the mass and width of the initial profile as parameters. Next, we test the limits of a family of perturbative solutions for massless scalars with static boundary conditions in  $\text{AdS}_4$ . Finally, we derive set of flow equations for the time evolution of a massive scalar field in the perturbative description of  $\text{AdS}_4$  with time-dependent boundary conditions.

# Contents

<b>Acknowledgments</b>	<b>i</b>
<b>Abstract</b>	<b>ii</b>
<b>Table of Contents</b>	<b>iii</b>
<b>1 Introduction</b>	<b>1</b>
1.1 The AdS/CFT Correspondence . . . . .	2
1.1.1 Extra Dimensions In Gauge Theories . . . . .	3
1.1.2 The $\text{AdS}_5 \times S^5$ Duality . . . . .	4
1.2 The Gauge/Gravity Dictionary . . . . .	5
1.3 Gravitational Collapse of Scalar Fields . . . . .	11
1.3.1 Scalar Fields in Holographic $\text{AdS}_{d+1}$ . . . . .	13
1.3.2 Nonlinear Stability & Instability . . . . .	17
1.3.3 A Perturbative Description . . . . .	19
1.3.4 The Landscape of Solutions . . . . .	20
1.3.5 Driven Scalars . . . . .	21
1.4 Summary . . . . .	22
<b>2 Nonlinear Evolution of Massive Scalar Fields in Anti-de Sitter Spacetime</b>	<b>24</b>
2.1 Contributions of Authors . . . . .	24
2.2 Introduction . . . . .	27
2.3 Review . . . . .	29

2.3.1	Massive scalars, stability, and time scales . . . . .	30
2.3.2	Methods . . . . .	34
2.4	Phase Diagram of Stability . . . . .	35
2.4.1	Metastable versus unstable initial data . . . . .	37
2.4.2	Irregular behaviors . . . . .	42
2.5	Spectral analysis . . . . .	48
2.5.1	Dependence on mass . . . . .	49
2.5.2	Spectra of different behaviors . . . . .	51
2.5.3	Evolution of spectra . . . . .	53
2.6	Discussion . . . . .	55
2.A	Convergence Testing . . . . .	58
<b>3</b>	<b>Perturbative Stability of Massless Scalars in <math>\text{AdS}_4</math></b> . . . . .	<b>64</b>
3.1	Contributions of Authors . . . . .	64
3.2	Introduction . . . . .	67
3.3	Minimally Coupled Scalar Fields in $\text{AdS}_{d+1}$ . . . . .	69
3.3.1	Linearized Solutions . . . . .	70
3.3.2	Two-Time Formalism . . . . .	71
3.4	Quasi-periodic Solutions in $\text{AdS}_4$ . . . . .	73
3.4.1	Persistence at Large $j_{max}$ . . . . .	74
3.5	High Temperature Perturbations . . . . .	75
3.5.1	Projections at Constant $\alpha_1$ . . . . .	76
3.5.2	Projections at Constant Temperature . . . . .	79
3.5.3	Building High-Temperature Solutions . . . . .	79
3.6	Time Evolution of Quasi-Periodic Solutions . . . . .	83
3.6.1	Low-temperature QP data . . . . .	83
3.6.2	High-Temperature QP Data . . . . .	85
3.7	Discussion . . . . .	88

3.A	Seeding Methods For Non-Linear Solvers . . . . .	92
3.B	Auxiliary Integrals For Calculating the $T, R, S$ Coefficients . . . . .	93
3.C	Frequency of Solution Checking . . . . .	95
<b>4</b>	<b>Perturbative Descriptions of Driven Instabilities in AdS</b>	<b>97</b>
4.1	Introduction . . . . .	98
4.2	Source Terms and Boundary Conditions . . . . .	100
4.3	Resonances From Normalizable Solutions . . . . .	106
4.3.1	Naturally Vanishing Resonances: $(+++)$ and $(+--)$ . . . . .	106
4.3.2	Non-vanishing Resonance: $(++-)$ . . . . .	108
4.4	Resonances From Non-normalizable Modes . . . . .	109
4.4.1	Two Non-normalizable Modes with Equal Frequencies . . . . .	111
4.4.2	Special Values of Non-normalizable Frequencies . . . . .	114
4.4.3	Integer Plus $\chi$ . . . . .	119
4.5	Discussion . . . . .	124
4.A	Derivation of Source Terms For Massive Scalars . . . . .	126
4.B	Two Non-normalizable Modes with Equal Frequencies . . . . .	130
<b>5</b>	<b>Conclusion</b>	<b>133</b>
<b>Bibliography</b>		<b>147</b>

# List of Figures

1.1	Horizon size and horizon formation time for a massive scalar	21
2.1	Horizon formation time vs. amplitude for classes of initial data	31
2.2	Stability phase diagram	36
2.3	Fitting the leading coefficient of $t_H = a\epsilon^{-p} + b$ as a function of initial data width	38
2.4	Horizon formation times for metastable initial data	39
2.5	Horizon formation times for irregular initial data	43
2.6	Evidence for chaotic evolution	45
2.7	Phase space trajectories for irregular and unstable initial data	46
2.8	Mass density profiles for chaotic systems	48
2.9	Energy spectra of best fit gaussians to the $j = 0$ eigenmode for various masses	50
2.10	Initial energy spectra for each type of initial data	51
2.11	Evolution of the energy spectra	52
2.12	Late-time spectra	54
2.A.1	Comparison of order of convergence of $\phi, M, A, \delta$ as a function of time for $\mu = 0.5$ over two base resolutions	59
2.A.2	Order of convergence for $\phi, M, A, \delta$ as a function of time for $\mu = 15$ at nearby amplitudes	60
2.A.3	Order of convergence for $\phi, M, A, \delta$ as a function of time for $\mu = 0$ at nearby amplitudes	60
2.A.4	Order of convergence for $\phi, M, A, \delta$ as a function of time for $\mu = 5$ at nearby amplitudes	61

2.A.5	Order of convergence for $\phi, M, A, \delta$ as a function of time for $\mu = 1$ at nearby amplitudes . . . . .	62
2.A.6	Order of convergence for $\phi, M, A, \delta$ as a function of time for $\mu = 20$ at nearby amplitudes . . . . .	62
3.1	Energy spectra for various low- $T$ QP solutions . . . . .	75
3.2	High temperature solutions resulting from projecting back to the QP solution surface at various frequencies . . . . .	77
3.3	Energy spectra resulting from perturbing the same QP solution at differing frequencies	78
3.4	Finding high temperature QP solutions using repeated perturbations with regular projections back to the QP surface . . . . .	80
3.5	Constructing high temperature solutions by hand . . . . .	81
3.6	Evolution of QP solutions at low temperature . . . . .	84
3.7	Taking the spectrum of a QP solution during evolution to use as a seed to find new QP solutions . . . . .	85
3.8	The evolution of a padded QP solution . . . . .	86
3.9	Examining the energy per mode during the evolution of a $T \simeq 5.4$ QP solution . .	87
3.10	Evolution of the energy spectrum and Ricci scalar for a $T \simeq 5.4$ QP solution . .	87
3.11	Evolution of the spectrum of a $T \simeq 5.4$ QP solution that has been padded with 100 modes . . . . .	88
3.12	Comparison between a attractor solution with $j_{max} = 200$ and the evolution of a $j_{max} = 100, T \simeq 5.4$ solution that has been padded by 100 modes . . . . .	88
3.A.1	Fitting the tail of the $j_{max} = 175$ spectrum to construct a seed for $j_{max} = 200$ at fixed $\alpha_1 = 0.2$ . Also included is actual QP spectrum for $j_{max} = 200$ . . . . .	93
3.A.2	Comparison of seed values to known QP solutions and exponential fitting . . . . .	94
3.C.1	Comparison of spectra and temperatures for different projection frequencies between $j_{max} = 50$ and $j_{max} = 150$ solutions . . . . .	95

4.1	Evaluating non-vanishing resonances for normalizable modes over a range of $m^2$ values . . . . .	110
4.2	Source term for two equal frequency, non-normalizable modes when $m^2 = 0$ . . . . .	113
4.3	Source term for two equal frequency, non-normalizable modes when $m^2 = -1$ . . . . .	114
4.4	Source term for two non-normalizable modes whose frequencies add to an integer when $m^2 = -1$ and $\bar{\omega}_1 + \bar{\omega}_2 = 4$ . . . . .	118
4.5	Source term for two non-normalizable modes whose frequencies add to an integer when $m^2 = 0$ for $\bar{\omega}_1 + \bar{\omega}_2 = 4$ and $8$ . . . . .	119
4.6	Source term for two non-normalizable modes with frequencies $\omega_\alpha = 2\alpha + \chi$ over various choices of $\chi$ . . . . .	122

# List of Tables

2.1	Best fit parameters for metastable data . . . . .	40
2.2	Best fit Lyapunov coefficients . . . . .	46
3.1	Attractor solution temperature for different truncation values with constant projection frequency . . . . .	78

# 1 Introduction

As experimental research into quantum information, condensed matter, and nuclear physics continues to reach new levels of precision, progress in developing theoretical predictions in these fields is hindered by a fundamental problem: in strong coupling regimes, the perturbative methods that underpin theories such as Quantum Electrodynamics become invalid. This is because such systems are highly nonlinear. While some progress is possible by employing numerical schemes such as lattice approximations, analytical results remain beyond our current mathematical understanding. In order to make progress, a new paradigm was required. By considering different coupling limits of a single string theory, [1] established a holographic description between strongly-coupled gauge theories and weakly-coupled gravitational theories in one higher dimension. Since its inception, this duality has been further developed into a dictionary that relates the fields in the gravitational theory to operators in the gauge theory. The Anti-de Sitter/Conformal Field Theory (AdS/CFT) correspondence allows strongly-coupled quantum processes to be reliably examined via geometric quantities in the dual theory. This duality has become a standard tool for theoretical physicists studying all kinds of dynamic processes in quantum theories, including the out-of-equilibrium dynamics of quantum theories at strong coupling.

The goal of this thesis is to leverage the AdS/CFT correspondence to study the dynamics of strongly coupled quantum theories through their dual description as a weakly coupled gravitational theory. To do so, we focus on minimally coupled scalar fields in Einstein-Hilbert gravity on AdS backgrounds. Existing entries in the gauge/gravity dictionary will motivate the systems that are considered, and existing literature will point to areas within the topic that have yet to be explored. The nonlinear stability of the theory will be studied via both numerical and analytical methods.

We will see that gravitational collapse in the bulk theory signals a phase transition in the dual gauge theory, and so examining the dynamics of the collapse is tantamount to understanding time dependent processes in the boundary theory.

This thesis embodies the results of three manuscripts that either have been, or are about to be, submitted for publication. In chapter 2, we examine the limits of the nonlinear stability of  $\text{AdS}_5$  by examining the range of behaviours exhibited during nonlinear evolution by differing initial data with static boundary conditions. Next, in chapter 3, we examine quasi-periodic solutions to the perturbative description of a massless scalar field in  $\text{AdS}_4$ , again with static boundary conditions. Finally, in chapter 4 we consider the addition of a time-dependent source term on the conformal boundary of the gravitational theory and derive the renormalization flow equations for the first non-trivial order in the small-amplitude expansion. A discussion of the results follows in chapter 5.

However, before utilizing the correspondence to study any particular process, we first review the main tenet of the gauge/gravity duality and its consequences: that there exists a fundamental relationship between a conformal field theory in  $d$ -dimensions and a gravitational theory in  $(d+1)$ -dimensions.

## 1.1 The AdS/CFT Correspondence

It was shown by [1] that a non-perturbative correspondence existed between superconformal field theories and supergravity theories on various spacetimes. Although originally conjectured from the perspective of string theory, more modern reviews of the gauge/gravity duality establish a gravitational theory as arising from the strong coupling limit of a gauge theory; see [2] for a review. We will use this paradigm to heuristically motivate the duality, as well as introduce relevant relationships between quantities in either theory.

### 1.1.1 Extra Dimensions In Gauge Theories

Although [1] was the first to establish explicitly a correspondence between a gravitational theory in  $(d + 1)$ -dimensional AdS and a conformal field theory in  $d$ -dimensions, the concept of a holographic relationship between a gauge theory and a gravitational theory in one higher dimension was conjectured earlier by [3] and [4] without relying solely on string theory.

For most gauge theories, there is a running of the coupling that dictates the evolution of the couplings with energy. Therefore, the physics of the theory is local with respect to an extra dimension, the energy. However, since many gauge theories suffer UV divergences at large energies, the size of the extra dimension may be limited. In contrast, some supersymmetric theories have vanishing beta functions; therefore, there is no running of the coupling. In this case, the energy scale is arbitrary and the extra dimension of the theory has no bound.

The vanishing of the beta function also indicates that the conformal invariance of the theory is unbroken; conformal invariance requires (among other things) that the theory remain invariant under rigid scale transformations by a unitless constant  $a$ , such that  $x^\mu \rightarrow ax^\mu$ . Interpreting the energy scale as an extra dimension,  $r$ , we require it to transform in the same way as energy, so that  $r \rightarrow r/a$ . The most generic metric that also obeys Poincaré plus scale symmetries is

$$ds^2 = \frac{a^2}{z^2} (\eta_{\mu\nu} dx^\mu dx^\nu + dz^2), \quad (1.1)$$

where  $z = a^2/r$ . This is precisely the metric for the Poincaré patch of Anti-de Sitter space with characteristic length  $a$ .

More than being an *a posteriori* observation, the gauge/gravity correspondence is in fact a much deeper and more specific relationship. The derivation of the duality is thoroughly covered from the full string theory perspective in, among others, [1, 2, 5, 6]. For now, let us establish the duality that will be most applicable to us: the duality between type IIB supergravity on  $\text{AdS}_5 \times \text{S}^5$  and  $\mathcal{N} = 4$  supersymmetric Yang-Mills theory in  $(3 + 1)$ -dimensions.

### 1.1.2 The AdS<sub>5</sub>×S<sup>5</sup> Duality

Consider a stack of  $N$  coincident D3-branes in type IIB string theory (ten Minkowski dimensions), each of which couple to gravity with strength  $g_s$ . At weak coupling,  $g_s N \ll 1$ , there are closed string states as well as open strings that end on the branes and have an  $SU(N)$  super-Yang-Mills effective action. At strong coupling, however, the branes curve the background and source an extremal black-brane geometry [7], whose metric is

$$ds^2 = f(r)^{-1/2} \eta_{\mu\nu} dx^\mu dx^\nu + f(r)^{1/2} (dr^2 + r^2 d\Omega_5^2) \quad \text{with} \quad f(r) = 1 + \frac{4\pi g_s N \ell_s^4}{r^4}, \quad (1.2)$$

where the  $x^\mu$  span the worldvolume of the D3-branes,  $d\Omega_5^2$  is the metric of the unit 5-sphere, and  $\ell_s$  is the length of the string.

Now we take the low-energy limit of the theories at either coupling limit. At weak coupling, the open strings decouple from the closed strings, resulting in an  $SU(N)$  super-Yang-Mills gauge theory on the brane worldvolume. In the  $g_s N \gg 1$  case, the low-energy limit corresponds to the near-horizon limit,  $r \rightarrow 0$ . In this limit, the 10D metric factors into the product AdS<sub>5</sub>×S<sup>5</sup>. To see this, we define  $\ell \equiv (4\pi g_s N)^{1/4} \ell_s$ , so that  $f^{1/2}(r) \rightarrow \ell^2/r^2$  in the near-horizon limit and (1.2) becomes

$$ds^2 = \frac{r^2}{\ell^2} \eta_{\mu\nu} dx^\mu dx^\nu + \frac{\ell^2}{r^2} dr^2 + \ell^2 d\Omega_5^2. \quad (1.3)$$

Note that the branes are now located at the bottom of the infinite throat. Any states near the horizon will be redshifted to low energies and any states in the asymptotic region will decouple from states near the black branes; all that remains are closed string states, i.e. supergravity, on an asymptotically AdS<sub>5</sub> background. This motivates the duality we will examine in detail: the one between scalar fields in AdS<sub>5</sub>×S<sup>5</sup> and a supersymmetric  $SU(N)$  Yang-Mills gauge theory on the boundary of AdS<sub>5</sub>.

Given that we now know what string theory we are working with, we can more directly relate the dimensionless parameters of the string theory (i.e. the string coupling  $g_s$  and AdS scale in string

units,  $\ell/\ell_s$ ) to the dimensionless parameters of the CFT (i.e. the Yang-Mills coupling  $g_{YM}$  and colour number  $N$ ). By examining the D3-brane Lagrangian, we are able to relate  $g_{YM}$  and  $g_s$  through  $4\pi g_s = g_{YM}^2$ . Altogether,

$$4\pi g_s = g_{YM}^2 \sim \frac{\lambda}{N} \quad \text{and} \quad \frac{\ell}{\ell_s} = (4\pi g_s N)^{1/4} \sim \lambda^{1/4}, \quad (1.4)$$

where  $\lambda$  is the 't Hooft coupling  $\lambda \equiv g_s N = g_{YM}^2 N$ . To remove stringy corrections to the geometry,  $\ell/\ell_s \gg 1$  so that the AdS length is much larger than the string length. Furthermore, string interactions are suppressed when  $g_s \ll 1$ . Thus, the bulk theory approaches classical Einstein-Hilbert gravity when  $N \gg \lambda \gg 1$ .

By considering other superstring avatars, such as M-theory<sup>1</sup>, we are able to establish similar dualities between gravitational and conformal field theories. In particular, the M-theory equivalent of D2-branes, M2-branes, are used – along with corresponding coupling limits – to establish a duality between a gravitational bulk theory on  $\text{AdS}_4 \times S^7$  and a CFT in  $(2+1)$ -dimensions [1]. In fact, many such dualities can be constructed through applying different compactifications and/or sources in the extra dimensions, each of which describes a different type of CFT on the boundary. For a review of other types of holographic constructions, see e.g. [9, 10].

## 1.2 The Gauge/Gravity Dictionary

With the existence of the duality now motivated, we turn to what kind of predictions arise from the correspondence. In particular, we wish to establish what physical quantities in either theory can be related through the AdS/CFT correspondence. In fact, many such relations arose from efforts to find counterexamples to the correspondence in the hopes of disproving it. Instead, each attempt confirmed the AdS/CFT correspondence and became an entry in the so-called dictionary. Here we will provide a few example cases to motivate how quantities on either side of the correspondence can be related.

---

<sup>1</sup>M-theory is the strong-coupling limit of type IIA superstring theory on 11D spacetime, and can be mapped to the other 10D superstring theories through choices of compactifications and length/coupling dualities [8].

## Symmetries

Consider the symmetries present in the  $\text{AdS}_5 \times \text{S}^5$  bulk theory. A  $(p+2)$ -dimensional Anti-de Sitter space can be presented by the hyperboloid  $X_0^2 + X_{p+2}^2 - \sum_{i=1}^{p+1} X_i^2 = R^2$  in a  $(p+3)$ -dimensional space with the metric

$$ds^2 = -dX_0^2 - dX_{p+2}^2 + \sum_{i=1}^{p+1} dX_i^2. \quad (1.5)$$

The choice of  $X_0 = R \cosh \rho \cos \tau$ ,  $X_{p+2} = R \cosh \rho \sin \tau$ , and  $X_i = R \sinh \rho \Omega_i$  with  $i = 1, \dots, p+1$ ,  $0 \leq \rho$ ,  $0 \leq \tau \leq 2\pi$ , and  $\sum_i \Omega_i = 1$  covers the hyperboloid exactly once, and is known as global coordinates. In these coordinates, the metric on  $\text{AdS}_{p+2}$  is

$$ds^2 = R^2 (-\cosh^2 \rho d\tau^2 + d\rho^2 + \sinh^2 \rho d\Omega^2). \quad (1.6)$$

A common coordinate redefinition of  $\tan x = \sinh \rho$  maps spatial infinity to  $x = \pi/2$ , and allows (1.6) to be written as

$$ds^2 = \frac{R^2}{\cos^2 x} (-d\tau^2 + dx^2 + \sin^2 x d\Omega^2). \quad (1.7)$$

Another common parameterization of AdS is a set of coordinates that cover half of the hyperboloid (1.5), known as Poincaré coordinates. These set  $X_0 = (1 + z^2(R^2 + \vec{x}^2 - t^2))/2z$ ,  $X_{p+2} = Rzt$ ,  $X^{p+1} = (1 - z^2(R^2 - \vec{x}^2 + t^2))/2z$ , and  $X^i = Rzx^i$ , with  $i = 1, \dots, p$ ,  $z > 0$ , and  $\vec{x} \in \mathbb{R}^p$ . Thus, the metric of  $\text{AdS}_{p+2}$  in the Poincaré patch description is

$$ds^2 = R^2 \left( \frac{d^2 z}{z^2} + z^2 (-dt^2 + d\vec{x}^2) \right). \quad (1.8)$$

From the description as the hyperboloid in (1.5),  $\text{AdS}_{p+2}$  has the isometry  $SO(2, p+1)$ , and is homogeneous and isotropic [6]. The global coordinate representation helps us to interpret the maximal compact subgroup of  $SO(2, p+1)$ ,  $SO(2) \times SO(p+1)$ , as constant translations in  $\tau$  plus

rotations of  $S^p$ . Likewise, the Poincaré coordinates describe the symmetries of AdS in terms of the Poincaré transformation on  $(t, \vec{x})$  plus the dilatation transformation  $(t, \vec{x}, z) \rightarrow (ct, c\vec{x}, c^{-1}z)$  for  $z > 0$ . Finally, invariance under special conformal transformations makes the Poincaré patch description of AdS fully invariant under conformal coordinate transformations.

In particular, a bulk theory on  $\text{AdS}_5 \times S^5$  has  $SO(2, 4) \times SO(6)$  symmetry. The  $\mathcal{N} = 4$  super-Yang Mills theory on the boundary of this space has an  $SO(2, 4)$  isometry from its conformal invariance, as well as  $SU(4) \simeq SO(6)$  R-symmetry that relates the six scalar fields and four fermions of the theory [1]. Therefore, the spatial isometries of the bulk space are interpreted as global symmetries of the boundary theory. Additionally, the supersymmetries inherent in the original type IIB superstring theory remain unbroken by the strong/weak coupling limits. Hence, the gauge/gravity correspondence conserves the symmetries of both theories.

## Observables

Besides matching symmetry groups and relating dimensionless parameters, the AdS/CFT correspondence is able to produce more physically relevant relationships involving observables in either theory. One such concrete example comes from relating the asymptotic behaviour of bulk fields to the expectation values of operators in the boundary theory: a bulk field in Poincaré AdS with metric (1.1) has leading-order value  $\phi^{(0)}$  as  $z \rightarrow 0$  (i.e. as the conformal boundary is approached) and acts as a source for an operator  $\mathcal{O}$  on the boundary. Furthermore, by examining the next-to-leading order contribution to the bulk field,  $\phi^{(1)}$ , it can be shown that the expectation value of the operator is given by  $\langle \mathcal{O} \rangle \propto \phi^{(1)}$  [11]. In § 1.3.1, we use the gauge/gravity duality to calculate the mass dimension of the boundary operator  $\mathcal{O}$ .

Another such example is the quark anti-quark potential in the boundary theory. In the gauge theory, this can be calculated via the Wilson loop  $W(\mathcal{C})$ , where  $\mathcal{C}$  is the closed loop connecting the quark worldlines. The bulk interpretation of the Wilson loop is the extremized proper area of a string worldsheet anchored on  $\mathcal{C}$  and extending into  $z > 0$  [12].

## Entanglement Entropy

A significant utilization of the gauge/gravity duality comes from its unique ability to relate quantum characteristics of the gauge theory to geometric ones in the bulk. Among the most quantum of all characteristics is the spatial distribution of quantum correlations within a system, given by the entanglement entropy. For a given subsystem  $\mathcal{M}$  of a local field theory with reduced density matrix  $\rho_{\mathcal{M}}$ , the entanglement entropy is given by the Von Neumann entropy  $S_{\mathcal{M}} = -\text{Tr} \rho_{\mathcal{M}} \ln \rho_{\mathcal{M}}$ . In practice,  $\mathcal{M}$  is a spatial region that is bounded by the entangling surface  $\partial\mathcal{M}$ .

In the strong coupling limit, calculating the entanglement entropy can be prohibitively difficult. However, using the AdS/CFT correspondence it has been shown that  $S_{\mathcal{M}}$  is given by a quarter of the area of the minimal surface at constant time in the bulk that is anchored on  $\partial\mathcal{M}$  [13]. Further properties of the entanglement entropy were subsequently shown to also have dual geometric descriptions in the bulk [14].

## Partition Functions

Since the underpinning of the AdS/CFT correspondence is taking different limits of the same theory, it is natural that the partition functions of either limit must still agree. We have already seen in § 1.1.2 that the weak coupling limit of the type IIB string theory is supergravity (SUGRA) in the bulk, while the strong coupling limit gives a supersymmetric (SUSY) Yang-Mills gauge theory on the boundary. The gauge/gravity duality allows us to relate the two limits of the partition function:

$$e^{-S_{SUGRA}} \approx Z_{string} \simeq Z_{gauge} = e^{-W_{SUSY}}, \quad (1.9)$$

where  $W$  is the generating functional for connected Green's functions in the gauge theory.

Consider a massive bulk field  $\phi(\vec{x}, z)$  that takes the value  $\phi_0(\vec{x})$  on the conformal boundary. We then solve the bulk equations of motion away from the boundary (i.e.  $z > \epsilon$ ) subject to Dirichlet boundary conditions. The leading term in the epsilon expansion of the bulk field is  $\phi(\vec{x}, z = \epsilon) \sim \epsilon^{\Delta^\pm} \phi_0(\vec{x})$ , where the scaling dimension  $\Delta^\pm$  will be explicitly derived below. By definition,  $S_{SUGRA}$  is extremized

by this solution and so (1.9) becomes [15, 16]

$$\lim_{\epsilon \rightarrow 0} \left( S_{SUGRA} [\phi(\vec{x}, z)] \right) \Big|_{\phi(\vec{x}, \epsilon) \rightarrow \phi_0(\vec{x})} \simeq \left\langle \int d^d x \phi_0(\vec{x}) \mathcal{O}(\vec{x}) \right\rangle_{CFT}, \quad (1.10)$$

where  $\mathcal{O}$  is the corresponding operator in the CFT. We will see that bulk scalar fields play an important role in the dual description of the thermalization of a CFT, as well as being a useful tool to study the nonlinear stability of AdS itself.

## Black Holes

Another important ingredient of the AdS/CFT correspondence was first mentioned in § 1.1.2: black holes. As discussed previously, the weak coupling limit of the  $N$  D3-branes produced an extremal black-brane geometry given by (1.3), which is the Poincaré patch description of AdS. Since the interaction cross-section of the branes with low-energy states in the bulk shrinks to zero, the effective geometry for these states is Anti-de Sitter. When discussing black holes in the AdS/CFT correspondence, we are referring to black holes embedded within an AdS geometry.

The connection between black hole physics and thermodynamics was noted by [17], and has been thoroughly examined since then. For a review of the thermodynamic properties of black holes, see [18–20]. It suffices for our purposes to highlight a few key features of the thermodynamic properties of black holes, and thereby motivate a correspondence between black holes in the bulk theory and a gauge theory in thermal equilibrium on the boundary.

By considering quantum effects near the event horizon, it can be shown that black holes emit particles whose thermal spectrum is equivalent to a black body of temperature [21, 22]

$$T_H = \frac{(\ell^2 + 2r_H^2)}{2\pi r_H \ell^2}, \quad (1.11)$$

where  $r_H$  is the size of the event horizon. When the black hole is placed in a geometry with a conformal boundary, it will be in thermal equilibrium with its Hawking radiation, and a stationary observer at asymptotic infinity will observe a black body spectrum corresponding to the temperature

$T_H$  [23]. The black hole will have positive specific heat, and therefore be thermodynamically stable, for  $\ell \gg r_H$  so that  $T_H \simeq 1/2\pi r_H$  [24].

Now consider the partition function for a thermal system in contact with a heat reservoir at temperature  $\beta^{-1}$ . The quantum partition function involves the trace over the eigenvectors of the Hamiltonian,

$$Z = \text{Tr } e^{-\beta H} = \int dq \langle q | \exp(-\beta H) | q \rangle. \quad (1.12)$$

The trace then reduces to a sum over only the periodic states [25]

$$\text{Tr } e^{-\beta H} = \int dq \int_{q'(0)=q}^{q'(\beta)=q} [dq'] e^{-S_E[q']} = \int [dq]_P e^{-S_E[q]}, \quad (1.13)$$

where  $S_E$  is the Euclidean action. Equivalently, we may sum over all states but impose the periodicity condition  $\tau \sim \tau + \beta$ .

As an example, we place a quantum theory on the background of Schwarzschild black hole in asymptotically flat spacetime. After Wick rotating  $t \rightarrow i\tau$ , the metric is

$$ds^2 = + \left(1 - \frac{2GM}{r}\right) d\tau^2 + \left(1 - \frac{2GM}{r}\right)^{-1} dr^2 + r^2 d\Omega_{d-1}^2. \quad (1.14)$$

Note that within the horizon  $r < 2GM$ , the metric of (1.14) is no longer Euclidean but instead is  $\text{diag}(- - ++)$ , unlike the Lorentz signature metric where the time and radial position change roles without changing the signature. Taking the near-horizon limit, we see that the metric develops a conical singularity. To resolve the singularity at  $r = r_H$ , we require that the Euclidean time be periodic such that  $\tau \sim \tau + 2\pi r_H$  [26]. By matching this condition on  $\tau$  with the one from finite-temperature quantum system, we can see that

$$\left. \begin{array}{l} \text{black hole: } \tau \sim \tau + 2\pi r_H \\ \text{CFT: } \tau \sim \tau + \beta \end{array} \right\} \beta \sim 2\pi r_H \Rightarrow T \sim 1/2\pi r_H. \quad (1.15)$$

Therefore, the temperature of the thermalized CFT is equal to the Hawking temperature of the black hole.

A non-trivial check of this duality comes from a comparison of the entropies of the two systems. In the bulk, the Bekenstein-Hawking relationship relates the entropy of a 5D black hole to the surface area of the horizon [17]

$$S_{BH} = \frac{A}{4G^{(5)}} \sim \frac{r_+^3 \ell^5}{g_s^2 \ell_s^8} \sim \frac{T_H^3 \ell^{11}}{g_s^2 \ell_s^8} \sim N^2 T_H^3 \ell^3, \quad (1.16)$$

where we have used the fact that the gravitational constant scales as  $G^{(d)} \sim g_s^2 \ell_s^{d-2}$  as well as (1.4). On the other hand, the entropy of a 4D gauge theory with temperature  $T_H$  in the limit of weak coupling<sup>2</sup> is

$$S_{YM} \sim N^2 T_H^3 \ell^3. \quad (1.17)$$

This agreement shows that the gauge theory possesses enough states to match the entropy of black holes in AdS<sub>5</sub>.

### 1.3 Gravitational Collapse of Scalar Fields

The picture thus far is this: using the AdS/CFT correspondence, we are able to study strongly-coupled gauge theories through their holographic dual, which is a gravitational theory in Anti-de Sitter space with a conformal boundary. We have also seen that black hole solutions in the bulk correspond to thermal states in the boundary theory, and were able to derive the equilibrium temperature of the thermal system by examining the Hawking temperature of the black hole. These results concern stationary systems; indeed, equilibrium and near-equilibrium dynamics of thermal gauge theories have holographic descriptions that are already understood (see [27], etc. for reviews).

---

<sup>2</sup>In the strong coupling limit, the Yang-Mills degrees of freedom are interacting and the entropy calculation is not straightforward. However, the weak coupling limit can be smoothly interpolated to the strong coupling limit via a numerical factor that does not affect our comparison [2].

But what about the dynamics of the thermalization?

Consider some gauge theory that is subjected to a homogeneous injection of energy on a very short time scale such that it is instantaneously far from equilibrium. The subsequent evolution towards a new equilibrium state is known as a *quench*. Quenches can result in thermal states, meta-stable configurations, or may never equilibrate [28]. For example, the infall of a spherical shell of matter (scalar field) in AdS is used as a model for the quench of a coherent state in a gauge theory. The radial position of the shell in the bulk acts as a scale to measure the typical separation of entangled excitations [29]. As the shell falls towards the origin, one of two things can happen: if the shell has a high enough mass density, a black hole forms which signals the thermalization of the gauge theory; if the shell does not collapse, it can pass through itself and begin expanding. Once the shell reaches the AdS boundary, the matter is reflected (under appropriate boundary conditions) and begins the infall again. This cycle of bounces is the holographic dual of so-called *revivals* in the quantum theory [30, 31], and has been used to help explain results from cold atom experiments [32, 33]. The negative curvature of AdS allows for states that do not immediately thermalize to oscillate around the minimum of an effective potential, undergoing repeated gravitational focusing with each oscillation. Therefore, unlike in asymptotically flat space, thermalization can occur at long times with respect to the light crossing time. One may also wish to investigate other non-equilibrium processes, for example the spontaneous breaking of a discrete symmetry in the boundary CFT. The holographic dual description is the evolution from a bulk black hole to a hairy black hole [34, 35]. However, the focus of the work in this thesis will be to study the dynamics of thermalization from a coherent state via the collapse of a scalar field.

### 1.3.1 Scalar Fields in Holographic AdS<sub>d+1</sub>

To determine the solution for a massive scalar field  $\phi(\vec{x}, z)$  in AdS<sub>d+1</sub> space, we begin with the (non-canonically normalized) bulk action for the free field

$$S[\phi] = -\frac{G^{(d+1)}}{2} \int d^{d+1}x \sqrt{-g} (g^{AB} \partial_A \phi \partial_B \phi + \mu^2 \phi^2) + S_{EH}, \quad (1.18)$$

where  $G^{(d+1)}$  is the  $(d+1)$ -dimensional Newton's constant and  $S_{EH}$  is the Einstein-Hilbert action. We choose Poincaré patch coordinates and use the metric in (1.1) to describe the background geometry. When integrating (1.18) by parts we must be careful to retain any surface terms since, unlike for flat spacetimes, they will not go to zero. With this in mind, we find that

$$S[\phi] = -\frac{G^{(d+1)}}{2} \int d^{d+1}x \sqrt{-g} \phi (-\square + \mu^2) \phi - \frac{G^{(d+1)}}{2} \int_{\partial AdS} d^d x \sqrt{-\gamma} g^{zB} \phi \partial_B \phi, \quad (1.19)$$

with  $\square \phi = (-g)^{-1/2} \partial_A (\sqrt{-g} g^{AB} \partial_B) \phi$  and  $\gamma$  equal to the induced metric on the boundary. Taking  $\phi(\vec{x}, z)$  to be of the form  $\phi(\vec{x}, z) = \exp(ik_\mu x^\mu) f_k(z)$ , the wave equation becomes

$$0 = \frac{1}{\ell^2} (z^2 k^2 - z^d \partial_z (z^{-d} \partial_z) + m^2 \ell^2) f_k(z). \quad (1.20)$$

The solutions to (1.20) are Bessel functions. To motivate two additional entries in the AdS/CFT dictionary, it suffices to examine only their behaviour as we approach the conformal boundary at  $z = 0$ . Near this boundary, the Bessel functions scale like a power law in  $z$ . Substituting  $f_k(z) \propto z^\Delta$  into the equation above gives

$$0 = (k^2 z^2 - \Delta(\Delta - d) + \mu^2 \ell^2) z^\Delta. \quad (1.21)$$

Or, in the limit  $z \rightarrow 0$ ,

$$\mu^2 \ell^2 = \Delta(\Delta - d) \quad \Rightarrow \quad \Delta^\pm = \frac{d}{2} \pm \sqrt{\frac{d^2}{4} + \mu^2 \ell^2}. \quad (1.22)$$

*N.B.* requiring that the energy of the scalar field be real means that the factor inside the square root of (1.22) is either positive or zero<sup>3</sup>. The mass-squared must then be  $\mu^2\ell^2 \geq -d^2/4$ , a restriction known as the Breitenlohner-Freedman bound [37].

Of the two values permitted by (1.22), only  $\Delta^+$  remains positive for any number of dimensions. Therefore, near the boundary this contribution goes like  $z^{\Delta^+}\phi_0(\vec{x})$  and remains finite as  $z \rightarrow 0$ . We will refer to solutions with this type of boundary scalar as *normalizable* solutions in subsequent chapters. Conversely, the second solution goes like  $z^{\Delta^-}\phi_0(\vec{x})$  near the boundary, and if  $\Delta^- < 0$  this contribution diverges. These are known as the *non-normalizable* solutions.

We can now use the scaling of  $\phi(\vec{x}, z)$  near the boundary to derive the scaling dimension of  $\mathcal{O}(\vec{x})$ , which tells us how relevant that operator remains with renormalization group flow. First, note that the induced metric on a cut-off surface placed at  $z = \epsilon$  in (1.19) is

$$ds^2 \Big|_{z=\epsilon} = \frac{\ell^2}{\epsilon^2} \eta_{\mu\nu} dx^\mu dx^\nu = \gamma_{\mu\nu} dx^\mu dx^\nu, \quad (1.23)$$

and that the coupling between the field and the operator given in (1.10) is more correctly written in terms of a limit of a bulk interaction. The non-vanishing part of  $\phi$  near the boundary contributes

$$\lim_{\epsilon \rightarrow 0} \int_{z=\epsilon} d^d x \sqrt{\gamma} \phi(\vec{x}, z = \epsilon) \mathcal{O}(\vec{x}, \epsilon) = \lim_{\epsilon \rightarrow 0} \int_{\partial AdS} d^d x \left( \frac{\ell}{\epsilon} \right)^d \left( \epsilon^{\Delta^-} \phi_0(\vec{x}) \right) \mathcal{O}(\vec{x}, \epsilon). \quad (1.24)$$

Since the action must be finite as  $\epsilon \rightarrow 0$ , we have that  $\mathcal{O}(\vec{x}, \epsilon) \sim \epsilon^d \epsilon^{-\Delta^-} \mathcal{O}_0(\vec{x}) = \epsilon^{d-\Delta^-} \mathcal{O}_0(\vec{x}) = \epsilon^{\Delta^+} \mathcal{O}_0(\vec{x})$ , where  $\mathcal{O}_0(\vec{x})$  is the operator in the CFT. Thus, the relevance of the operator – whether or not the operator will contribute positively, negatively, or marginally to renormalization group flow of the CFT [38] – will be determined by the value of  $\Delta^+$ .

Our primary application of the AdS/CFT correspondence will be to examine in detail various processes in the bulk given that we have a dictionary to translate the solutions to the boundary gauge theory. In particular, we wish to consider the thermalization of states of the CFT through

---

<sup>3</sup>An equivalent restriction is that  $\Delta^\pm \in \mathbb{R}$  since operators in a CFT with complex scaling dimensions violate the unitarity condition of the theory [36].

their dual description of the formation of a black hole in the bulk. In this case, the spacetime metric will initially be described by global AdS but will evolve into a Schwarzschild metric once collapse has occurred. By solving for the evolution of metric functions that interpolate between these two solutions, we are able to track the process of gravitational collapse. Note that our discussion above has been written in terms of the boundary behaviour of the scalar field in Poincaré coordinates, which were introduced in (1.8). In order to examine the behaviour of a CFT when energy is not allowed to disperse, a more suitable choice of coordinates is global coordinates, which were introduced in (1.7). As we approach the conformal boundary in the bulk – corresponding to  $x \rightarrow \pi/2$  in global coordinates – one may choose a new radial coordinate  $\theta \equiv x - \pi/2$  so that the boundary limit in global AdS is equivalent to  $\theta \rightarrow 0$ . Expanding the scalar field in this regime gives the same power law falloff as the Poincaré coordinates, but this time with respect to  $\theta$ .

Following [39], we begin by writing the metric of asymptotic  $\text{AdS}_{d+1}$  in Schwarzschild-like coordinates

$$ds^2 = \frac{\ell^2}{\cos^2(x/\ell)} \left( A e^{-2\delta} dt^2 + A^{-1} dx^2 \sin^2(x/\ell) d\Omega^{d-1} \right), \quad (1.25)$$

where  $x \in [0, \pi/2)$  and  $x = \pi/2$  corresponds to the conformal boundary. The metric functions  $A(t, x)$  and  $\delta(t, x)$  are functions of only two variables due to the spherical symmetry. We will hereafter work in units of the AdS length scale, setting  $\ell = 1$ . The Einstein and Klein-Gordon equations for the minimally-coupled scalar field  $\phi(t, x)$  are

$$G_{ab} + \Lambda g_{ab} = 8\pi \left( \nabla_a \phi \nabla_b \phi - \frac{1}{2} g_{ab} ((\nabla \phi)^2 + \mu^2 \phi^2) \right) \quad \text{and} \quad \frac{1}{\sqrt{-g}} \partial_a \sqrt{-g} g^{ab} \partial_b \phi - \mu^2 \phi = 0. \quad (1.26)$$

The canonical equations of motion are [40]

$$\partial_t \phi = A e^{-\delta} \Pi, \quad \partial_t \Phi = \partial_x (A e^{-\delta} \Pi), \quad \text{and} \quad \partial_t \Pi = \frac{\partial_x (\Phi A e^{-\delta} \tan^{d-1}(x))}{\tan^{d-1}(x)} - \frac{\mu^2 e^{-\delta} \phi}{\cos^2(x)}, \quad (1.27)$$

where the momentum is  $\Pi(t, x) = A^{-1}e^\delta \partial_t \phi$  and  $\Phi(t, x) \equiv \partial_x \phi$ . The metric functions obey

$$\begin{aligned}\partial_x \delta &= -(\Pi^2 + \Phi^2) \sin(x) \cos(x), \quad A = 1 - \frac{2M \sin^2(x)}{(d-1) \tan^{d-1}(x)} \\ \partial_x M &= \tan^{d-1}(x) \left[ \frac{A(\Pi^2 + \Phi^2)}{2} + \frac{\mu^2 \phi^2}{2 \cos^2(x)} \right],\end{aligned}\tag{1.28}$$

with the mass function  $M(t, x)$  subject to the conservation equation  $\partial_t M(t, x = \pi/2) = 0$ . The value of  $\delta(t, x)$  at either boundary is set by a gauge choice. Finally, the spherical symmetry of the system requires that  $\Phi(t, 0) = 0$ . Without imposing extra conditions at the outer boundary, there are two classes of solutions for  $\phi(t, x)$  based on their scaling as  $x \rightarrow \pi/2$ . For now, we consider only the normalizable class, i.e. solutions that scale as  $(\cos x)^{\Delta^+}$  near the conformal boundary.

Expanding the scalar field and metric functions in terms of some (small) constant  $\epsilon$ :

$$\phi(t, x) = \sum_{j=0}^{\infty} \epsilon^{2j+1} \phi_{2j+1}(t, x), \quad A(t, x) = 1 - \sum_{j=1}^{\infty} \epsilon^{2j} A_{2j}(t, x), \quad \delta(t, x) = \sum_{j=1}^{\infty} \epsilon^{2j} \delta_{2j}(t, x).\tag{1.29}$$

At linear order, the gravitational system obeys

$$\partial_t^2 \phi_1 = \left( \frac{(d-1)}{\sin(x) \cos(x)} \partial_x + \partial_x^2 - \frac{\mu^2}{\cos^2(x)} \right) \phi_1 \equiv -L\phi_1.\tag{1.30}$$

Separating the time and position dependence, we seek the normalized eigenfunctions  $e_j(x)$  that satisfy  $L e_j(x) = \omega_j^2 e_j(x)$ . These are the Jacobi polynomials:

$$e_j(x) = k_j \cos^{\Delta^\pm}(x) P_j^{(\frac{d}{2}-1, \Delta^\pm - \frac{d}{2})}(\cos(2x)).\tag{1.31}$$

The eigenvalues have the simple form  $\omega_j = 2j + \Delta^\pm$ , with  $\Delta^\pm$  given by (1.22).

Solutions to the linearized equations of motion are stable at all times [41]. However, beyond linear order there are instabilities at  $\mathcal{O}(\epsilon^3)$  due to secular terms, which are terms that grow larger with time. These terms cannot be removed by frequency shifts and arise from resonances in the spectrum of the scalar fields [42]. Various resummation [43] and multi-scale techniques [44] have been developed

to describe the growth of such terms within the perturbative description. These methods will be used in chapters 3 and 4 to absorb the resonant terms into renormalized integration constants.

The end point of the evolution of nonlinear bulk scalar fields can be generally categorized into either stable (those that resist gravitational collapse over long<sup>4</sup> time scales) or unstable (those that collapse immediately or at the perturbative timescale) configurations. In exploring these solutions, we will find a rich landscape of behaviours that lie between these more simple classifications.

### 1.3.2 Nonlinear Stability & Instability

Before focusing solely on the collapse of generic scalars in Anti-de Sitter space, it is worth noting that the stability of  $\text{AdS}_{d+1}$  has also been probed previously in several ways. *Soliton* solutions – a general class of localized field configurations – can be constructed in asymptotically- $\text{AdS}_4$  spacetime [45]. When solitons were given charges in  $\text{AdS}_5$ , their evolution exhibited phase transitions, such as the development of black hole solutions with scalar hair, that are indicative of spontaneous symmetry breaking in the boundary theory [46]. A similar type of field configuration is known as an *oscillon*. These too are localized, long-lived scalar field configurations generic to all background curvatures, but have time-dependent profiles [47]. It should be noted that these scalar field solutions were constructed by numerical methods. Indeed, finding numerical solutions to the nonlinear Einstein equations for a given field profile is a common practice; for a review on the methods used to construct such solutions, see [48].

In general, asymptotically- $\text{AdS}$  spacetime admits a variety of stable solutions [49, 50]. So-called *boson star* solutions are stationary, perturbatively stable, complex scalar field solutions [51]. Since the  $\text{AdS}_5 \times \text{S}^5$  action is invariant under the global phase transformation  $\phi \rightarrow \exp(-i\theta)\phi$ , boson stars carry a conserved charge,  $Q$ . For small values of  $Q$ , boson star solutions are related to oscillon solutions [52]. They can be constructed from both massive and massless fields in asymptotically- $\text{AdS}$  spacetimes [53]. More recently, stable boson star solutions have been described in terms of a

---

<sup>4</sup>The definition of “long” is somewhat subjective, but generally taken as many multiples of the light-crossing time. In the limit of  $\epsilon \rightarrow 0$ , however, collapse never occurs.

multi-oscillator description, wherein the scalar field is written as an infinite sum over normal modes with non-integer frequencies [54]. Interestingly, studies of the evolution of massless scalars in  $\text{AdS}_3$  found that a critical mass existed below which black holes would not form and above which static black hole solutions were supported [55]. However, the black holes formed by the collapse may or may not support scalar hair [56–59]. For a review of the stability of  $\text{AdS}_3$ , see [60].

Gravitational instability has been studied in more general contexts than the ones we will focus on here. Preliminary examinations of the onset of instability in a gravitational theory coupled to a scalar field focused on the case of a flat background geometry. For generic initial data parameterized by  $p$ , [61] observed the following critical phenomena for spherically-symmetric solutions:

- If collapse is guaranteed for values  $p > p^*$ , then as  $p \rightarrow p^*$ , black holes can be created with masses  $M \propto |p - p^*|^\gamma$ . The critical exponent  $\gamma$  is independent of initial conditions and depends only on the type matter. For a spherically symmetric, massless scalar field,  $\gamma \approx 0.37$ .
- Just before the formation of the event horizon, the spacetime approaches a scale-invariant solution – the critical solution – that is also independent of the initial conditions.

These characteristics are collectively known as Choptuik scaling, and are found in all critical gravitational collapses, independent of geometry, initial conditions, or boundary conditions [62–64]. Choptuik scaling of critical solutions for scalars in AdS is also well established [65, 66].

The most influential examination of the nonlinear stability of  $\text{AdS}_4$  was undertaken in [67], which found that it was generically unstable to any perturbation with amplitude  $\epsilon > 0$ . This was particularly surprising given that it was well known that flat spacetime required a minimum energy density for a black hole to form. It was further demonstrated that generic massless scalars in  $\text{AdS}_{d+1}$  would collapse for all  $d \geq 3$  [68, 69]. However, as we discuss below in § 1.3.4, this was not the complete picture.

Universal scaling of the horizon size (and therefore mass) was confirmed for critical data, as was scale invariance just before collapse [70]. For the critical amplitudes  $\epsilon_0 > \epsilon_1 > \epsilon_2$  such that  $r_H(\epsilon_i) = 0$ , the difference in horizon formation times between successive critical values follows  $t_H(\epsilon_{i+1}) - t(\epsilon_i) \approx \pi$ ,

the light-crossing time.

### 1.3.3 A Perturbative Description

In most cases, analytic solutions for the full evolution of critical scalars in  $\text{AdS}_{d+1}$  are not possible – the exception being  $\text{AdS}_3$  [71–74]. However, stable data are often able to be written in terms of one or more spatial eigenfunctions of  $\text{AdS}_{d+1}$ , including the examples discussed in § 1.3.2. The turbulent transfer of energy to short length scales that precedes gravitational collapse is sufficiently nonlinear that an analytical solution does not remain valid for all times. A perturbative theory, however, is able to capture the weak nonlinearity of the system over timescales of  $t \sim \epsilon^{-2}$ .

Recall the expansion described by (1.29). At first order in  $\epsilon$ , a linearized equation of motion for the leading contribution to the scalar field has solutions that are given by sums over the normal modes of  $\text{AdS}_{d+1}$  (after imposing Dirichlet conditions at the conformal boundary). The backreaction on the metric is described by the  $\mathcal{O}(\epsilon^2)$  equations for  $A_2$  and  $\delta_2$ , which are integrals involving the first-order solution  $\phi_1$ . At  $\mathcal{O}(\epsilon^3)$ , there is an inhomogeneous equation for the third order part of the scalar field

$$\partial_t^2 \phi_3 + L\phi_3 = S^{(3)}(\phi_1, A_2, \delta_2). \quad (1.32)$$

As described by [67], the source  $S^{(3)}$  contains resonant contributions that cannot be removed by frequency shifts. Resonant contributions that grow with time are known as *secular* terms, and are responsible for eventually triggering collapse by shifting the energy spectrum to high frequencies. Because such secular terms appear beyond linear order, this effect is described as weakly turbulent. Further investigation into the direct cascades of energy to higher modes confirmed that the appearance of resonant terms in  $S^{(3)}$  only when coherent phase conditions were met [75–77].

While scalar field with initial profiles that are dominated by a single linear eigenmode are nonlinearly stable, the same cannot be said for multi-mode initial data, i.e. data comprised of the addition of one or more eigenmode. In this case, the presence of the extra modes allow for resonances to occur

and secular growth to lead to collapse at times of  $t \sim \epsilon^{-2}$ . In order to better understand how these solutions maintained stability for times  $t < \epsilon^{-2}$ , [44] introduced a multi-scale technique wherein a “slow time”  $\tau = \epsilon^2 t$  governed the transfer of energy between modes. This Two-Time Formalism, or TTF, produced analytic expressions for the absorption of secular terms into the definition of renormalized amplitude and phase variables [78–80]. Families of quasi-periodic solutions that extend previous TTF configurations further expanded the space of perturbatively stable solutions [81–84]. Testing the limits of quasi-periodic solutions for massless scalar fields is the topic of the work presented in chapter 3.

### 1.3.4 The Landscape of Solutions

The presence of perturbatively stable solutions within the TTF description spurred the search for initial data that remained stable within the full, nonlinear theory. Generic initial data for a scalar field with initial width  $\sigma$  takes the form

$$\phi(t=0, x) = 0, \quad \Pi(t=0, x) = \epsilon \exp\left(-\frac{\tan^2(x)}{\sigma^2}\right). \quad (1.33)$$

Varying the width of the pulse and the mass of the field, it was found that “islands of stability” existed within the space initial data where collapse would not occur below some threshold amplitude (see figure 1.1 for one such example) [39, 85–87]. Developing a fuller picture of these islands of stability is a subject of ongoing research, and is one of the goals of the work presented in chapter 2. While the majority of existing literature uses Gaussian initial data in  $\text{AdS}_4$  and  $\text{AdS}_5$  with Dirichlet boundary conditions, more recent examinations of stability islands have included multi-oscillator constructions and Neumann boundary conditions [88, 89].

It is also worth noting as a matter of completeness that scalar field perturbations are not the only type of instabilities that have been considered. Localized, self-gravitating solutions to the Einstein-Maxwell equations in a vacuum are known as *geons*, and have long lifetimes with respect to the characteristic periods of the system [90]. The excitation of a single (scalar) geon mode is stable in

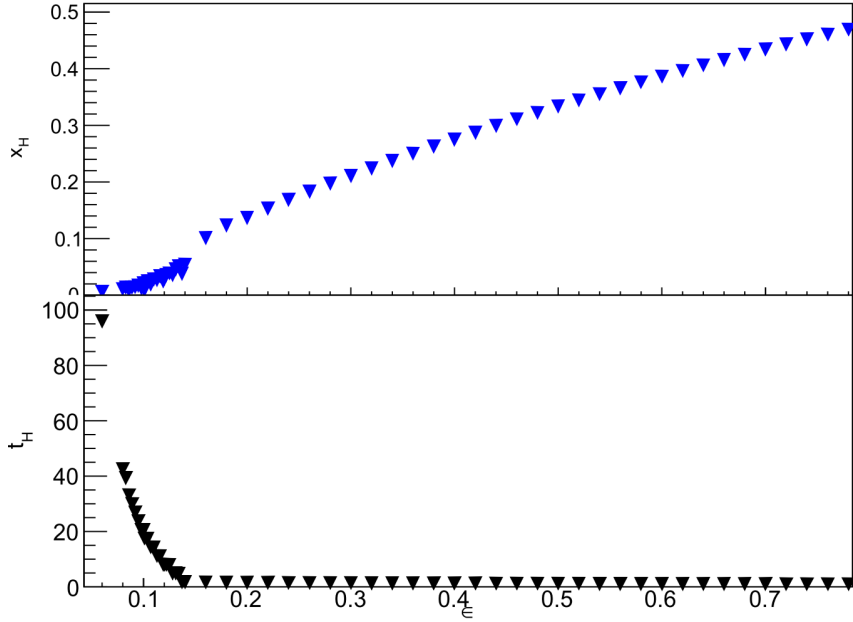


**Figure 1.1:** Horizon size  $x_H$  and horizon formation time  $t_H$  as a function of amplitude in  $AdS_5$  for a massive scalar field with  $\sigma = 2$  in (1.33). Instead of the periodic, discontinuous behaviour, there is some minimal value  $\epsilon_{min}$  below which black holes do not form. Used with permission from [39].

Anti-de Sitter space; however, any combination of two or more such modes becomes unstable [91]. This complements the conjecture that the stability islands in the space of scalar field data may be anchored by linear modes. In asymptotically- $AdS_4$  spacetimes, stable geon solutions can be constructed numerically [92, 93].  $AdS$  is unstable against all vector geon modes [94].

### 1.3.5 Driven Scalars

We have previously limited our discussion to the normalizable scalar field solutions, as these are responsible for the weakly turbulent instabilities that lead to gravitational collapse. In general, the linearized equations of motion (1.30) admit two types of solutions with two different scaling behaviours near the boundary. The second set of solutions, which scale as  $z^{\Delta^-}$  as  $z \rightarrow 0$ , are known as non-normalizable solutions and are not restricted to integer frequencies. These solutions can couple to time-dependent terms on the boundary, thereby carrying energy into the bulk, and are known as driven, or *pumped*, scalar fields.

The emergence of new phases in a Conformal Field Theory as a function of driving frequency is

known as Floquet dynamics [95, 96]. The holographic dual to such a system is described by the driving of a massless, complex, bulk scalar field by a time-dependent boundary term. The vacuum bulk solution corresponds to a Floquet condensate on the boundary. Such solutions exhibit both stable and unstable evolution over the space of initial data, with the unstable data branching into two possible endpoints: the formation of a black hole in the bulk theory, or a horizonless, pulsating, late-time solution [97, 98]. For real scalar fields subject to monotonically increasing boundary conditions, both stable and unstable data exist; however, unstable data can result in either a black hole solution, or a limiting cycle. When periodic boundary conditions are considered, dynamically stabilized big crunch singularities are possible for sufficiently high driving frequencies [99].

Despite constructing stable and unstable numerical solutions for driven scalars, analytic solutions to the perturbative description of weakly turbulent instabilities has yet to extend beyond leading order in the backreacton with the metric [100]. Capturing  $\mathcal{O}(\epsilon^3)$  instabilities in these driven scalar systems is the focus of the work in chapter 4.

## 1.4 Summary

We have now seen how the AdS/CFT correspondence establishes a duality between strongly-coupled gauge theories and weakly-coupled gravitational theories in one extra dimension. Using this correspondence, various dynamical processes in strongly-coupled gauge theories can be explored via the collapse of scalar fields in Anti-de Sitter spacetime. Furthermore, we have seen that the end state of the theory depends on the initial profile of the scalar field, and that a large variety of both stable and unstable phenomena are possible. However, a better understanding of the islands of stability in the full theory, as well as the limits of the perturbative description, is still required. Similarly, the incorporation of time dependent boundary conditions into a perturbative theory for the weakly turbulent instabilities remains an outstanding issue. The work collected in this thesis aims to address these issues.

The following chapters each contain a manuscript that is focused on research into one of the areas

described above. After a brief discussion of how each project contributes to the resolution of these issues, the contributions of the authors are laid out. The work itself is then presented. A discussion of how these works contribute to a better understanding of gravitational collapse in Anti-de Sitter space follows in chapter 5.

## 2 Nonlinear Evolution of Massive Scalar Fields in Anti-de Sitter Spacetime

As mentioned in § 1.3.2, within the space of initial data for massive scalar fields in  $\text{AdS}_{d+1}$  there are islands of stability for Gaussian momentum profiles where collapse does not occur for sufficiently small perturbations. Examining the dependence of the end state (stable, unstable, or otherwise) on the initial conditions has been the goal of previous works, such as [39, 101] and others. However, the limit of small but non-perturbative amplitudes requires significant computing resources and has only recently become computationally accessible. The goal of the work presented here is to leverage the computing resources available through Westgrid and Compute Canada to examine the broadest possible range of initial parameters.

### 2.1 Contributions of Authors

The research covered in this work built upon on the numerical solving methods first utilized as part of [39, 101] to examine nonlinear instabilities in the full Einstein/Klein-Gordon system of massive scalars in  $\text{AdS}_{d+1}$ . The goal of this work was to expand the space of initial data being considered and thereby chart the islands of stability. Previous work had identified these islands and commented on the transition regions between stable and unstable configurations, but had avoided the computationally costly simulations required for cases on the “shoreline.”

My role involved running multiple, simultaneous simulations over different heterogeneous computing clusters through the Westgrid network of the Compute Canada consortium. I was responsible for

roughly 184 core years<sup>5</sup> worth of simulations over the course of this work.

To perform the data analysis required, I wrote new plotting programs that interfaced with existing data types while also providing extensions specifically for this project. For example, code for plotting the horizon formation time  $t_H$  against the amplitude of the perturbation  $\epsilon$  was rewritten in python with a range of fitting options for critical data above a specified  $t_{fit}$  (see plots and insets in figure 2.4 along with fitting parameters in table 2.1). I also programmed and performed all of the convergence tests included in appendix 2.A that verified the evolution of the data. Of particular importance was discerning the reliability of the solutions for irregular data. In figures 2.A.4 and 2.A.5, the order of convergence  $Q$  is calculated for irregular data. These tests help to validate important observations of chaotic evolution, even for massless scalars.

As is common for these types of projects, all members of the collaboration were equally involved in the interpretation of the data, as well as the late stages of editing. Authors are listed alphabetically and it is understood that all members contribute equally to the publication.

---

<sup>5</sup>From the [Compute Canada](#) website: “a core year is the equivalent of running computations on a CPU core constantly for a period of one year.”

# Phase Diagram of Stability for Massive Scalars in Anti-de Sitter Spacetime

Phys. Rev. **D102** (2020) 2, 026015 [[1711.00454](#)]

Brad Cownden<sup>1</sup>, Nils Deppe<sup>2</sup>, and Andrew R. Frey<sup>1,3</sup>

<sup>1</sup>*Department of Physics & Astronomy,*

*University of Manitoba*

*66 Chancellors Cir, Winnipeg, Manitoba R3T 2N2, Canada*

<sup>2</sup>*Cornell Center for Astrophysics and Planetary Science and Department of Physics,*

*Cornell University*

*122 Sciences Drive, Ithaca, New York 14853, USA*

<sup>3</sup>*Department of Physics and Winnipeg Institute for Theoretical Physics,*

*University of Winnipeg*

*515 Portage Avenue, Winnipeg, Manitoba R3B 2E9, Canada*

We diagram the behavior of 5-dimensional anti-de Sitter spacetime against horizon formation in the gravitational collapse of a scalar field, treating the scalar field mass and width of initial data as free parameters, which we call the stability phase diagram. We find that the class of stable initial data becomes larger and shifts to smaller widths as the field mass increases. In addition to classifying initial data as stable or unstable, we identify two other classes based on nonperturbative behavior. The class of metastable initial data forms a horizon over longer time scales than suggested by the lowest order perturbation theory at computationally accessible amplitudes, and irregular initial data can exhibit non-monotonic and possibly chaotic behavior in the horizon formation times. Our results include evidence for chaotic behavior even in the collapse of a massless scalar field.

## 2.2 Introduction

Through the anti-de Sitter spacetime (AdS)/conformal field theory (CFT) correspondence, string theory on  $\text{AdS}_5 \times X^5$  is dual to a large  $N$  conformal field theory in four spacetime dimensions ( $\mathbb{R} \times S^3$  when considering global  $\text{AdS}_5$ ). The simplest time-dependent system to study in this context is the gravitational dynamics of a real scalar field with spherical symmetry, corresponding to the time dependence of the expectation value of the zero mode of a single trace operator in the gauge theory. Starting with the pioneering work of [67–70], numerical studies have suggested that these dynamics may in fact be generically unstable toward formation of (asymptotically)  $\text{AdS}_{d+1}$  black holes even for arbitrarily small amplitudes. While perhaps surprising compared to intuition from gravitational collapse in asymptotically flat spacetimes, the dual picture of thermalization of small energies in a compact space is more expected. In terms of the scalar eigenmodes on a fixed AdS background, the instability is a cascade of energy to higher frequency modes and shorter length scales (weak turbulence), which eventually concentrates energy within its Schwarzschild radius. In a naive perturbation theory, this is evident through secular growth terms.

However, some initial scalar field profiles lead to quasi-periodic evolution (at least on the time scales accessible via numerical studies) at small but finite amplitudes; even early work [67, 91] noted that it is possible to remove the secular growth terms in the evolution of a single perturbative eigenmode. A more sophisticated perturbation theory [42, 44, 78–80, 82, 102–107] supports a broader class of quasi-periodic solutions that can contain non-negligible contributions from many modes, and other stable solutions orbit the basic quasi-periodic solutions [82]. Stable solutions exhibit inverse cascades of energy from higher frequency to lower frequency modes due to conservation laws following from the high symmetry of AdS (integrability of the dual CFT). Stable behavior also appears in the full non-perturbative dynamics for initial profiles with widths near the AdS length scale [52, 108, 109]; however, analyses of the perturbative and full dynamics in the literature have not always been in agreement at fixed small amplitudes. For example, some perturbatively stable evolutions at finite amplitude actually form black holes in numerical evaluation of the full

dynamics [41, 44, 81]. Understanding the breakdown of the approximations used in the perturbative theory, as well as its region of validity, is an active and important area of research [83, 110–113].

Ultimately, the main goal of this line of inquiry is to determine whether stability or instability to black hole formation (or both) is generic on the space of initial data, so the extent of the “islands of stability” around single-mode or other quasi-periodic solutions and how it varies with parameters of the physics on AdS are key questions of interest. The biggest changes occur in theories with a mass gap in the black hole spectrum, such as  $\text{AdS}_3$  and Einstein-Gauss-Bonnet gravity in  $\text{AdS}_5$ , which cannot form horizons at small amplitudes. While small-amplitude evolution in  $\text{AdS}_3$  appears to be quasi-periodic [31, 60], there is some evidence to point toward late-time formation of a naked singularity in  $\text{AdS}_5$  Einstein-Gauss-Bonnet gravity [101, 114] (along with a power law energy spectrum similar to that at horizon formation). Charged scalar and gauge field matter [115] also introduces a qualitative change in that initial data may lead to stable evolution or instability toward either Reissner-Nordström black holes or black holes with scalar hair.

In this paper, we extend the study of massive scalar matter initiated in [39, 85]. Specifically, using numerical evolution of the full gravitational dynamics, we diagram classes of gravitational collapse behavior as a function of scalar field mass and initial scalar profile width, which we call a stability phase diagram in analogy to a phase diagram for phases of matter. This is the first systematic study of behavior for classes of initial data in AdS gravitational collapse using two tuning parameters. By considering the time to horizon formation as a function of the initial profile’s amplitude at finite amplitude, we identify several different classes of behavior and indicate them on the phase diagram. Finally, we analyze and characterize these different behaviors, presenting evidence for chaotic behavior, including the first evidence for chaotic behavior in the horizon formation time of massless scalar collapse, which has no length scale other than the AdS radius. Throughout, we work in  $\text{AdS}_5$ , due to its relevance to strongly coupled gauge theories in four dimensions and because previous literature has indicated massless scalars lead to greater instability than in  $\text{AdS}_4$  (the main other case considered), which makes the effects of the scalar field mass more visible.

We note briefly two caveats for the reader. First, horizon formation always takes an infinite amount

of time on the AdS conformal boundary due to the usual time dilation effects associated with horizons; this agrees with the understanding of thermalization in the CFT as an asymptotic process. Horizon formation times discussed in this paper correspond to an approximate notion of horizon formation that we will describe below, but alternate measures of thermalization may be of interest. Second, the black holes we discuss are smeared on the compact  $X^5$  dimensions of the gravitational side of the duality, as in most of the literature concerning stability of AdS, and we are particularly interested in small initial amplitudes that lead to black holes small compared to the AdS scale. As described in [116–118], small black holes in this situation suffer a Gregory-Laflamme-like instability toward localization on  $X^5$  (which may in fact lead to formation of a naked singularity). At the same time, certain light stable solutions for charged scalars (boson stars) are stable against localization on  $X^5$  [119]. We therefore provisionally assume that the onset of the Gregory-Laflamme-like instability occurs only at horizon formation, not at any point of the earlier horizon-free evolution.

The plan of this paper is as follows: in section 2.3, we review the time scales associated with horizon formation with an emphasis on the behavior of massive scalars and briefly discuss our methods. Then, in section 2.4, we present the phase diagram of different stability behaviors, and an attempt at heuristic analytic understanding appears in 2.5. We close with a discussion of our results.

## 2.3 Review

In this section, we review results on the stability of scalar field initial data as well as our methods (following the discussion of [39]).

### 2.3.1 Massive scalars, stability, and time scales

As in most of the literature, we work in Schwarzschild-like coordinates, which have the line element (in asymptotic  $\text{AdS}_{d+1}$ )

$$ds^2 = \frac{1}{\cos^2(x)} (-Ae^{-2\delta}dt^2 + A^{-1}dx^2 + \sin^2(x)d\Omega^{d-1}) \quad (2.1)$$

in units of the AdS scale. In these coordinates, a horizon appears at  $A(x, t) = 0$ , but reaching zero takes an infinite amount of time (measured either in proper time at the origin or in conformal boundary time); following the standard approach, we define a horizon as having formed at the earliest spacetime point (as measured by  $t$ ) where  $A$  drops below a specified threshold defined in §2.3.2 below. Of course, horizon formation represents a coarse-grained description since the pure initial state of the dual CFT cannot actually thermalize; a more precise indicator of approximate thermalization may be the appearance of a power law energy spectrum (exponentially cut off) in the perturbative scalar eigenmodes. This indicator is tightly associated with horizon formation (though see [101, 114] for some counterexamples).

A key feature of any perturbative formulation of the gravitational collapse is that deviations from  $A = 1, \delta = 0$  appear at order  $\epsilon^2$ , where  $\epsilon$  is the amplitude of initial data. As a result, horizons can form only after a time  $t \sim \epsilon^{-2}$ ; in the multiscale perturbation theory of [42, 44, 78–80, 82, 103, 105–107], there is in fact a scaling symmetry  $\epsilon \rightarrow \epsilon', t \rightarrow t(\epsilon/\epsilon')^2$  that enforces the proportionality  $t_H \propto \epsilon^{-2}$ , where  $t_H$  is the (approximate) horizon formation time for unstable initial data at small amplitude.

At this point, it is worth making a small clarification. If the collapsing matter takes the form of a well-defined pulse, horizon formation occurs when the pulse nears the origin. For massless matter, that means that the  $t_H$  is piecewise continuous as a function of  $\epsilon$ ; each continuous “step” has approximately constant  $t_H$  and is separated from the next step by a time of approximately  $\pi$ , the light crossing time for a round trip from the origin to the boundary of AdS. Massive matter does not reach the boundary, so the steps are not always separated by  $\pi$ , and may in fact not be separated

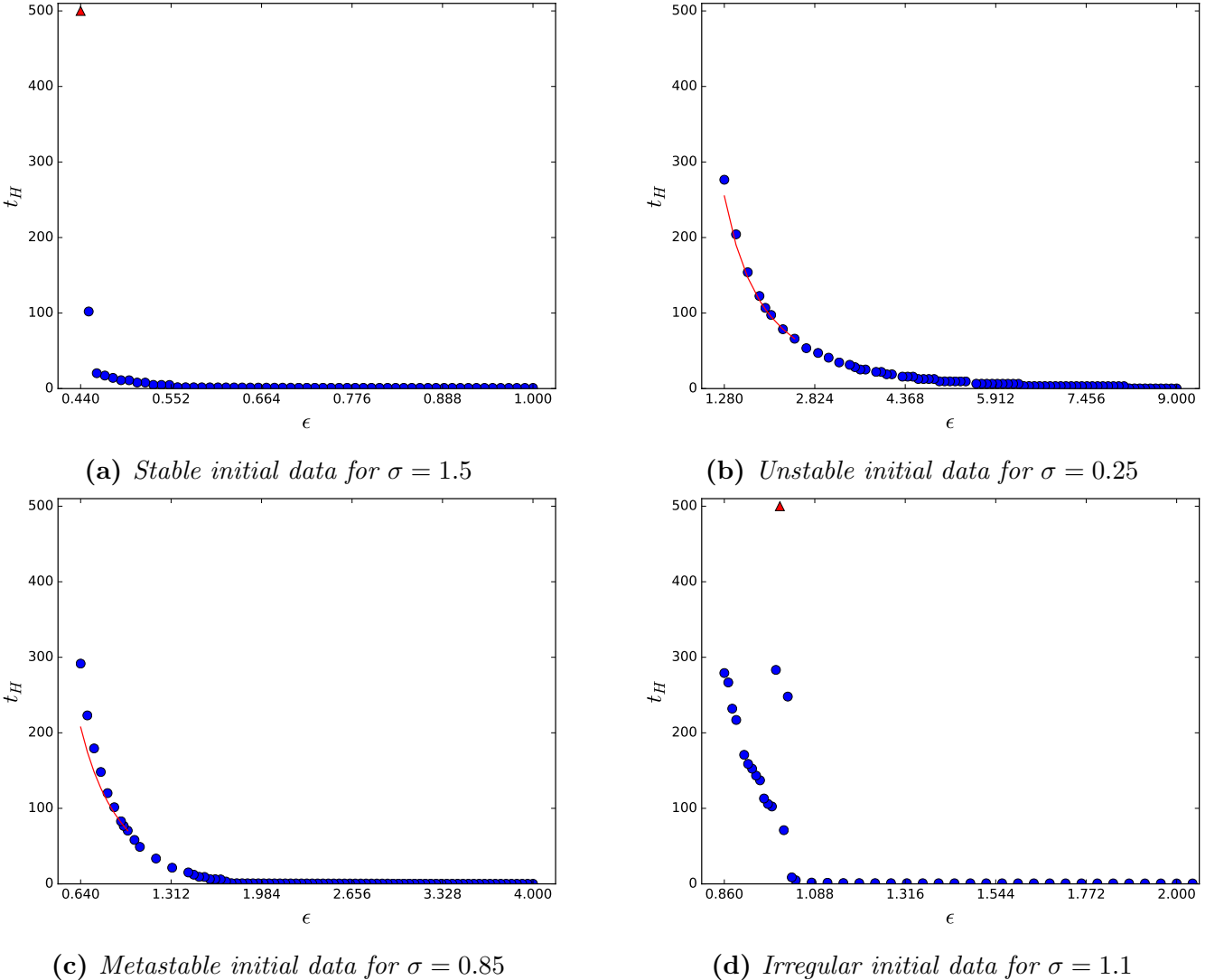


**Figure 2.1:** Classes of initial data for massless scalars and initial width  $\sigma$ . Blue dots represent horizon formation; red triangles indicate a lower limit for  $t_H$ . Red curves in subfigures 2.1b, 2.1c are  $t_H = a\epsilon^{-2} + b$  matched to largest two amplitudes in the curve.

at all if the pulse spreads out in radius. In any case, though, the width of the steps decreases drastically as amplitude decreases, so it becomes very difficult to find the transition amplitudes numerically. In fact, adjacent amplitudes in a numerical sample are typically multiple steps apart once the evolution is already long, which justifies using the perturbative scaling  $t_H \propto \epsilon^{-2}$ .

Based on the perturbative scaling relation, initial data can be divided into several classes with respect to behavior at low amplitudes, as illustrated in figure 2.1 for massless scalars. *Stable* initial data evolves indefinitely without forming a horizon. In practice, we identify this type of behavior in

numerical evolutions by noting rapid horizon formation at high amplitude with a vertical asymptote in  $t_H$  just above some critical amplitude. In our numerical results, we see a sudden jump at the critical amplitude to evolutions with no horizon formation to a large time  $t_{lim}$ , possibly with a small window of amplitudes with large  $t_H$  just above the critical amplitude. In a few cases, we have captured a greater portion of the asymptotic region. See figure 2.1a. *Unstable* initial data, in contrast, forms a horizon at all amplitudes following the perturbative scaling relation  $t_H \propto \epsilon^{-2}$  as  $\epsilon \rightarrow 0$ . In our analysis, we will verify this scaling by fitting  $t_H$  to a power law as described in section 2.3.2 below; if we limit the fit to smaller values of  $\epsilon$ , the scaling becomes more accurate. Figure 2.1b shows unstable data. The red curve is of the form  $t_H = a\epsilon^{-2} + b$  with  $a, b$  determined by matching the curve to the data for the largest two amplitudes with  $t_H \geq 60$  (not a best fit); note that the data roughly follows this curve. The categorization of different initial data profiles with similar characteristic widths into stable and unstable is robust for massless and massive scalars [39]; small and large width initial data are unstable, while intermediate widths are stable. One of the major results of this paper is determining how the widths of initial data in these “islands of stability” vary with scalar mass.

A priori, there are other possible types of behavior, at least beyond the first subleading order in perturbation theory, that is, at finite  $\epsilon$ . *Metastable* initial data collapses with  $t_H \propto \epsilon^{-p}$  with  $p > 2$  at small but not arbitrarily small amplitudes (or another more rapid growth of  $t_H$  with decreasing amplitude). We will find this type of behavior common on the “shoreline” of islands of stability where stable behavior transitions to unstable. As we will discuss further below, metastable behavior may or may not continue as  $\epsilon \rightarrow 0$ ; in principle, as higher order terms in perturbation theory become less important, the behavior may shift to either stable or unstable as described above. In principle, initial data that is stable at third order in perturbation theory but unstable at higher order could have metastable scaling even in the  $\epsilon \rightarrow 0$  limit, though our numerical study cannot address this case. We in fact find circumstantial evidence in favor of the different possibilities. In the case that the  $\epsilon \rightarrow 0$  behavior is perturbatively unstable, the perturbative scaling  $t_H \propto \epsilon^{-2}$  only appears for larger  $t_H$  than the typical unstable case; it may therefore be reasonable for the reader

to consider metastable initial data as part of a second order transition between unstable and stable classes of initial data. Figure 2.1c shows metastable initial data that continues to collapse to times  $t_H \sim 0.6t_{lim}$  but more slowly than  $\epsilon^{-2}$ ; note that  $t_H$  for collapsed evolutions at small amplitudes lies significantly above the curve  $t_H = a\epsilon^{-2} + b$  (which is determined as in figure 2.1b). There was one additional type of behavior identified by [39], which was called “quasi-stable” initial data at the time since the low-amplitude behavior was not yet clear. We find here that these initial data are typically stable at small amplitude but exhibit irregular behavior in  $t_H$  as a function of  $\epsilon$ , so we will denote them as *irregular* initial data; irregular behavior may be strongly non-monotonic or even exhibit some evidence of chaos. Figure 2.1d shows an example of irregular initial data. Later, we will see more striking examples of this behavior for massive scalars.

We emphasize that we are not claiming that metastable or irregular behavior persist to arbitrarily small amplitudes (though a priori metastable behavior could). In that sense, the multiscale perturbation theory suggests that the only two classes of stability behavior are stable and unstable with  $t_H \propto \epsilon^{-2}$  scaling as  $\epsilon \rightarrow 0$ . However, it is also important to understand physics outside the perturbative regime, and classifying the behavior of AdS when higher-order or nonperturbative effects contribute is still of interest. For example, it is clear that metastable initial data (as defined precisely below) does not exhibit perturbatively unstable behavior for  $t_H$  values as small as other unstable initial data, even in the cases where it may at all. This may help understanding the breakdown of the multiscale perturbation theory. Similarly, irregular initial data leads to qualitatively different behavior even visually and suggests that nonperturbative dynamics are important. It is in the spirit of looking beyond the multiscale perturbation theory that we call metastable and irregular initial data independent classes of behavior, even if they are not quite on the same standing as perturbatively stable or unstable classes. This paper presents the first systematic mapping of where these distinct behaviors appear.

### 2.3.2 Methods

For spherically symmetric motion, the Klein-Gordon equation for scalar mass  $\mu$  can be written in first order form as

$$\phi_{,t} = A e^{-\delta} \Pi, \quad \Phi_{,t} = (A e^{-\delta} \Pi)_{,x}, \quad (2.2)$$

$$\Pi_{,t} = \frac{(A e^{-\delta} \tan^{d-1}(x) \Phi)_{,x}}{\tan^{d-1}(x)} - \frac{e^{-\delta} \mu^2 \phi}{\cos^2(x)}, \quad (2.3)$$

where  $\Pi$  is the canonical momentum and  $\Phi = \phi_{,x}$  is an auxiliary variable. The Einstein equation reduces to constraints, which can be written as

$$\delta_{,x} = -\sin(x) \cos(x) (\Pi^2 + \Phi^2) \quad (2.4)$$

$$M_{,x} = (\tan(x))^{d-1} \left[ A \frac{(\Pi^2 + \Phi^2)}{2} + \frac{\mu^2 \phi^2}{2 \cos^2(x)} \right], \quad (2.5)$$

$$A = 1 - 2 \frac{\sin^2(x)}{(d-1)} \frac{M}{\tan^d(x)}, \quad (2.6)$$

where the mass function  $M$  asymptotes to the conserved ADM mass at the boundary  $x = \pi/2$ . We will restrict to  $d = 4$  spatial dimensions. Since results are robust against changes in the type of initial data [39], we can take the initial data to be a Gaussian of the areal radius in the canonical momentum and trivial in the field. Specifically,

$$\Pi(t=0, x) = \epsilon \exp \left( -\frac{\tan^2(x)}{\sigma^2} \right), \quad \phi(t=0, x) = 0. \quad (2.7)$$

The width  $\sigma$  and field mass  $\mu$  constitute the parameter space for our stability phase diagram.

We solve the Klein-Gordon evolution equations (2.2,2.3) and Einstein constraint equations (2.4,2.5) numerically using methods similar to those of [109] on a spatial grid of  $2^n + 1$  grid points; we discuss the convergence properties of our code in the appendix. We denote the approximate horizon position  $x_H$  and formation time  $t_H$  by the first point such that  $A(x_H, t_H) \leq 2^{7-n}$ . In detail, we evolve the system in time using a 4th-order Runge-Kutta stepper and initially use a 4th-order Runge-Kutta

spatial integrator at resolution  $n = 14$ . If necessary, we switch to a 5th-order Dormand-Prince spatial integrator and increase resolution near horizon formation. Due to time constraints, we do not increase the resolution beyond  $n = 21$  for any particular calculation; if a higher resolution would be required to track horizon formation for a given amplitude, we exclude that amplitude.

To determine the stability class of initial data with a given width  $\sigma$ , we allow evolutions to run to a maximum time of  $t_{lim} = 500$  in AdS units, so  $t_{lim}$  is a lower limit for  $t_H$  for amplitudes that do not form a horizon within that time. Normally, however, if the initial data appears unstable, we only evolve amplitudes with  $t_H \lesssim 0.6t_{lim}$ ; this is partly to save computational resources and partly to distinguish stable evolutions from collapsing ones. For unstable or metastable initial data, we find the best fit of the form  $t_H = a\epsilon^{-p} + b$  to evolutions with  $t_H > t_{fit}$ , where  $t_{fit}$  is a constant time chosen such that amplitudes with evolutions that last longer are usually roughly perturbative;<sup>6</sup> in practice,  $t_{fit} = 60$  gives results close to the perturbative result  $p = 2$  for evolutions expected to be unstable from the literature, but we will also consider  $t_{fit} = 80, 100$  as described below. In other words, since a given amplitude  $\epsilon$  may be in the perturbative scaling regime for one set of initial data but nonperturbative for another, we compare initial data at similar horizon formation times (addressing the onset of perturbative behavior). Choosing  $t_{fit}$  as above gives consistent values of the fit parameters for the three values of  $t_{fit}$  for the largest and smallest initial data widths, which are unstable.

## 2.4 Phase Diagram of Stability

Here we give our main result, the phase diagram of stability classes as a function of initial profile width and scalar mass, along with a more detailed discussion of the scaling of horizon formation time with amplitude for varying initial data.

The stability phase diagram for spherically symmetric scalar field collapse in  $\text{AdS}_5$ , treating the

---

<sup>6</sup>The power law plus constant fits the leading and first subleading contribution to  $t_H$  in a perturbative expansion in  $\epsilon$ , and we have found that the subleading term is typically not negligible in the computationally accessible regime.

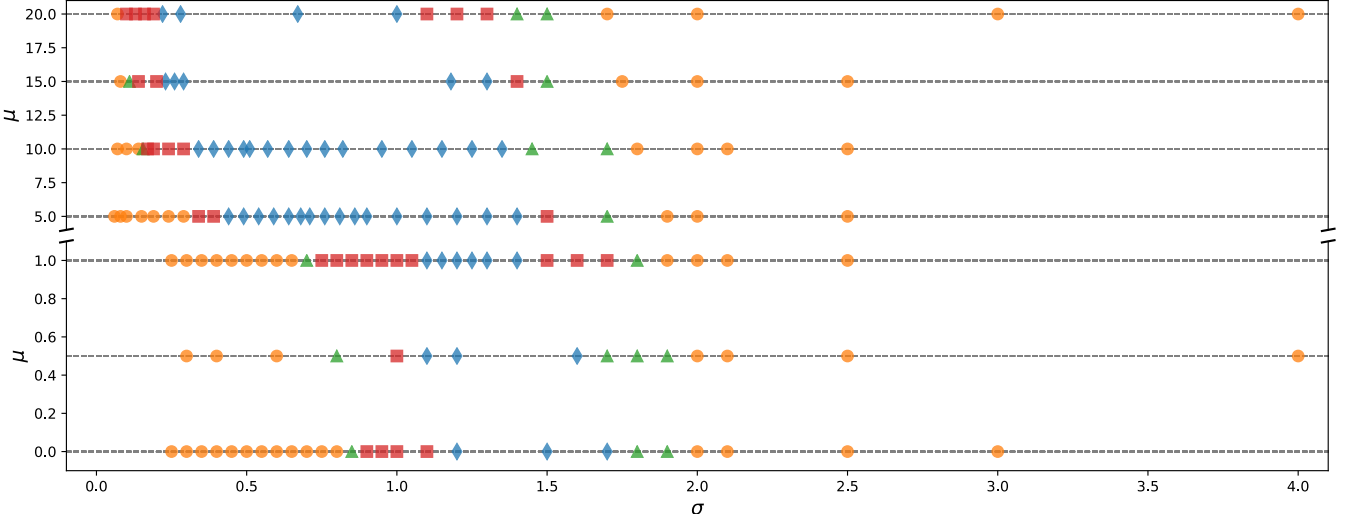


**Figure 2.2:** Stability phase diagram as a function of initial data width  $\sigma$  and scalar field mass  $\mu$ . Blue diamonds represent stable initial data, orange circles unstable initial data, green triangles metastability, and red squares irregular behavior.

width  $\sigma$  of initial data and scalar field mass  $\mu$  as tunable parameters, appears in figure 2.2. Each  $(\mu, \sigma)$  combination that we evolved numerically is indicated by a point, with blue diamonds and orange circles representing stable and unstable initial data respectively. The metastable class is represented by green triangles, while the irregular class are represented by red squares. Note that the graph has been divided into two regions with different scales, separated by a break:  $0 \leq \mu \leq 1$  is pictured on the bottom, while  $5 \leq \mu \leq 20$  is pictured on the top. At a glance, two features of the stability phase diagram are apparent: as  $\mu$  increases, the island of stability moves toward smaller values of  $\sigma$  and takes up a gradually larger range of  $\sigma$ . To be specific, the stable class of initial data is centered at  $\sigma = \bar{\sigma} \sim 1.4$  and has a width of  $\Delta\sigma \sim 0.7$  for  $\mu = 0, 0.5$ , with  $\bar{\sigma} \sim 1.2$  for  $\mu = 1$ .  $\Delta\sigma$  increases to  $\sim 1.1$ , and the island of stability is centered at  $\bar{\sigma} \sim 0.9$  for  $\mu = 5, 10$ , while  $\Delta\sigma \sim 1.2$  for  $\mu = 15, 20$  with the stable class centered at  $\bar{\sigma} \sim 0.8$ . Note that the transition between ‘‘light field’’ and ‘‘heavy field’’ behavior occurs for  $\mu > 1$  in AdS units.

The metastable and irregular classes appear at the shorelines of the island of stability, the boundary between unstable and stable classes. In particular, the slope of the power law  $t_H \sim \epsilon^{-p}$  as  $\epsilon \rightarrow 0$  increases as the width moves toward the island of stability, leading to metastable behavior. We find metastability at the large  $\sigma$  shoreline for all  $\mu$  values considered and also at the small  $\sigma$  shoreline

for several scalar masses. It seems likely that metastable behavior appears in only a narrow range of  $\sigma$  for larger  $\mu$ , which makes it harder to detect in a numerical search, leading to its absence in some parts of the stability phase diagram. We find irregular behavior at the small  $\sigma$  shoreline for every mass and at the large  $\sigma$  boundary for large  $\mu$ , closer to stable values of  $\sigma$  than metastable initial data. This class of initial data includes a variety of irregular and non-monotonic behavior, as detailed below. Evidence for chaotic behavior especially becomes more prominent at larger values of  $\mu$ , as we will discuss below.

### 2.4.1 Metastable versus unstable initial data

While stable and irregular initial data are typically apparent by eye in a plot of  $t_H$  vs  $\epsilon$ , distinguishing the unstable from metastable classes is a quantitative task. As we described in section 2.3.2, we find the least squares fit of  $t_H = a\epsilon^{-p} + b$  to all evolutions with  $t_H > t_{fit}$  for the given  $(\mu, \sigma)$ , running over values  $t_{fit} = 60, 80, 100$ . Using the covariance matrix of the fit, we also find the standard error for each fit parameter. We classify a width as having unstable evolution if the best fit value of  $p$  is within two standard errors of  $p = 2$  for  $t_{fit} = 60, 80$  or one standard error for  $t_{fit} = 100$  (due to a smaller number of data points, the standard errors for  $t_{fit} = 100$  tend to be considerably larger). In contrast, we classify a width as having metastable evolution if the best fit  $p$  is statistically significantly different from 2 (in that the best fit value is more than 2 standard errors from  $p = 2$  for  $t_{fit} = 60, 80$  and more than 1 standard error from  $p = 2$  for  $t_{fit} = 100$ ). This indicates that either further subleading contributions in a perturbative expansion of  $t_H$  are non-negligible in this regime for metastable initial data or that possibly metastable initial data are stable at the first nontrivial order in perturbation theory. Considering larger values of  $t_{fit}$  helps to ensure that the leading perturbative terms do not come to dominate for particular initial profile at the smallest computationally accessible amplitude values. In the case that the fit to  $t_H = a\epsilon^{-p} + b$  has large reduced  $\chi^2$  or is sensitive to fitting algorithm, the data is not well-described by our fitting function, so we classify it as irregular (see the next subsection).

The fits  $t_H = a\epsilon^{-p} + b$  allow us to explore the time scale of horizon formation across the stability

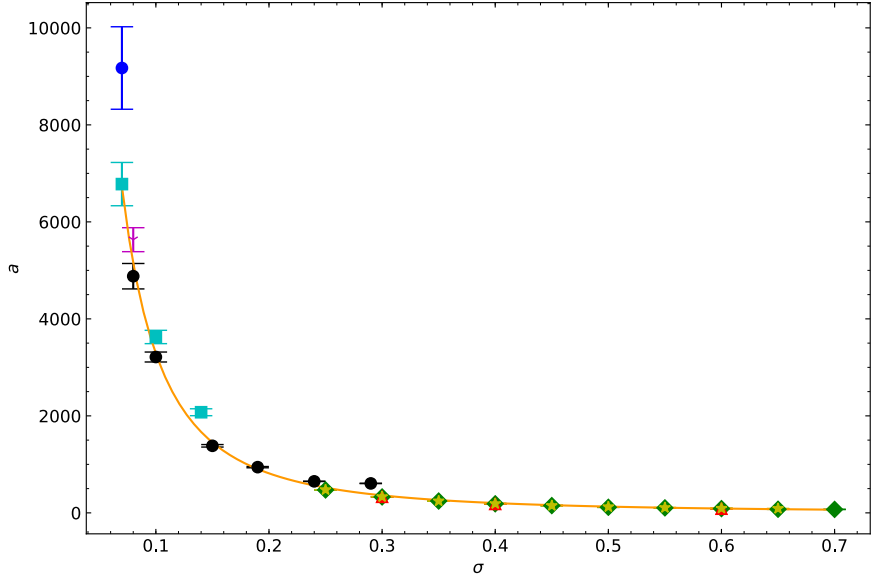
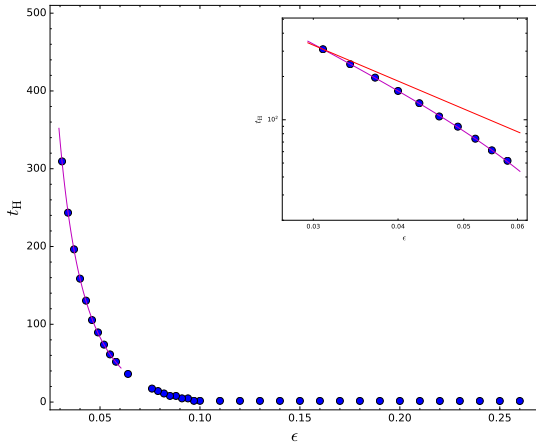


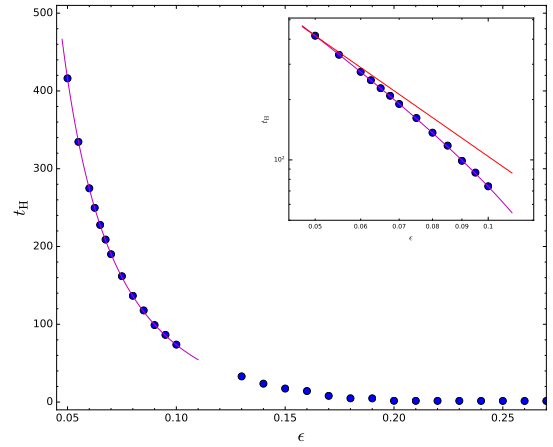
**Figure 2.3:** Coefficient  $a$  from the fit  $t_H = a\epsilon^{-p} + b$  as a function of width  $\sigma$  using  $t_{fit} = 60$ . Shows data for  $\mu = 0$  (green diamonds), 0.5 (red triangles), 1 (yellow stars), 5 (black circles), 10 (cyan squares), 15 (magenta Y), and 20 (blue circles). The orange line is the best power law fit.

phase diagram, for example through a contour plot of one of the coefficients vs  $\sigma$  and  $\mu$ . In most cases, this has not been informative, but an intriguing feature emerges if we plot the normalization coefficient  $a$  vs  $\sigma$  for unstable initial data at small  $\sigma$ , as shown in figure 2.3 for  $t_{fit} = 60$ . By eye, the coefficient is reasonably well described by the fit  $a = (32.0 \pm 0.3)\sigma^{-(2.01 \pm 0.02)}$  (values following  $\pm$  are standard errors of the best fit values) *independent of scalar field mass*. This is not born out very well quantitatively; the reduced  $\chi^2$  for the fit is  $\chi^2/\text{d.o.f.} = 180$ , indicating a poor fit. However, the large  $\chi^2$  seems largely driven by a few outlier points with large scalar mass, so it is tempting to speculate that the gravitational collapse in this region of parameter space is driven by gradient energy, making all fields effectively massless at narrow enough initial  $\sigma$ . The picture is qualitatively similar if we consider the parameter  $a$  for  $t_{fit} = 80, 100$  instead.

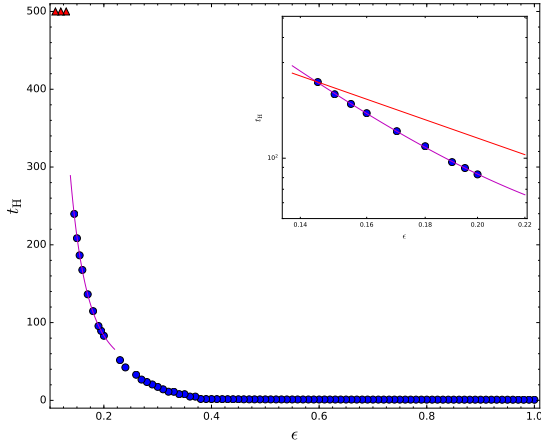
Several examples of metastable behavior appear in figure 2.4. These figures show both data from the numerical evolutions (blue dots and red triangles) and fits of the form  $t_H = a\epsilon^{-p} + b$  for points with  $t_H > t_{fit} = 60$  (magenta curves). The best fit parameters are given in table 2.1 along with the standard errors (listed following  $\pm$  for the fit values) and  $\chi^2$  values. The insets show the fit region with a log-log scale and an additional line (red) showing an  $\epsilon^{-2}$  power law normalized to fit



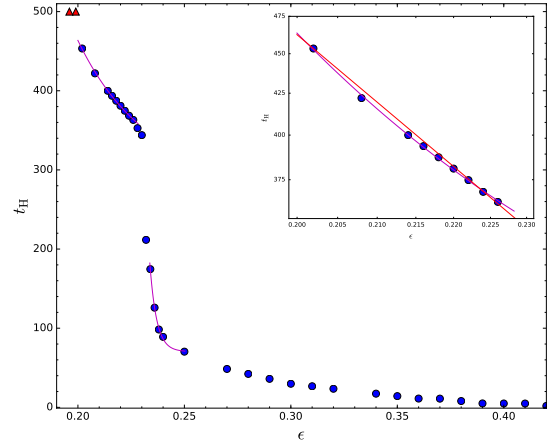
(a)  $\mu = 15, \sigma = 1.5$



(b)  $\mu = 5, \sigma = 1.7$



(c)  $\mu = 0, \sigma = 1.8$



(d)  $\mu = 0.5, \sigma = 1.7$

**Figure 2.4:** Metastable behavior: blue dots represent horizon formation and red triangles a lower limit on  $t_H$ . Magenta curves are fits  $t_H = a\epsilon^{-p} + b$  over the shown range of amplitudes. Insets show the fit region with log-log scale; note that the fit is not strictly a power law, so the fits are not straight lines. See table 2.1 for best fit parameters. Red lines in insets are  $\epsilon^{-2}$  power laws normalized to the  $t_H$  of the smallest amplitude shown.

the smallest amplitude shown in the inset. It is visually clear that  $t_H$  grows faster than  $\epsilon^{-2}$  for all these examples as  $\epsilon$  decreases in the fit region (there is a significant constant offset in figure 2.4d).

Figures 2.4a,2.4b demonstrate behavior typical of most of the instances of metastable initial data we have found; specifically, the initial data continue to collapse through horizon formation times of  $t_H \sim 0.6t_{lim}$  but with  $p$  significantly greater than the perturbative value of  $p = 2$ . Note that the evolutions of figure 2.4b have been extended to larger values of  $t_H$  to demonstrate that the evolutions

	$a$	$p$	$b$	$\chi^2/\text{d.o.f.}$
$\mu = 15, \sigma = 1.5$	$0.10 \pm 0.01$	$2.33 \pm 0.05$	$-27 \pm 4$	0.7736
$\mu = 5, \sigma = 1.7$	$0.91 \pm 0.06$	$2.07 \pm 0.02$	$-33 \pm 2$	0.5070
$\mu = 0, \sigma = 1.8$	$0.06 \pm 0.02$	$4.3 \pm 0.2$	$30 \pm 5$	1.502
$\mu = 0.5, \sigma = 1.7$ ( $t_H < 0.4t_{lim}$ )	$(4 \pm 32) \times 10^{-45}$	$73 \pm 5$	$70 \pm 2$	5.409
$(t_H > 0.72t_{lim})$	$0.02 \pm 0.03$	$5.6 \pm 0.8$	$260 \pm 20$	1.078

**Table 2.1:** Best fit parameters for the cases shown in figure 2.4 restricting to  $t_H > t_{fit} = 60$  and as noted. Listed errors ( $\pm$  values) are standard errors.  $\chi^2/\text{d.o.f.}$  is the reduced  $\chi^2$  value used as a measure of goodness-of-fit.

continue to collapse to somewhat smaller amplitude values. Figure 2.4b is also of interest because its best fit value  $p \approx 2.07 \pm 0.02$  is approximately as close to the perturbative value as several stable sets of initial data but has a smaller standard error for the fit, so the difference from the perturbative value is more significant (again, the value following the  $\pm$  is the standard error).

Figure 2.4c shows metastable evolution to  $t_H \lesssim 0.6t_{lim}$  but then a sudden jump to stability until  $t = t_{lim}$ . In the figure, the fit has been extended to the largest non-collapsing amplitude, which demonstrates that there is no collapse over a time period significantly longer than the fit predicts. This example argues that metastable data may in fact become stable at the smallest amplitudes. On the other hand, figure 2.4d shows a similar jump in  $t_H$  to values  $t_H < t_{lim}$ ; evolution at lower amplitudes shows metastable scaling with  $p \approx 5.6 \pm 0.8$  for  $360 < t_H < t_{lim}$ . The figure also shows a metastable fit with larger reduced  $\chi^2$  at larger amplitudes corresponding to  $t_{fit} < t_H < 0.4t_{lim}$ . So this is another option: metastable behavior may transition abruptly to metastable behavior with different scaling (or possibly even perturbatively unstable behavior) at sufficiently small amplitudes. It is also reasonable to classify this case as irregular due to the sudden jump in  $t_H$ ; we choose metastable due to the clean metastable behavior at low amplitudes.

Our point of view is that initial data in the metastable class is distinct from the unstable class at finite amplitudes corresponding to  $t_{fit} < t_H < 300$ ; they take longer to collapse at a fixed small value of  $\epsilon$  than would be expected by the perturbative scaling. An alternate point of view is to ask whether we can determine if a given set of initial data is perturbatively unstable in the  $\epsilon \rightarrow 0$  limit.

We have already seen that metastable initial data does not follow the perturbative scaling when fit to  $t_H = a\epsilon^{-p} + b$ , the first two terms of the perturbative expansion. However, it is possible that a perturbative description applies but requires a further subleading term. To test this hypothesis, we fit unstable and metastable initial data to  $t_H = a\epsilon^{-p} + b + c\epsilon^2$ ; as described earlier in this section, we determine if  $p$  is within two standard errors of the perturbative value  $p = 2$  (or one standard error for  $t_{fit} = 100$ ).

The unstable class of initial data is instructive. For the new fits of unstable initial data,  $p$  is statistically equal to 2, and the new values of  $a, p, b$  are consistent with the values from the old fits to within two standard errors (or sometimes slightly more). The fit value of  $c$  is uniformly within a standard error of zero, and, for the amplitude values in the fit region, the  $\epsilon^2$  term is small compared to the constant and  $\epsilon^{-2}$  terms. What is more, for some unstable initial data near the island of stability, the original  $t_H = a\epsilon^{-p} + b$  fits for  $t_{fit} = 60$  have  $p > 2$  statistically; on the other hand, the new fits have  $p = 2$  within statistical error. In other words, the perturbative expansion is still valid but requires more terms. Part of the metastable class of initial data also behaves in this manner and could therefore be reasonably considered to be perturbatively unstable. Of the metastable initial data we found, these are  $\sigma = 1.9$  for  $\mu = 0$ ,  $\sigma = 0.8$  and 1.9 for  $\mu = 0.5$ ,  $\sigma = 0.7$  for  $\mu = 1$ ,  $\sigma = 1.7$  for  $\mu = 5$ ,  $\sigma = 0.155$  for  $\mu = 10$ ,  $\sigma = 0.11$  and 1.5 for  $\mu = 15$ , and  $\sigma = 1.5$  for  $\mu = 20$ . In addition,  $\mu = 1, \sigma = 1.8$  and  $\mu = 10, \sigma = 1.7$  initial data have similar behavior, but  $p$  is not statistically consistent with 2 for any of the fit regions, though it is closer than in the original fits. On the other hand, the other metastable initial data ( $\sigma = 0.85$  and 1.8 for  $\mu = 0$ ,  $\sigma = 1.7$  and 1.8 for  $\mu = 0.5$ ,  $\sigma = 1.45$  for  $\mu = 10$ , and  $\sigma = 1.4$  for  $\mu = 20$ ) show no evidence for perturbative behavior. Specifically,  $p$  remains statistically larger than 2 for all fits, the  $\epsilon^2$  term in the new fit is roughly the same magnitude as the other terms, and the  $a, p, b$  values in the new fits are not statistically consistent with the original fits. To check if perturbative scaling might be masked by numerical errors, we have also fit these remaining metastable data ( $\sigma = 0.85, 1.8$  for  $\mu = 0$ ,  $\sigma = 1.8$  for  $\mu = 0.5$ ,  $\sigma = 1.8$  for  $\mu = 1$ ,  $\sigma = 1.45, 1.7$  for  $\mu = 10$ , and  $\sigma = 1.4$  for  $\mu = 20$ ) with  $t_H = a\epsilon^{-p} + b\epsilon^{-1} + c$ . Of these, only the  $\mu = 1, \sigma = 1.8$  and  $\mu = 10, \sigma = 1.7$  initial data have

best fit  $p$  values statistically consistent with  $p = 2$ . However, except for  $\mu = 1, \sigma = 1.8$  initial data, the best fit  $p$  values are all further from  $p = 2$  in absolute terms (usually substantially); the main effect of including the  $\epsilon^{-1}$  term is to increase the standard error on the best fit for  $p$ . Therefore, it is not clear that potential numerical errors alone can be responsible for the observed deviation from perturbative scaling. We would also point out that, even if the extra  $\epsilon^{-1}$  term turns out to be important for these initial data, the fact that it is only important at the boundary of the island of stability indicates a change in behavior for these mass/width combinations as compared to those farther from the stable region. This justifies a separate classification related to the slower entry of these mass/width combinations into the perturbative regime (as measured by horizon formation time).

## 2.4.2 Irregular behaviors

We have found a variety of irregular behaviors at the transition between the metastable and stable classes which we have classified together as irregular initial data; however, it may be better to describe them as separate classes. The stability phase diagram 2.2 indicates that the irregular class extends along the “inland” side of the small  $\sigma$  shoreline and at least part of the large  $\sigma$  shoreline of the island of stability. What is not clear from our evolutions up to now is whether each type of behavior appears along the entire shoreline or if they appear in pockets at different scalar field masses. Examples of each type of behavior that we have found appear in figure 2.5.

The first type of irregular behavior, shown in figure 2.5a, is monotonic ( $t_H$  increases with decreasing  $\epsilon$  as usual), but it is not well fit by a power law. In fact, this behavior would classify as metastable by the criterion of section 2.4.1 in that the power law of the best fit  $t_H = a\epsilon^{-p} + b$  is significantly different from  $p = 2$ , except for the fact that the reduced  $\chi^2$  value for the fit is very large (greater than 10) and also that different fitting algorithms can return significantly different fits, even though the data may appear to the eye like a smooth power law. In any case, this type of behavior apparently indicates a breakdown of metastable behavior and hints at the appearance of non-monotonicity. So far, our evolutions have not demonstrated sudden jumps in  $t_H$  typical of stability at low amplitudes,

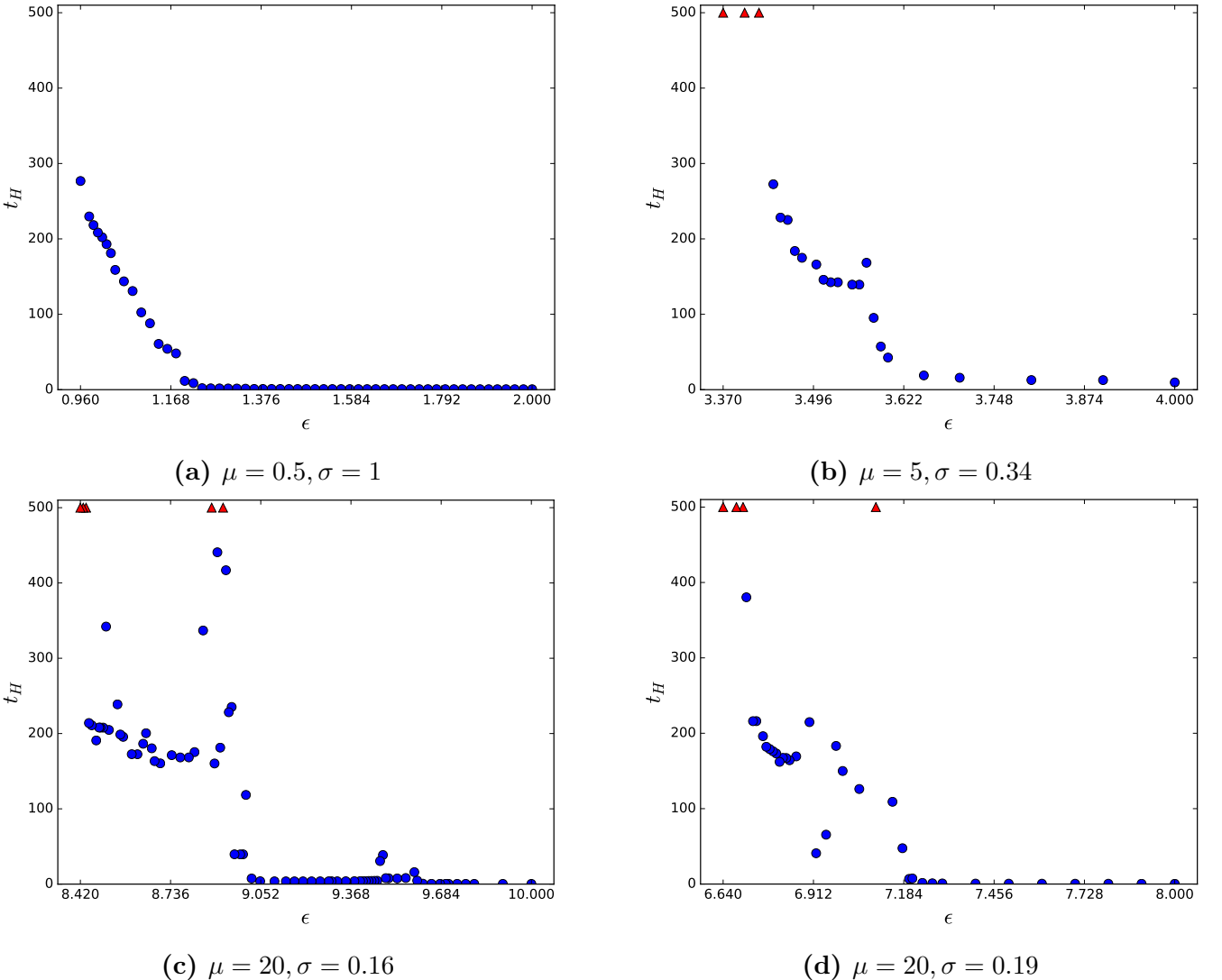


**Figure 2.5:** Irregular behavior: blue dots represent horizon formation and red triangles a lower limit on  $t_H$ .

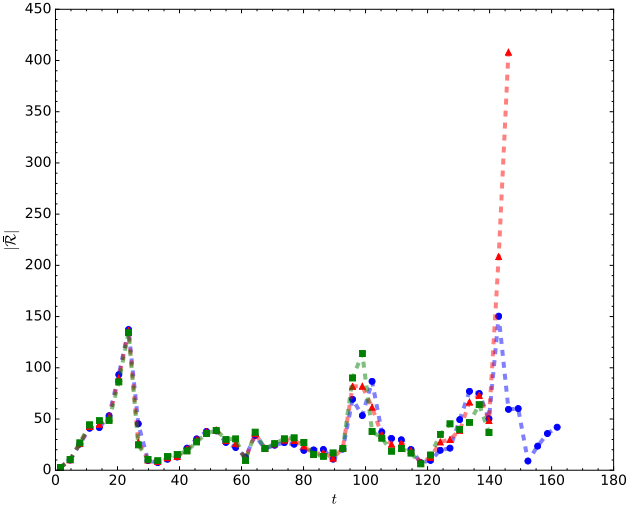
however.

Figure 2.5b exemplifies non-monotonic behavior in the irregular class. This type of behavior, which was noted already by [52], involves one or more sudden jumps in  $t_H$  as  $\epsilon$  decreases, which may be followed by a sudden decrease in  $t_H$  and then resumed smooth monotonic increase in  $t_H$ . There are suggestions that this type of initial data is stable at low amplitudes due to the usual appearance of non-collapsing evolutions, but it is worth noting that these amplitudes could instead experience another jump and decrease in  $t_H$ , just at  $t_H > t_{lim}$ . Finally, [39] studied this type of behavior in some detail, denoting it as “quasi-stable.”

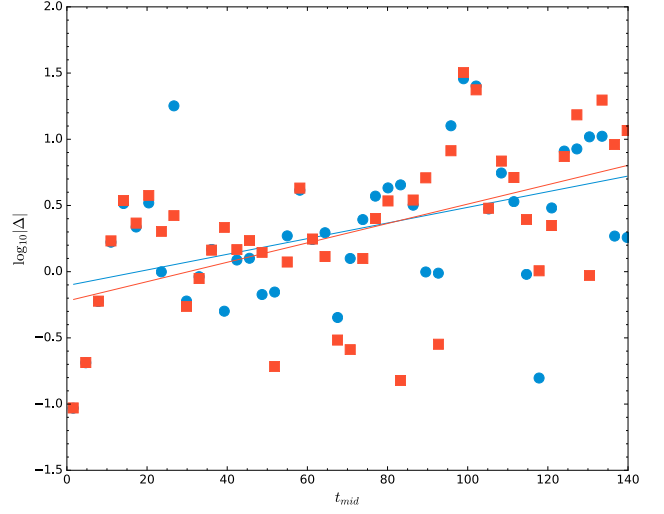
Some irregular initial data demonstrates evidence of chaotic behavior, in that  $t_H$  appears to be sensitive to initial conditions (ie, value of amplitude) over some range of amplitudes. This type of behavior appears over the range of masses (see figure 2.1d for a mild case for massless scalars), but it is more common and more dramatic at larger  $\mu$ . Figures 2.5c,2.5d represent the most extreme behavior of this type among the initial data that we studied with collapse at  $t_H < 50$  not very far separated from amplitudes that do not collapse for  $t < t_{lim}$  along with an unpredictable pattern of variation in  $t_H$ . This type of evidence for chaotic behavior has been seen previously in the collapse of transparent but gravitationally interacting thin shells in AdS [120] as well as in the collapse of massless scalars in AdS<sub>5</sub> Einstein-Gauss-Bonnet gravity [101, 114]; these references speculated that the  $t_H$  vs  $\epsilon$  curve is fractal. In both cases, this type of behavior is hypothesized to be due to the transfer of energy between two infalling shells, with horizon formation only proceeding when one shell is sufficiently energetic. In the latter case, the extra scale of the theory (given by the coefficient of the Gauss-Bonnet term in the action) leads the single initial pulse of scalar matter to break into two pulses.

We should therefore ask two questions: does this irregular behavior show evidence of true chaos, and is a similar mechanism at work here? We note first that [114] found evidence (using a modified box test) that the  $t_H$  vs  $\epsilon$  curve has a non-integer fractal dimension for plots visually similar to our figures 2.5c,2.5d. Here, to quantify the presence of chaos, we examine the difference in time evolution between similar initial conditions (nearby amplitudes), which diverge exponentially in chaotic systems. Specifically, any quantity  $\Delta$  should satisfy  $|\Delta| \propto \exp(\lambda t)$  for Lyapunov coefficient  $\lambda$ . Our characteristic will be the upper envelope of the Ricci scalar at the origin per light crossing time,  $\bar{\mathcal{R}}(t)$ . We consider three sets of irregular initial data: a massless scalar of width  $\sigma = 1.1$  with amplitudes  $\epsilon = 1.02, 1.01, 1.00$  (see figure 2.1d), a  $\mu = 5$  massive scalar of width  $\sigma = 0.34$  and  $\epsilon = 3.52, 3.51, 3.50$ , and a  $\mu = 20$  scalar of width  $\sigma = 0.19$  and  $\epsilon = 6.98, 6.95, 6.92$  (figure 2.5d). We also calculated determined the Lyapunov coefficient for unstable initial data with  $\mu = 0.5$ ,  $\sigma = 0.3$ , and  $\epsilon = 1.22, 1.20, 1.18$  for comparison.

Figure 2.6 details evidence for chaotic evolution in the  $\mu = 5, \sigma = 0.34$  case; figure 2.6a shows our



(a) Upper envelope of Ricci scalar at origin



(b)  $\log |\Delta|$  vs.  $t_{mid}$

**Figure 2.6:** Left: The upper envelope of the Ricci scalar for amplitudes  $\epsilon_1 = 3.50$  (blue circles),  $\epsilon_2 = 3.51$  (red triangles), and  $\epsilon_3 = 3.52$  (green squares) for  $\mu = 5, \sigma = 0.34$ . Right:  $\log(|\Delta_{ab}|)$  and best fit (blue circles and line) and  $\log(|\Delta_{ab}|)$  and best fit (red squares and line), calculated as a function of the midpoint  $t_{mid}$  of the time interval.

characteristic function  $\bar{R}(t)$  for the amplitudes  $\epsilon_1 = 3.50$ ,  $\epsilon_2 = 3.51$ , and  $\epsilon_3 = 3.52$ . By eye,  $\bar{R}$  shows noticeable differences after a long period of evolution. These are more apparent in figure 2.6b, which shows the log of the differences  $\Delta_{ab} \equiv \bar{R}_{\epsilon_a} - \bar{R}_{\epsilon_b}$ , along with the best fits. Although there is considerable noise — or oscillation around exponential growth — in the differences (leading to  $R^2$  values  $\sim 0.2, 0.26$  for the fits), the average slope gives Lyapunov coefficient  $\lambda = 0.007$  (within the error bar of each slope), and each slope differs from zero by more than 3 standard errors. One interesting point is that the  $t_H$  vs  $\epsilon$  curve in figure 2.5b does not appear chaotic to the eye, even though it shows some of the mathematical signatures of chaos at least for  $\epsilon_1 < \epsilon < \epsilon_3$  (the visible spike in  $t_H$  is at  $\epsilon \sim 3.57$ ).

The story is similar for the massless and  $\mu = 20$  cases we studied, which exhibit  $\lambda$  values that differ from zero by at least 1.9 standard errors; see table 2.2. This is a milder version of the behavior noted by [101, 114, 120], especially for the  $\mu = 5$  case studied. One thing to note is that the strength of oscillation in  $\log(|\Delta|)$  around the linear fit increases with increasing mass, so that the two best fit Lyapunov exponents for  $\mu = 20$  are no longer consistent with each other at the 1-standard deviation level. We should note, however that the unstable initial data with  $\mu = 0.5, \sigma = 0.3$  also exhibits a

		$\lambda$	average $\lambda$
$\mu = 0, \sigma = 1.1$	$\Delta_{12}$	$0.011 \pm 0.005$	0.011
	$\Delta_{23}$	$0.011 \pm 0.005$	
$\mu = 0.5, \sigma = 0.3$	$\Delta_{12}$	$0.021 \pm 0.0007$	0.022
	$\Delta_{23}$	$0.024 \pm 0.001$	
$\mu = 5, \sigma = 0.34$	$\Delta_{12}$	$0.006 \pm 0.002$	0.007
	$\Delta_{23}$	$0.007 \pm 0.002$	
$\mu = 20, \sigma = 0.19$	$\Delta_{12}$	$0.046 \pm 0.009$	0.032
	$\Delta_{23}$	$0.019 \pm 0.007$	

**Table 2.2:** Best fit Lyapunov coefficients  $\lambda$  for adjacent amplitude pairs and average  $\lambda$  value for each  $\mu, \sigma$  system studied. Standard errors are given following  $\pm$  signs.

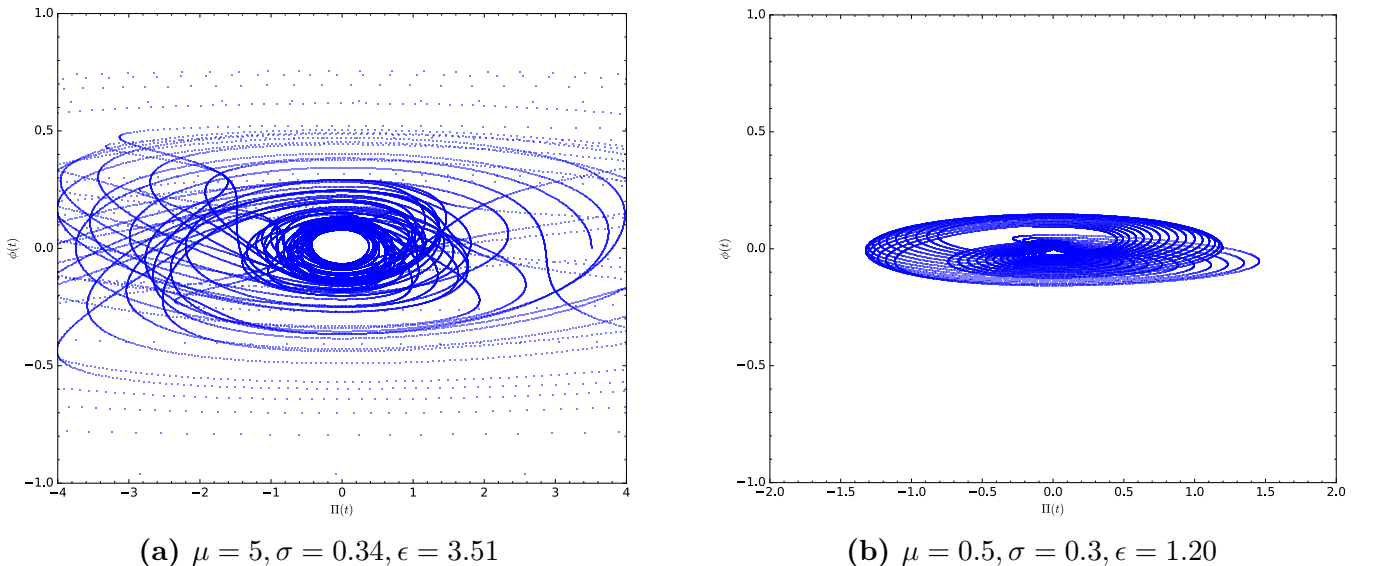


**Figure 2.7:** Trajectories in  $\Pi(x = 0), \phi(x = 0)$  phase space for one irregular and one unstable evolution. Trajectories are shown for  $t < 50$ .

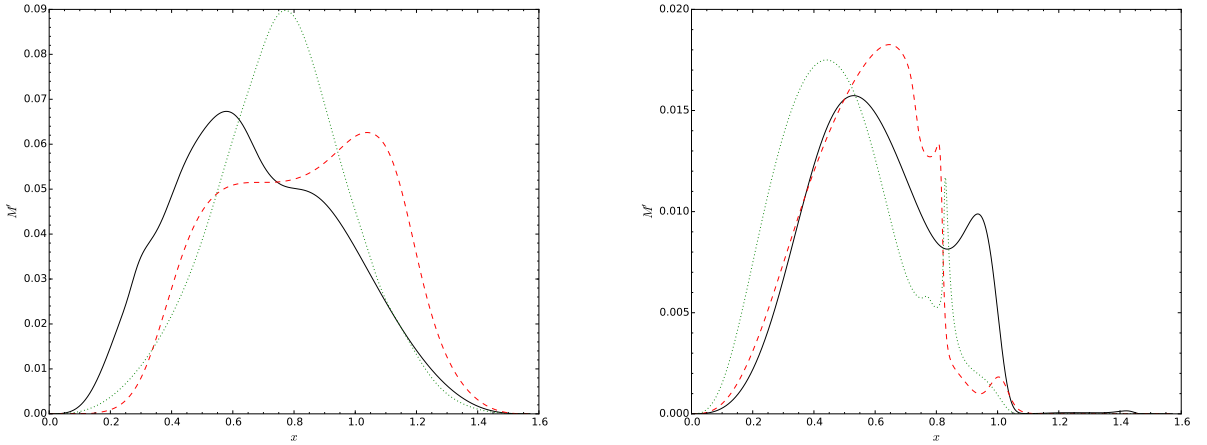
statistically positive Lyapunov exponent, though we should note that the value of  $\lambda$  quoted in table 2.2 includes the time shortly before horizon formation, which does increase  $\lambda$  somewhat (though not more than the quoted error).

Since the Lyapunov coefficients do not distinguish the irregular and unstable cases, we also consider the phase space trajectories of the evolutions. Following [121], we consider the trajectory of evolutions in  $\Pi$  and  $\phi$  evaluated at the origin for  $t \leq 50$  in figure 2.7. Neither the  $\mu = 5, \sigma = 0.34, \epsilon = 3.51$

(figure 2.7a) or  $\mu = 0.5, \sigma = 0.3, \epsilon = 1.20$  (figure 2.7b) trajectories close, though there is a clear difference. Specifically, the former trajectory is visually disorganized (that is, strongly varying orbits) with very rapid motion (seen in the gap between points on the trajectory between plotted time steps). Meanwhile, the latter motion is comparatively regular, typical of quasi-periodic motion. Figure 2.7a is typical of turbulence and clearly shows that these evolutions are nonperturbative, even though  $t_H$  is large (well into the perturbative regime for unstable initial data).

To sum up, we have identified irregular initial data that shows evidence of chaotic behavior. Specifically, several of the  $t_H$  vs  $\epsilon$  curves appear qualitatively similar to analogous plots in [101, 114, 120], which were demonstrated to have fractal-like behavior (including fractional fractal dimension in one case). Furthermore, a number of cases of irregular initial data (and some unstable) have positive Lyapunov exponents; phase space trajectories for irregular initial data show very rapid motion typical of turbulence, while unstable initial data have more regular trajectories. Taken together, this is strong evidence for chaotic behavior for some irregular initial data, similar to that discussed in other studies of gravitational collapse in AdS. Furthermore, this is the first evidence of chaos in the  $t_H$  vs  $\epsilon$  curve for gravitational collapse of a massless scalar in AdS to our knowledge.

The mechanism underlying the possibly chaotic behavior seems somewhat different or at least weaker than the two-shell or Einstein-Gauss-Bonnet systems. When examining the time evolution of the mass distributions of these data, we see a single large pulse of mass energy that oscillates between the origin and boundary without developing a pronounced peak. However, there is also apparently a smaller wave that travels across the large pulse. We can see this by comparing snapshots of the mass distribution at different times, as in figure 2.8. In the massless case examined, this wave deforms the pulse, leading to a double-shoulder appearance seen at two times in figure 2.8a. In the  $\mu = 5, \sigma = 0.34$  case, the secondary wave is more like a ripple, usually smaller in amplitude but more sharply localized, as toward the right side of the main pulse in figure 2.8b. So the chaotic behavior may be caused by the relative motion of the two waves, rather than energy transfer between two shells. In this hypothesis, a horizon would form when both waves reach the neighborhood of the origin at the same time.



**(a)**  $\mu = 0, \sigma = 1.1, \epsilon = 1.01$ , at times  $t = 60$  (solid black),  $t = 62$  (dashed red),  $t = 64$  (dotted green) **(b)**  $\mu = 5, \sigma = 0.34, \epsilon = 3.52$ , at times  $t = 132$  (solid black),  $t = 137$  (dashed red),  $t = 140$  (dotted green)

**Figure 2.8:** Radial derivative of the mass function at the indicated time for two systems that show evidence of chaos. Note the appearance of a secondary wave on top of the main pulse.  $(\mu, \sigma, \epsilon)$  as indicated.

As a note, we have run convergence tests on several sets of irregular initial data and find that our calculations are convergent overall, as expected (even at lower resolution than we used). In particular, the massless scalar evolutions studied in table 2.2 are convergent already at resolution given by  $n = 12$  (note that we typically start at  $n = 14$ ); we also observe convergent behavior for the  $\mu = 5$  evolutions discussed in table 2.2. We have therefore validated that nonmonotonic behavior and even evidence of chaos occurs. The only caveat may be for some of the apparently initial data with scalar mass  $\mu = 20$ , which nonetheless appear well-behaved according to other indicators. The reader may or may not wish to take them at face value but should recall that we have presented other chaotic initial data with rigorously convergent evolutions. See the appendix for a more detailed discussion.

## 2.5 Spectral analysis

As we discussed in the introduction, instability toward horizon formation proceeds through a turbulent cascade of energy to shorter wavelengths or, more quantitatively, to 1st-order scalar eigenmodes

with more nodes. Inverse cascades are typical of stable evolutions. Therefore, understanding the energy spectrum of our evolutions, both initially and over time, sheds light on the behavior of the self-gravitating scalar field in asymptotically AdS spacetime, providing a heuristic analytic understanding of the stability phase diagram.

The (normalizable) eigenmodes  $e_j$  are given by Jacobi polynomials as

$$e_j(x) = \kappa_j \cos^{\lambda_+}(x) P_j^{(d/2-1, \sqrt{d^2+4\mu^2}/2)}(\cos(2x)) \quad (2.8)$$

( $\kappa_j$  is a normalization constant) with eigenfrequency  $\omega_j = 2j + \lambda_+$  and  $\lambda_+ = (d + \sqrt{d^2 + 4\mu^2})/2$  in  $\text{AdS}_{d+1}$  for  $j = 0, 1, \dots$  (see [6, 122] for reviews). Including gravitational backreaction, we define the energy spectrum

$$E_j \equiv \frac{1}{2} \left( \Pi_j^2 - \phi_j \ddot{\phi}_j \right), \quad (2.9)$$

where

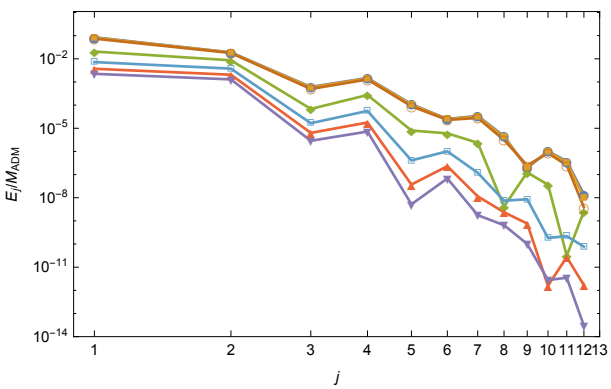
$$\begin{aligned} \Pi_j &= \left( \sqrt{A}\Pi, e_j \right), \quad \phi_j = (\phi, e_j), \\ \ddot{\phi}_j &= \left( \cot^{d-1}(x) \partial_x [\tan^{d-1}(x) A \Phi] - \mu^2 \sec^2(x) \phi, e_j \right), \end{aligned} \quad (2.10)$$

and the inner product is  $(f, g) = \int_0^{\pi/2} dx \tan^{d-1}(x) f g$ . The sum of  $E_j$  over all modes is the conserved ADM mass.

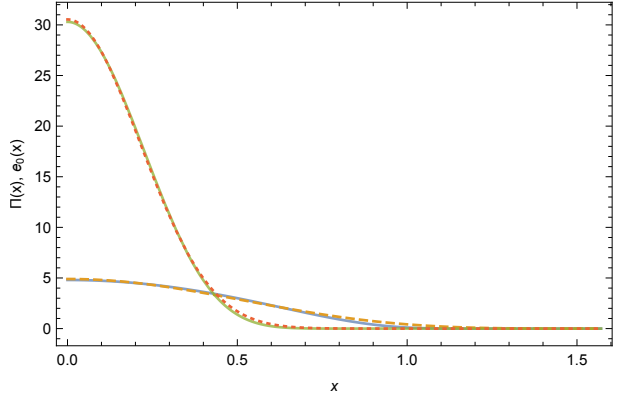
### 2.5.1 Dependence on mass

The most visibly apparent feature of the stability phase diagram of figure 2.2 is that the island of stability both expands and shifts to smaller widths as the scalar mass increases. As it turns out, the energy spectrum of the Gaussian initial data (2.7) provides a simple heuristic explanation.

It is well established both in perturbation theory and numerical studies that initial data given by a single scalar linear-order eigenmode is in fact nonlinearly stable, and the spectra of many quasi-



(a) Best fit gaussian energy spectra.



(b) Best fit gaussian and zeroth eigenmode.

**Figure 2.9:** Left: Spectra of the best fit gaussians (2.7) to the  $j = 0$  eigenmode for masses  $\mu = 0$  (blue circles), 0.5 (yellow squares), 1 (empty orange circles), 5 (green diamonds), 10 (empty cyan squares), 15 (upward red triangles), and 20 (downward purple triangles). Right: an overlay of the best fit Gaussian and  $e_0$  eigenmode for  $\mu = 0$  (solid blue is best fit, orange dashed is eigenmode) and  $\mu = 20$  (solid green, red short dashes).

periodic solutions are also dominated by a single eigenmode. As a result, we should expect Gaussian initial data that approximates a single eigenmode (which must be  $j = 0$  due to lack of nodes) to be stable. To explore how this depends on mass, we find the best fit values of  $\epsilon, \sigma$  for the  $j = 0$  eigenmode for each mass that we consider (defined by the least-square error from the Gaussian to a discretized eigenmode); this is the “best approximation” Gaussian to the eigenmode. Then we find the energy spectrum of that best-fit Gaussian; these are shown in figure 2.9a. From the figure, it is clear that the  $j = 0$  eigenmode is closer to a Gaussian at larger masses. That is, other eigenmodes contribute less to the Gaussian’s spectrum at higher masses (by several orders of magnitude over the range from  $\mu = 0$  to 20). Simply put, the shape of the  $j = 0$  eigenmode is closer to Gaussian at higher masses, which suggests that the island of stability should be larger at larger scalar field mass. Figure 2.9b compares the  $j = 0$  eigenmode and best fit Gaussian for  $\mu = 0$  and 20; on inspection, there is more deviation between the eigenmode and Gaussian for the massless scalar.

In addition, the best-fit Gaussian width decreases from  $\sigma \sim 0.8$  for a massless scalar as the mass increases. At  $\mu = 20$ , the best-fit width is  $\sigma \sim 0.31$ . This suggests that Gaussians that approximate the  $j = 0$  mode well enough are narrower in width at higher masses. An interesting point to note is that the island of stability for  $\mu = 0, 0.5$  is actually centered at considerably larger widths

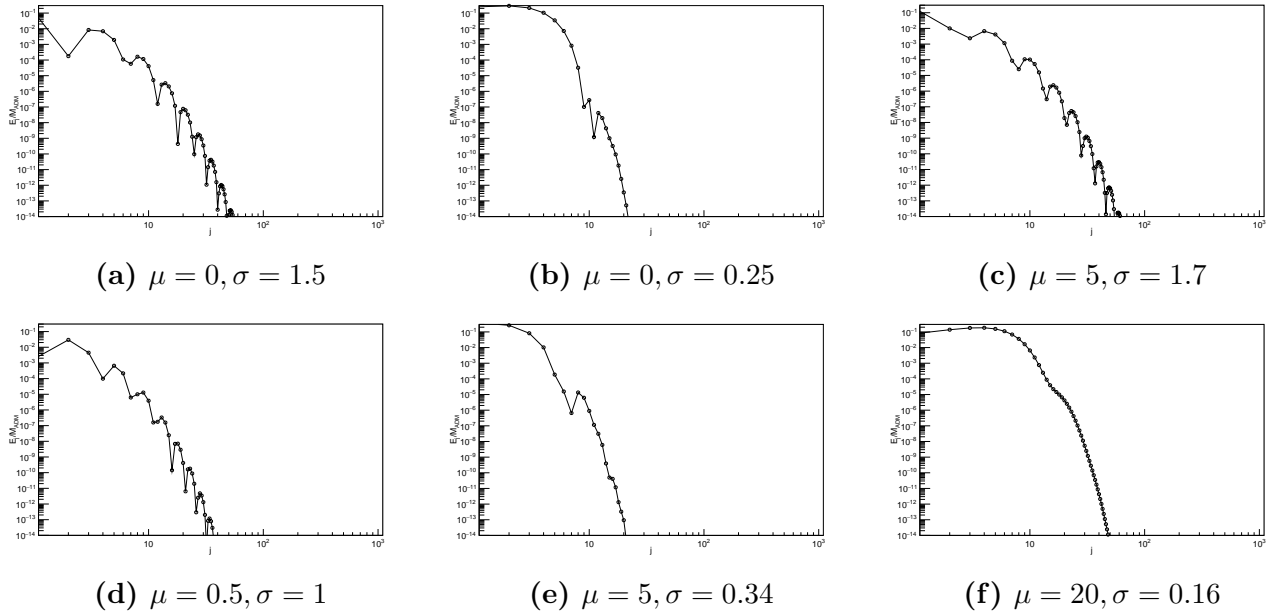


**Figure 2.10:** Initial ( $t = 0$ ) energy spectra for the indicated evolutions. In order, these represent stable, unstable, metastable, monotonic irregular, non-monotonic irregular, and chaotic irregular initial data.

than the best-fit Gaussian. This may not be surprising, since the best-fit Gaussians at low masses actually receive non-negligible contributions from higher mode numbers; moving away from the best-fit Gaussian can actually reduce the power in higher modes. For example, the stable initial data shown in figure 2.10a below has considerably less power in the  $j = 2$  mode.

### 2.5.2 Spectra of different behaviors

A key question that one might hope to answer is whether the stability class of a given  $(\mu, \sigma)$  can be determined easily by direct inspection of the initial data without requiring many evolutions at varying amplitudes. The initial energy spectra for examples of each class, including monotonic, non-monotonic, and apparently chaotic irregular behaviors, are shown in figure 2.10. These spectra are taken from among the smallest amplitudes we evolved in order to minimize backreaction effects.

Unfortunately, the initial energy spectra do not seem to provide such a method for determining the stability class. Very broadly speaking, stable and metastable  $(\mu, \sigma)$  correspond to initial spectra that drop off fairly quickly from the  $j = 0$  mode as  $j$  increases, while unstable and irregular behaviors

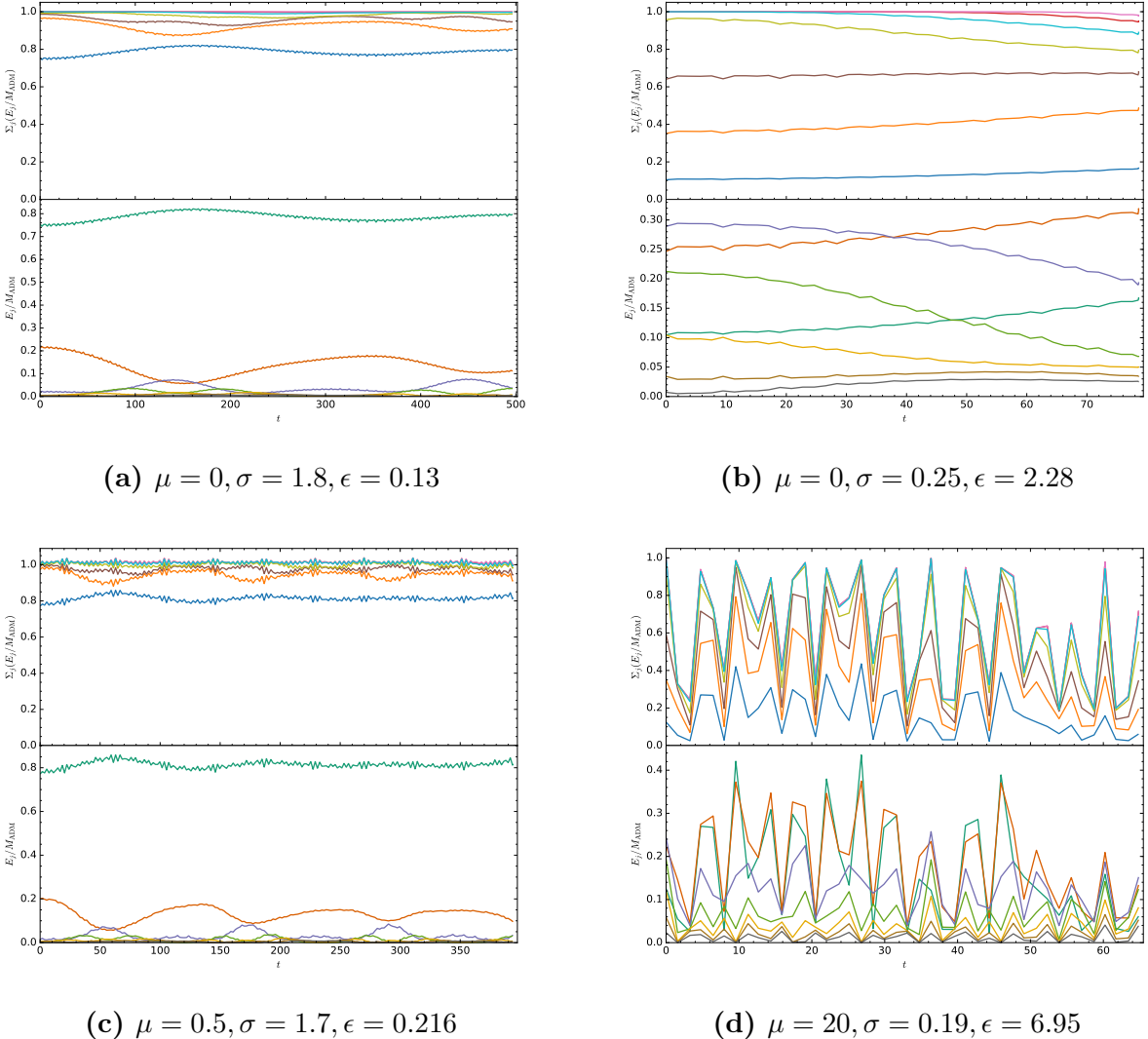


**Figure 2.11:** The time dependence of the energy spectra as a fraction of the total ADM mass for the indicated  $\mu, \sigma, \epsilon$ . Lower panels show the lowest 7 modes (in colors cyan, red, purple, green, yellow, brown, and gray respectively). Upper panels show cumulative energy to mode  $j = 0, 1, 2, 4, 8, 16, 32$  (in colors blue, orange, brown, yellow, aqua, red, and magenta).

tend to have roughly constant or even slightly increasing spectra up to  $j = 5$  or 10. However, figure 2.10d shows that some irregular initial data have spectra that decrease rapidly after a small increase from  $j = 1$  to  $j = 2$ . Kinks in the spectrum are more prevalent for widths of the AdS scale or larger, while spectra for smaller widths tend to be smoother.

### 2.5.3 Evolution of spectra

While the initial spectrum for a given  $(\mu, \sigma)$  pair does not have predictive value regarding the future behavior as far as we can tell, the time dependence of the spectrum throughout the evolution of the system is informative. Figure 2.11 shows the time-dependence of spectra for examples of the stable, unstable, metastable, and chaotic irregular classes. In each figure, the lower panel shows the fraction  $E_j/M_{ADM}$  in each mode up to  $j = 6$ , while the upper panel shows the cumulative fraction  $\sum_j E_j/M_{ADM}$  to the mode  $2^k$  with  $k = 0$  to 5.

The difference between stable evolution in figure 2.11a and unstable evolution in figure 2.11b is readily apparent. As the evolution proceeds, we expect a cascade of energy into higher mode numbers, but inverse cascades to lower modes can also occur. The stable evolution shows a slow pattern of cascades and inverse cascades, in fact. On the other hand, the unstable evolution shows a nearly monotonic cascade of energy into the highest modes along with a simultaneous cascade of energy into the lowest modes (therefore depleting intermediate modes). These are common observations in the literature and are included here for completeness.

The metastable evolution shown in figure 2.11c is interesting in light of the stable and unstable spectra. The amplitude shown is from the “unstable” portion of figure 2.4d, the part consistent with the perturbative scaling  $t_H \sim \epsilon^{-2}$ . However, the spectrum shows a similar pattern of slow cascades and inverse cascades to the stable initial data example, though on a somewhat faster time scale in this case. While perhaps surprising, this is in keeping with the similarities noted between the initial spectra in figures 2.10a and 2.10c. We have also checked that the time-dependent spectrum at a higher amplitude with  $t_H \sim 100$  follows the same pattern as 2.11c; in fact, it looks essentially the same but simply ends at an earlier time. This lends some credence to the idea that metastable initial data is stable at lowest nontrivial order in perturbation theory, with instability triggered by higher-order corrections. Alternately, the instability could be caused by an oscillatory singularity in the perturbative theory, as discussed in [106, 110–112] in the case of two-mode initial data. These divergences do not appear in the energy spectrum.

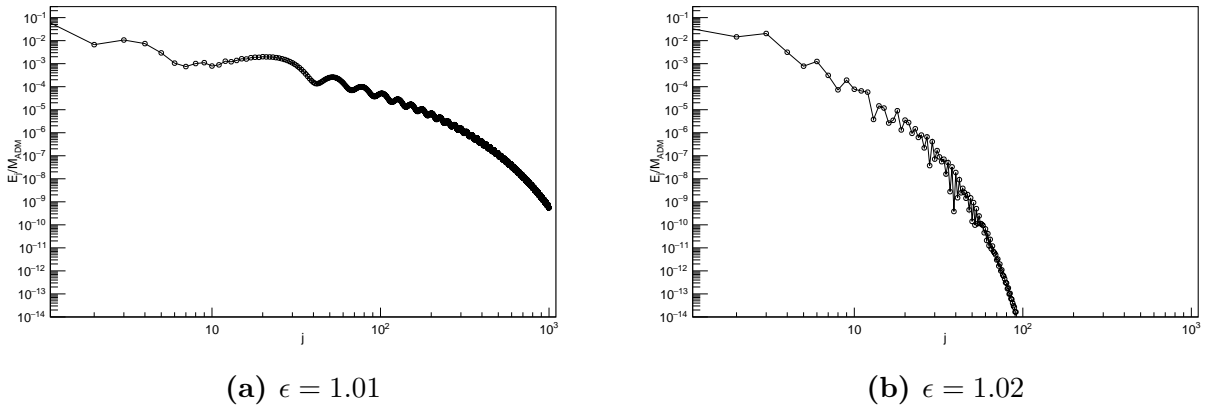


**Figure 2.12:** Spectra at time  $t \approx 71$  for  $\mu = 0, \sigma = 1.1$  for the two amplitudes given.  $\epsilon = 1.01$  forms a horizon at  $t_H \approx 71.1$ ,  $\epsilon = 1.02$  at  $t_H \approx 248.0$ .

Figure 2.11d shows the time-dependence of the spectrum in an irregular evolution, specifically  $\mu = 20, \sigma = 0.19$  at  $\epsilon = 6.95$ , which is in the chaotic region of the  $t_H$  vs  $\epsilon$  plot in figure 2.5d. There is rapid energy transfer among modes, including cascades out of and inverse cascades into mode numbers  $j \leq 32$  over approximately a light-crossing time. It is easy to imagine that horizon formation might occur at any of the cascades of energy into higher modes, leading to seemingly random jumps in  $t_H$  as a function of amplitude.

Finally, the time-evolved energy provides another possible measure of approximate thermalization in the dual CFT; namely, the spectrum should approach an (exponentially cut-off) power law at thermalization. In most cases, this occurs shortly before horizon formation, but there are exceptions, such as the late time behavior of initial data below the critical mass for black hole formation in Einstein-Gauss-Bonnet gravity [114]. When there is evidence of chaotic behavior, it is particularly interesting to know if the spectra for similar amplitudes approach a power law at similar times even if horizons form at very different times. Figure 2.12 shows the energy spectra for two amplitudes in the chaotic region of the  $t_H$  vs  $\epsilon$  plot for  $\mu = 0, \sigma = 1.1$ . Figure 2.12a is the spectrum just before horizon formation for  $\epsilon = 1.01$ , while figure 2.12b is the spectrum at approximately the same time for  $\epsilon = 1.02$ , which is very long before horizon formation. In this example, we see that the spectrum does approach a power law for the evolution that is forming a horizon, while the other evolution demonstrates a more rapid decay (typically fit by a power law times an exponential in the

literature). Therefore, this example suggests that a power law spectrum may yield similar results to horizon formation as a measure of thermalization in the dual CFT.

## 2.6 Discussion

For the first time, we have presented the phase diagram of stability of  $\text{AdS}_5$  against horizon formation, treating the scalar field mass  $\mu$  and width  $\sigma$  of initial data as free parameters. In addition to mapping the location of the so-called “island of stability,” we have gathered evidence for two non-perturbative classes on the “shorelines” of the island, the metastable and irregular classes. While these must either exhibit stability (no collapse below some critical amplitude) or instability (collapse at arbitrarily small but finite amplitude) as the amplitude  $\epsilon \rightarrow 0$ , they are distinguished by their behavior at computationally accessible (finite) amplitudes. While perturbatively unstable evolutions obey  $t_H \propto \epsilon^{-2}$  as  $\epsilon \rightarrow 0$  (and show evidence of this behavior at finite  $\epsilon$ ), metastable initial data follows  $t_H \propto \epsilon^{-p}$  for  $p > 2$  over a range of amplitudes  $\epsilon > 0$ . The irregular class is characterized by horizon formation times  $t_H$  that are not well described by a power law and sometimes exhibit non-monotonicity or even evidence of chaos. Both of these classes appear across the range of  $\mu$  values that we study and at both small- and large-width boundaries of the stable class of initial data.

At this time, it is impossible to say whether metastable initial data is stable or unstable as  $\epsilon \rightarrow 0$  (or if all metastable data behaves in the same way in that limit). Our numerical evolutions include cases in which the lowest amplitudes jump either to metastable scaling with smaller  $p$  or to evolutions that do not collapse over the timescales we study. We did find evidence that many metastable profiles move toward perturbatively unstable scaling ( $t_H \propto \epsilon^{-2}$ ) as  $\epsilon \rightarrow 0$  but more slowly than the initial data that we have classified as unstable. It is also possible that some metastable initial data is stable in the perturbative theory (ie, to  $\epsilon^3$  order in a perturbative expansion) but not at higher orders. We emphasize once again, however, that our interest and therefore our classification is in small but finite  $\epsilon$  behavior (which is by definition not strictly in the perturbative regime).

The irregular class seems likely to be (mostly) stable at arbitrarily small amplitudes based on our numerical evolutions, though we have not found a critical amplitude for monotonic irregular initial data. The irregular initial data includes the “quasi-stable” initial data described in [39, 52], which has a sudden increase then decrease in  $t_H$  as  $\epsilon$  decreases as well as evidence for chaotic behavior. In fact, we have found evidence for weakly chaotic behavior for non-monotonic initial data in the form of a small but nonzero Lyapunov coefficient and in the phase space trajectory. Both non-monotonicity and chaos become stronger and more common at larger scalar masses; however, we have also found evidence of chaotic behavior for the massless scalar including in the  $t_H$  vs  $\epsilon$  curve. To our knowledge, this is the first evidence of chaos in this relationship for spherically symmetric massless scalar collapse in AdS, which is particularly interesting because there is only one physically meaningful ratio of scales,  $\sigma$  as measured in AdS units.

While we have emphasized the appearance of new behaviors outside perturbation theory, metastable and irregular initial data are interesting potential subjects for analysis in the multiscale perturbation theory. A key question is if they demonstrate any unusual behavior there or map directly onto the stable or unstable classes.

Aside from the ultimate stability or instability of metastable and irregular initial data, several questions remain. For one, black holes formed in massive scalar collapse in asymptotically flat spacetime exhibit a mass gap for initial profiles wider than the Compton wavelength  $1/\mu$  [123]. Whether this mass gap exists in AdS is not clear, and it may disappear through repeated gravitational focusing as the field oscillates many times across AdS; investigating this type of critical behavior will likely require techniques similar to those of [124]. Returning to our stability phase diagram, the physical mechanism responsible for chaos that seems to occur for some irregular initial data is not yet clear. Is it some generalization of the same mechanism as found in the two-shell system? Also, would an alternate definition of approximate thermalization in the dual CFT, such as development of a power-law spectrum, lead to a different picture of the stability phase diagram? Finally, the big question is whether there is some test that could be performed on initial data alone that would predict in advance its behavior? So far, no test is entirely successful, so new ideas are necessary.

**Acknowledgments** We would like to thank Brayden Yarish for help submitting jobs for the  $\mu = 10$  evolutions. The work of ND is supported in part by a Natural Sciences and Engineering Research Council of Canada PGS-D grant to ND, NSF Grant PHY-1606654 at Cornell University, and by a grant from the Sherman Fairchild Foundation. The work of BC and AF is supported by the Natural Sciences and Engineering Research Council of Canada Discovery Grant program. This research was enabled in part by support provided by WestGrid ([www.westgrid.ca](http://www.westgrid.ca)) and Compute Canada Calcul Canada ([www.computecanada.ca](http://www.computecanada.ca)).

# Appendix

## 2.A Convergence Testing

Due to the large number of evolutions we have carried out, it is not computationally feasible to test all of them for convergence. Therefore, we have checked several interesting cases of irregular initial data, which are the most curious. These are carried out by evolving the initial data with a base resolution  $n = 14$  and again at  $n = 15, 16$  with commensurate time steps, as described in [39]. In the cases indicated, we evaluated the order of convergence at lower resolutions. We remind the reader that the order of convergence  $Q$  is the base-2 logarithm of the ratio of  $L^2$  errors (root-mean-square over all corresponding grid points) between successive pairs of resolutions. We also note that the initial data is defined analytically, so  $Q$  can appear poor at  $t = 0$  since the errors are controlled by round off; in some cases,  $Q$  is therefore undefined and not plotted.

First, we carried out convergence tests for mass  $\mu = 0.5$ , width  $\sigma = 1$ , and amplitude  $\epsilon = 1.12$ , which is monotonic irregular initial data presented in figure 2.5a. This amplitude collapses with  $t_H \sim 88$ . Figure 2.A.1a shows the ( $L^2$  norm) order of convergence for the field variable  $\phi$ , the mass function  $M$ , and the metric functions  $A, \delta$ . While the order of convergence is initially poor and even negative, all these variables show approximately fourth order convergence for times  $t \gtrsim 70$ . The reason for the initially poor convergence is that the error between successive resolutions is already given by (machine limited) round off. As a demonstration, we tested the order of convergence with base resolution  $n = 12$ , as shown in figure 2.A.1b. The variables show order of convergence  $Q \gtrsim 3$  already at this resolution for most of the evolution, losing convergence only for  $t > 80$ , where we

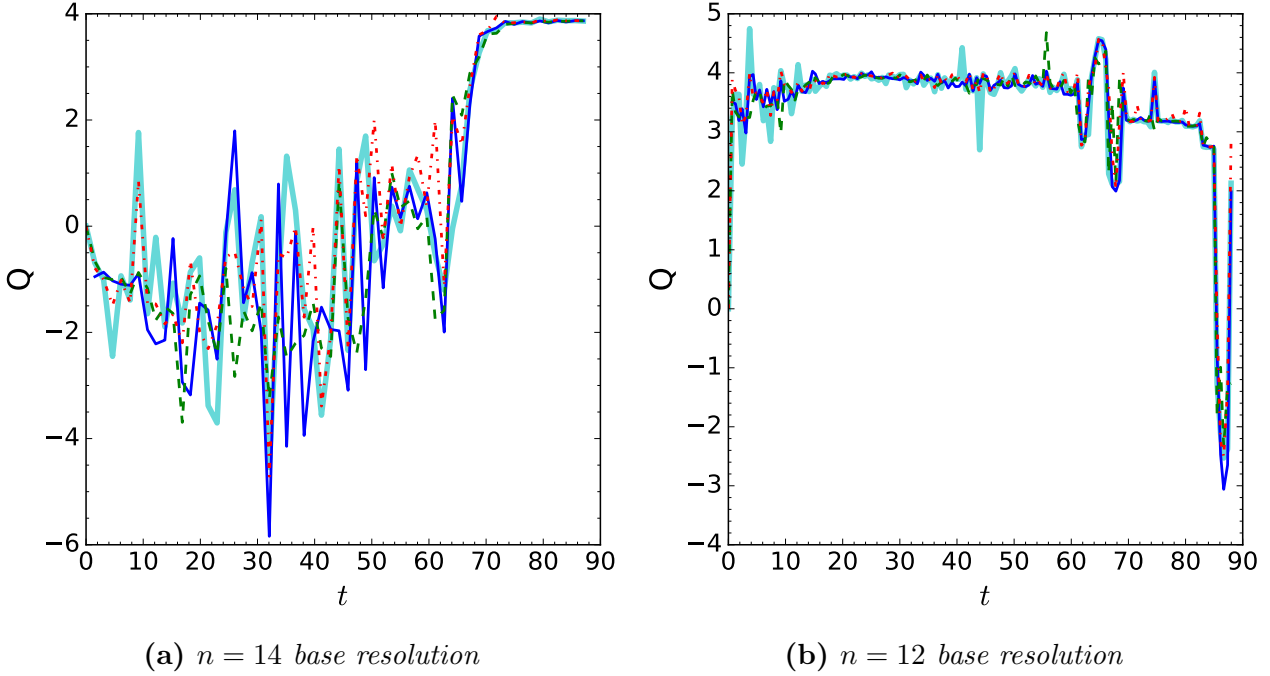


**Figure 2.A.1:** Convergence results for  $\mu = 0.5$ ,  $\sigma = 1$ ,  $\epsilon = 1.12$  showing order of convergence  $Q$  vs time for  $\phi, M, A, \delta$  (blue thin solid line, green dashed line, red dash-dotted line, cyan thick solid line, respectively). Left: Resolutions  $n = 14, 15, 16$  used. Right: Resolutions  $n = 12, 13, 14$  used.

see approximately 4th-order convergence in the  $n = 14$  resolution computations.

Two of the authors have discussed the convergence properties of evolution for the nonmonotonic irregular initial data with  $\mu = 20, \sigma = 0.1, \epsilon = 11.74$ , which is in an amplitude region of increased  $t_H$  surrounded by smaller values, in detail in [39]. In short, the variables  $\phi, M, A, \delta$  all exhibit fourth order convergence, as does  $\Pi^2(t, 0)$ , and the conserved mass actually has 6th order convergence.

Initial data for  $\mu = 15, \sigma = 0.2$  is also nonmonotonic, as shown in figure 2.A.2a. While we have not analyzed all aspects of the convergence, we see from the remainder of figure 2.A.2 that  $\phi, M, A, \delta$  exhibit convergent behavior at better than second order for  $\epsilon = 7.42$  (figure 2.A.2b, second-largest value of  $t_H$  in figure 2.A.2a) and  $\epsilon = 7.40$  (figure 2.A.2c, adjacent amplitude in figure 2.A.2a). It is important to note that the larger amplitude also has the larger horizon formation time, contrary to the usual monotonic behavior. In other words, we have validated the nonmonotonicity of this initial data through convergence testing.

It is most crucial to validate the convergence of chaotic evolutions. In table 2.2, we noted that

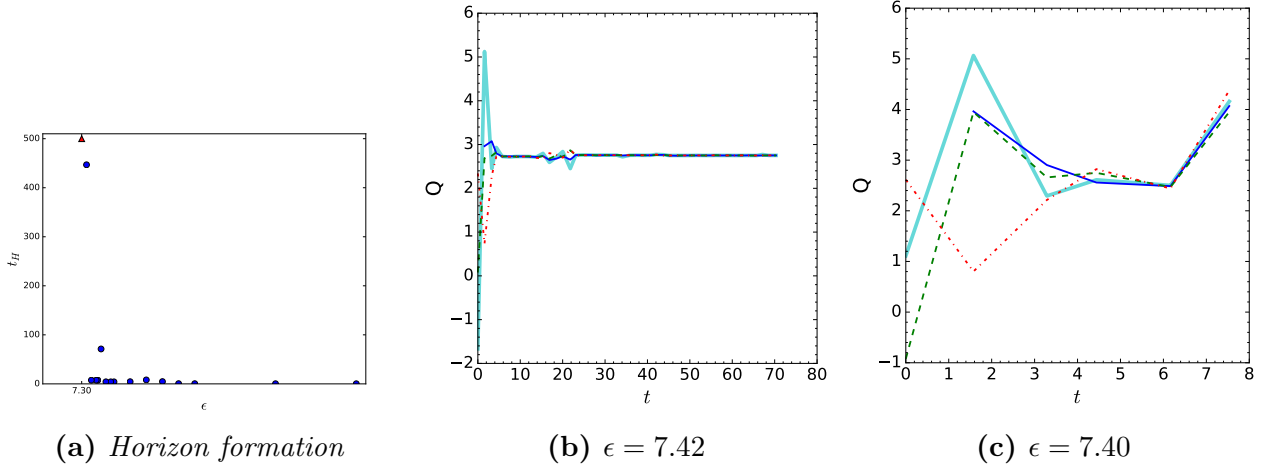


**Figure 2.A.2:** Convergence results for  $\mu = 15$ ,  $\sigma = 0.2$ . Left:  $t_H$  vs  $\epsilon$ . Middle & Right: order of convergence vs time for  $\phi, M, A, \delta$  (blue thin solid line, green dashed line, red dash-dotted line, cyan thick solid line, respectively) for indicated amplitudes.

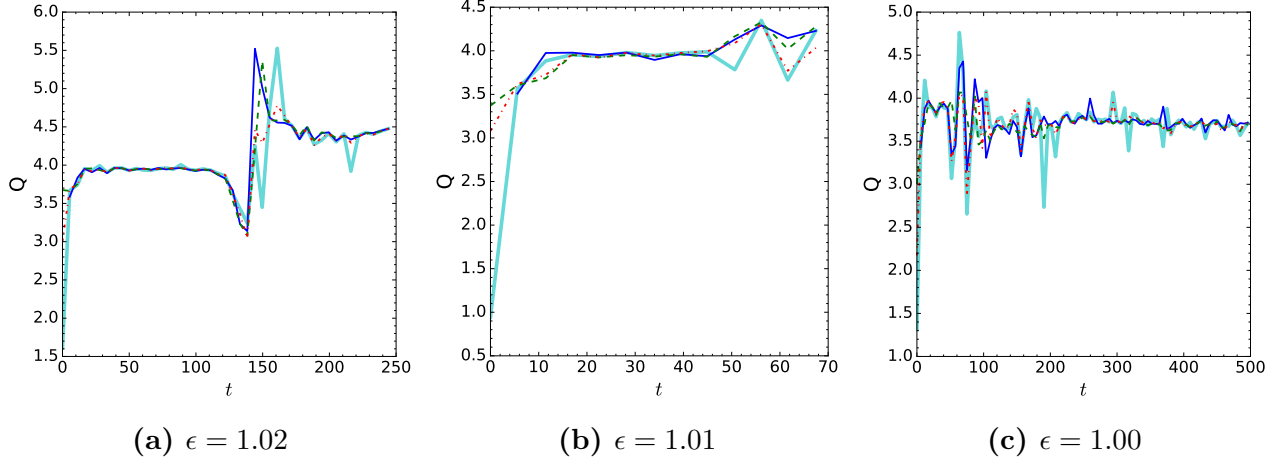


**Figure 2.A.3:** Convergence results for  $\mu = 0$ ,  $\sigma = 1.1$  for listed amplitudes showing order of convergence  $Q$  vs time for  $\phi, M, A, \delta$  (blue thin solid line, green dashed line, red dash-dotted line, cyan thick solid line, respectively); resolutions  $n = 12, 13, 14$ .

the Ricci scalar at the origin has nonzero Lyapunov exponent at almost the 2 sigma level for amplitudes  $\epsilon = 1.02, 1.01, 1.00$  for  $\mu = 0, \sigma = 1.1$ . We show the results of convergence tests for these amplitudes in figure 2.A.3; because these are longer evolutions, we consider the convergence at the lower resolutions  $n = 12, 13, 14$ . After a transient start-up period, these are all convergent with  $Q > 2.5$  for all variables considered at all times; for most of the time, the order of convergence is  $Q > 3.5$ . It is worth noting that one of the amplitudes does not form a horizon through  $t = 500$ . These convergence tests validate both the nonmonotonic nature of the evolution ( $t_H \approx 248, 71$  and

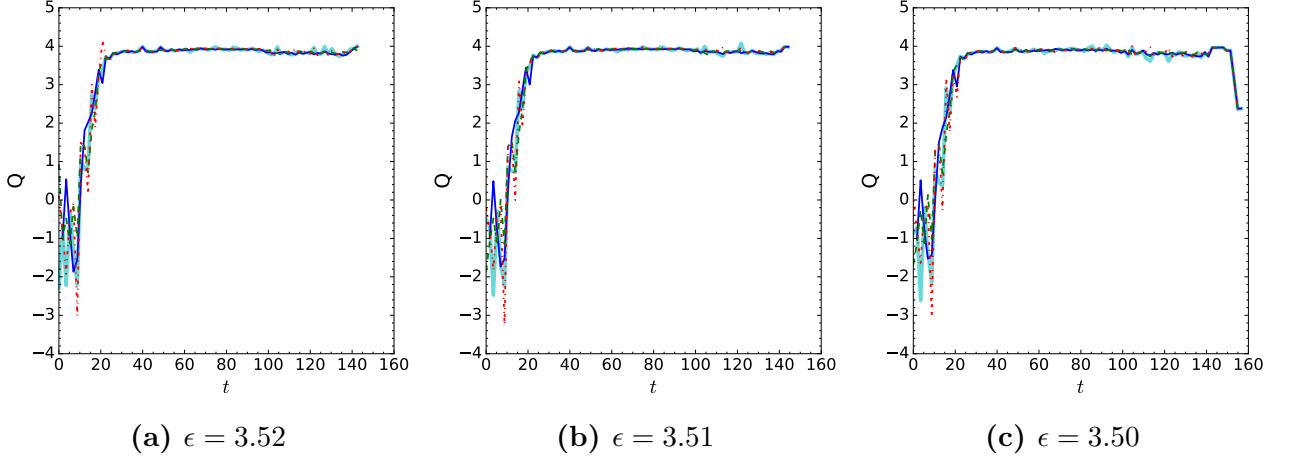


**Figure 2.A.4:** Convergence results for  $\mu = 5$ ,  $\sigma = 0.34$  for listed amplitudes showing order of convergence  $Q$  vs time for  $\phi, M, A, \delta$  (blue thin solid line, green dashed line, red dash-dotted line, cyan thick solid line, respectively); resolutions  $n = 14, 15, 16$ .

$> 500$  for  $\epsilon = 1.02, 1.01, 1.00$  respectively) and also the calculation of the Lyapunov coefficient.

Also in table 2.2, we found a nonzero Lyapunov exponent for  $\mu = 5, \sigma = 0.34$  at amplitudes  $\epsilon = 3.52, 3.51, 3.50$ . The results of convergence tests for these amplitudes appear in figure 2.A.4. For  $t \gtrsim 20$ , these evolutions exhibit convergent behavior with  $Q > 3.5$  (and always  $Q > 2$ ). At early times, the apparent poor convergence is again due to the errors being dominated by round-off; we have carried out additional convergence tests (not shown) and verified that these evolutions are already convergent with order of convergence close to  $Q = 4$  at base resolutions  $n = 12$  for  $t \lesssim 20$ . Again, convergence tests validate chaotic behavior for these initial data.

Initial data with  $\mu = 1, \sigma = 1$  is chaotic over a narrow range of amplitudes. We have carried out convergence testing for amplitudes  $\epsilon = 1.15, 1.14$ , which are the two amplitudes with  $t_H < 100$  between amplitudes with  $t_H \gtrsim 150$  in figure 2.A.5a. The order of convergence was poor for these amplitudes in our initial tests with base resolution  $n = 14$  because the error between resolutions was dominated by round-off, similar to the convergence tests we discussed above for  $\mu = 0.5, \sigma = 1$ . In subsequent tests with lower resolutions  $n = 11, 12, 13$ , we find an order of convergence  $Q \sim 4$  for most of the evolutions (and always  $Q > 3$ ). It is important to note again that our evolutions exhibit convergence while showing horizon formation at a later time for a larger amplitude in this case, again validating the nonmonotonic behavior.

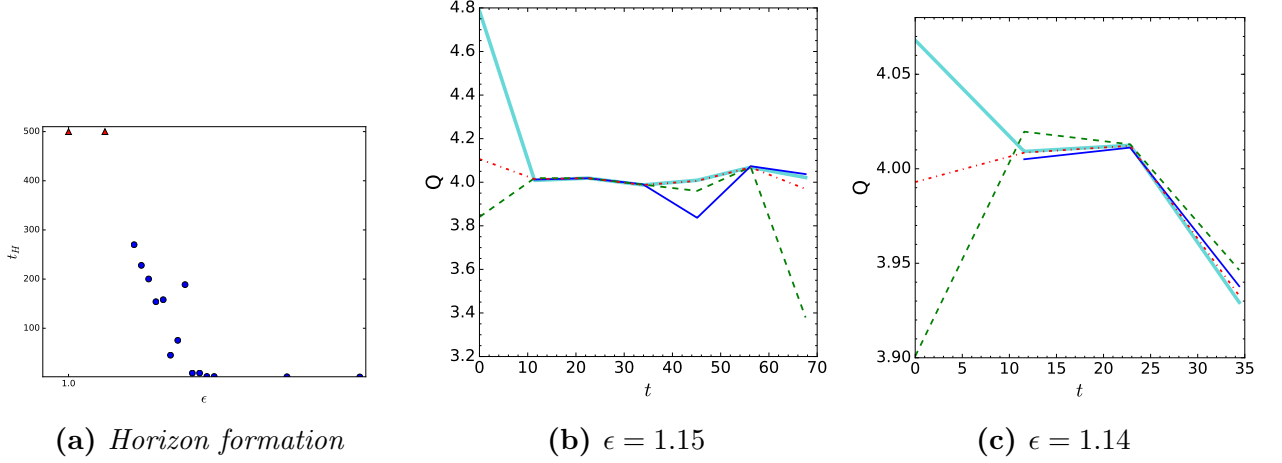


**Figure 2.A.5:** Convergence results for  $\mu = 1$ ,  $\sigma = 1$ . Left:  $t_H$  vs  $\epsilon$ . Middle & Right: order of convergence  $Q$  vs time for  $\phi, M, A, \delta$  (blue thin solid line, green dashed line, red dash-dotted line, cyan thick solid line, respectively); resolutions  $n = 11, 12, 13$ .

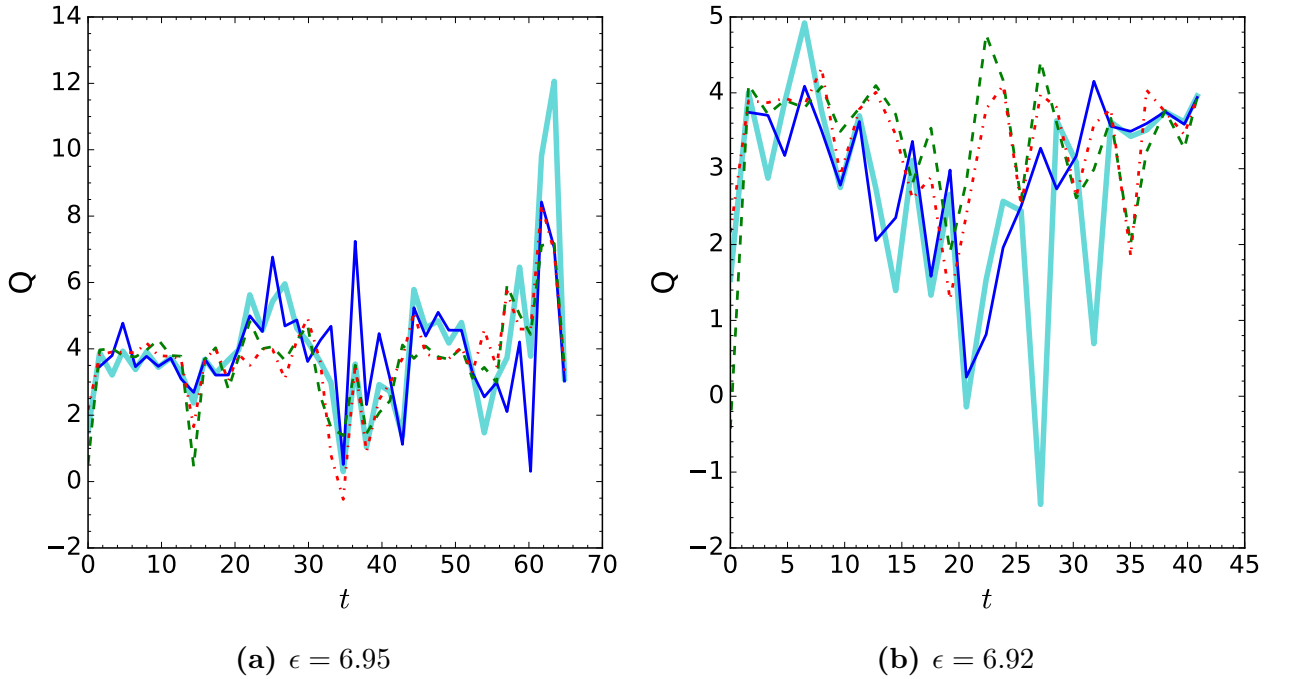


**Figure 2.A.6:** Order of convergence vs time for  $\phi, M, A, \delta$  (blue thin solid line, green dashed line, red dash-dotted line, cyan thick solid line, respectively) for  $\mu = 20$ ,  $\sigma = 0.19$  and indicated amplitudes.

Finally, we ran convergence tests for the chaotic initial data with  $\mu = 20$ ,  $\sigma = 0.19$  for  $\epsilon = 6.95, 6.92$ , with  $t_H \approx 65.5, 40.8$  respectively. As shown in figure 2.A.6, the simulations are close to fourth order convergence for most of the evolution, but there are periods where the order of convergence for evolution and constraint variables becomes negative. This of course leads to the concern that the evolutions should have collapsed during those periods and extend into an “afterlife” evolution.

We have therefore evolved these amplitudes through these regions (approximately  $t = 30 - 40$  for  $\epsilon = 6.95$  and  $t = 18 - 30$  for  $\epsilon = 6.92$ ) at high resolution ( $n = 18$ ). If the evolutions are truly in an afterlife, this higher resolution calculation may include horizon formation. We do not observe this. Another tell-tale of would-be horizon formation is a decrease in the timestep size by an order of magnitude or more followed by an increase. We monitor the timestep size every 500 timesteps through this evolution but do not observe a decrease in timestep size by more than a factor of 2. As a result, we believe the values of  $t_H$  found are reliable, though the reader may wish to consider them with some caution. In other words, while convergence testing is the gold standard to validate our numerical evolutions, there are other indicators of reliability, which these evolutions satisfy. It is also worth noting that the rapid energy transfer characteristic of figure 2.11d for  $\epsilon = 6.95$  begins immediately and is therefore seen in a convergent region of the evolutions, particularly for  $t \lesssim 14$ . Nonetheless, we emphasize that we have found convergent evolutions for irregular initial data at scalar masses from  $\mu = 0$  to 20. It is important to note that we have validated nonmonotonic behavior in plots of  $t_H$  vs  $\epsilon$ . Convergence testing also specifically validates the evolutions used to find a nonzero Lyapunov coefficient (at nearly the  $2\sigma$  level) for massless scalar collapse.

# 3 Perturbative Stability of Massless Scalars in AdS<sub>4</sub>

Having examined the collapse of massive scalars fields in AdS<sub>5</sub>, we now wish to explore the perturbatively stable solutions for massless scalars. These solutions resist gravitational collapse and give analytic descriptions of the direct and inverse energy cascades that must be balanced for stability to be achieved.

The Two-Time Formalism (TTF) allows for renormalization flow equations that absorb secular terms into renormalized integration constants in the first-order solution for the scalar field. These flow equations become algebraic under a quasi-periodic (QP) ansatz for the amplitudes and phases. While the TTF theory technically involves an infinite sum of terms, by truncating the series to a finite  $j_{max}$  value, numerical values for the amplitudes and phases can be calculated. How the truncation value affects the space of solutions, and the limits of the solution space itself, remains to be addressed.

## 3.1 Contributions of Authors

In this collaboration, QP solutions to (3.19) were found numerically through programs initially written by N. Deppe, but later expanded and developed by myself. In particular, I developed code to achieve the tail fitting and seeding procedure detailed in appendix 3.A that allowed for solutions to (3.19) to be developed for  $j_{max}$  values of several hundred – almost an order of magnitude greater than the solutions previous found in the literature. Implementation of the high temperature perturbation method outlined in 3.5 was done using code I developed, as was the procedure of reoptimization that

allowed for the high temperature solution to be projected back to the QP solution surface at various frequencies. Finally, I developed the constant- $T$  solution finding method using a Newton-Raphson solver. Evolution of the solutions was based on numerical methods initially developed by N. Deppe, then further developed by me. All data management and analysis was done using programs I wrote.

Much of the numerical work for this project was done using the University of Winnipeg's tesla server, where CPU hours are not tracked. However, for larger systems increased computing power was required, which necessitated transferring all code to Compute Canada's new Cedar cluster. Once there, I used 5.43 CPU years' worth of computing power to run evolutions and analysis of the results. Finally, I have written the manuscript, with input from the other authors, that appears here.

As is common for these types of projects, all members of the collaboration were equally involved in the interpretation of the data, as well as the late stages of editing. Authors are listed alphabetically and it is understood that all members contribute equally to the publication.

# On the Stability of High-Temperature, Quasi-Periodic Solutions for Massless Scalars in AdS<sub>4</sub>

To Appear on [arxiv.org](https://arxiv.org)

Brad Cownden<sup>1</sup>, Nils Deppe<sup>2</sup>, and Andrew R. Frey<sup>1,3</sup>

<sup>1</sup>*Department of Physics & Astronomy,*

*University of Manitoba*

*66 Chancellors Cir, Winnipeg, Manitoba R3T 2N2, Canada*

<sup>2</sup>*Cornell Center for Astrophysics and Planetary Science and Department of Physics,*

*Cornell University*

*122 Sciences Drive, Ithaca, New York 14853, USA*

<sup>3</sup>*Department of Physics and Winnipeg Institute for Theoretical Physics,*

*University of Winnipeg*

*515 Portage Avenue, Winnipeg, Manitoba R3B 2E9, Canada*

We examine a family of numerical solutions in the Two-Time Formalism (TTF) description of massless scalars in AdS<sub>4</sub> parameterized by the dimensionless parameter  $T$ . Numerical solutions can only be found by truncating a sum over frequency components to some finite number. However, any numerical solution must be robust against an increase in the number of frequencies. We extensively verify the robustness of such solutions against truncation, and over a range of  $T$ . We find that solutions with low values of  $T$  are in general robust as the number of modes is increased, while solutions with higher values of  $T$  are not. Finally, we examine the evolution of possible quasi-periodic solutions within the TTF description and show that low- $T$  solutions maintain their quasi-periodicity while higher  $T$  solutions do not.

## 3.2 Introduction

The question of the nonperturbative stability of  $(d+1)$ -dimensional Anti-de Sitter spacetime against horizon formation has been examined extensively, both as a question of mathematical physics and given its application to the AdS/CFT correspondence; see reviews such as [125]. Beginning with the seminal work of [67], others (including [64, 68–70, 126]) have repeatedly demonstrated the generic instability of spherically symmetric  $\text{AdS}_{d+1}$  gravity minimally coupled to a scalar field. The primary driver of the instability in the fully nonlinear system is the turbulent flow of energy to short length scales. However, [58, 87, 108] and others have shown that some initial conditions in asymptotically AdS spacetimes resist gravitational collapse; these conditions form islands of stability in the space of initial data. As these islands of stability continue to be explored, more subtle behaviours continue to be identified, particularly along the “shorelines” [39, 86, 88, 120]. Within the stability islands are various solutions created from exciting a single linear mode, known as oscillons or breathers for real scalars [50, 58, 64, 67], boson stars for complex scalars (on a fixed metric) [52, 108], and geons in pure gravity [49, 91].

While the nonperturbative physics of AdS instability requires numerical study, the perturbative formulation is purely analytical and encapsulates the weakly turbulent physics at  $\mathcal{O}(\epsilon^3)$  in a small-amplitude expansion. The linear-order system is simply a massless scalar in global AdS whose solution is written as a sum over the spatial eigenfunctions of AdS. At this order, the scalar field is stable for all times. The next-to-leading order in the expansion –  $\mathcal{O}(\epsilon^3)$  for the scalar field – gives an equation of motion for the scalar field that is sourced by the scalar’s backreaction with non-trivial metric functions. It is at this order that resonant sources terms arise which grow with time and invalidate the perturbative description. When only a single eigenmode is excited, resonances can be removed by frequency shifts; however, multimode data contain resonances that cannot be removed this way [91]. For fields constructed from multiple excited eigenmodes, the secular growth of resonant terms triggers the onset of instability [60, 91, 110, 127].

To describe the secular growth, the amplitude and phase of each eigenmode are allowed to flow with

respect to time. Applying renormalization techniques to these new slowly-varying amplitudes and phases leads to a ladder of coupled first-order ordinary differential equations describing the flow. There are several equivalent methods to arrive at the flow equations: the Two-Time Formalism (TTF) – wherein the slow time  $\tau = \epsilon^2 t$  is the flow parameter [44] – a renormalization-like formalism [42, 78], and time averaging procedure [78, 80]. The  $\mathcal{O}(\epsilon^3)$  resonances are then controlled by absorbing the secular terms into the renormalized amplitudes and phases.

In order to numerically solve the flow equations for a general scalar field, one naturally must truncate the mode expansion at a maximum eigenmode number  $j_{max}$ . By taking a quasi-periodic (QP) ansatz for the amplitude and phase variables, we are guaranteed a stable solution. These QP solutions, like all other solutions in the TTF description, have constant energy  $E$  and particle number  $N$ , and families of solutions are parameterized by a unit-less “temperature” parameter  $T = E/N$  [44, 82]. Understanding the bounds of the space of QP solutions allows us to better understand how to construct more general long-lived scalar fields. QP solutions are special in that the time-dependence of each mode is harmonic, so QP solutions satisfy algebraic equations. The first family of low-temperature solutions is found by directly solving these algebraic equations. High temperature solutions were purportedly found by [82] through repeatedly perturbing low-temperature solutions up to a maximum temperature of  $T_{max} = 2j_{max} + d$ .

In this work, we ask when QP solutions to the truncated TTF theory extend to the full untruncated theory. We explore the space of high temperature solutions using established perturbative methods, and solutions are tested against various choices of  $j_{max}$ . We then examine the stability of both classes of solutions through indicators such as the scalar curvature and energy transfer among eigenmodes.

This work is organized as follows: we begin in § 3.3 with a review of the linearized solutions for a minimally coupled, massless scalar field in  $\text{AdS}_{d+1}$ , as well as the renormalization flow equations that govern the time evolution of the amplitudes and phases in the TTF theory. In § 3.4, we find quasi-periodic solutions in  $\text{AdS}_4$  by numerically solving a set of algebraic equations and establish the bounds of low-temperature QP solutions. We then consider methods of probing the space of QP solutions to include high-temperature solutions in § 3.5, and examine the evolution of all QP

solutions within the perturbative theory in § 3.6. We end with a discussion of results in § 3.7.

### 3.3 Minimally Coupled Scalar Fields in AdS<sub>d+1</sub>

Consider a spherically-symmetric, asymptotically AdS<sub>d+1</sub> spacetime with characteristic curvature  $L = 1$ . Written in Schwarzschild-like coordinates, the metric is given by

$$ds^2 = \frac{1}{\cos^2(x)} (-Ae^{-2\delta}dt^2 + A^{-1}dx^2 + \sin^2(x)d\Omega^{d-1}), \quad (3.1)$$

where the radius  $x \in [0, \pi/2]$  and  $-\infty < t < \infty$ . A minimally-coupled, massless scalar field  $\phi(t, x)$  is subject to the following Einstein and Klein-Gordon equations:

$$G_{ab} + \Lambda g_{ab} = 8\pi \left( \nabla_a \phi \nabla_b \phi - \frac{1}{2} g_{ab} (\nabla \phi)^2 \right) \quad (3.2)$$

$$0 = \frac{1}{\sqrt{-g}} \partial_a \sqrt{-g} g^{ab} \partial_b \phi. \quad (3.3)$$

The canonical equations of motion for the scalar field are

$$\partial_t \phi = Ae^{-\delta}\Pi, \quad \partial_t \Phi = \partial_x(Ae^{-\delta}\Pi), \quad \text{and} \quad \partial_t \Pi = \frac{\partial_x(\Phi A e^{-\delta} \tan^{d-1}(x))}{\tan^{d-1}(x)}, \quad (3.4)$$

where the canonical momentum is  $\Pi(t, x) = A^{-1}e^\delta \phi$  and  $\Phi(t, x) \equiv \partial_x \phi$  is an auxiliary variable. In terms of these fields, (3.2) reduces to

$$\partial_x \delta = -(\Pi^2 + \Phi^2) \sin(x) \cos(x), \quad (3.5)$$

$$\partial_x A = \frac{d-2+2\sin^2(x)}{\sin(x) \cos(x)} (1-A) - A \sin(x) \cos(x) (\Pi^2 + \Phi^2). \quad (3.6)$$

### 3.3.1 Linearized Solutions

The linearized scalar field solutions come from expanding in terms of a small amplitude

$$\phi(t, x) = \sum_{j=0}^{\infty} \epsilon^{2j+1} \phi_{2j+1}(t, x), \quad A(t, x) = 1 - \sum_{j=1}^{\infty} \epsilon^{2j} A_{2j}(t, x), \quad \delta(t, x) = \sum_{j=1}^{\infty} \epsilon^{2j} \delta_{2j}(t, x). \quad (3.7)$$

Under this expansion, the  $\mathcal{O}(\epsilon)$  terms give the linearized equation of motion for the scalar field

$$\partial_t^2 \phi_1 + \hat{L} \phi_1 = 0 \quad \text{where} \quad \hat{L}_1 \equiv -\frac{1}{\tan^{d-1}(x)} \partial_x (\tan^{d-1}(x) \partial_x). \quad (3.8)$$

The eigenfunctions of  $\hat{L}$  satisfy  $\hat{L} e_j = \omega_j^2 e_j$ , where  $\omega_j = 2d + j$  and

$$e_j(x) = k_j \cos^d(x) P_j^{(\frac{d}{2}-1, \frac{d}{2})}(\cos(2x)) \quad \text{with} \quad k_j = \frac{2\sqrt{j!(j+d-1)!}}{\Gamma(j+\frac{d}{2})}. \quad (3.9)$$

Note that the normalizations are chosen such that

$$\langle e_i, e_j \rangle \equiv \int_0^{\frac{\pi}{2}} dx e_i e_j \tan^{d-1}(x) = \delta_{ij}. \quad (3.10)$$

By expanding the scalar field functions in terms of the eigenbasis given in (3.9) and substituting into (3.8), we find that the time-dependent functions  $c_n^{(2j+1)}(t) = \langle \phi_{2j+1}(t, x), e_n(x) \rangle$  satisfy  $\ddot{c}_j^{(1)} + \omega_j^2 c_j^{(1)} = 0$ . The general solution for the scalar field can then be written as a sum over eigenfunctions with time-independent amplitude and phase variables

$$\phi_1(t, x) = \sum_{j=0}^{\infty} A_j \cos(\omega_j t + B_j) e_j(x). \quad (3.11)$$

As discussed in [42, 78, 106], the integer nature of the mode frequencies mean that the spectrum is fully resonant. In general, secular growth caused by resonances cannot be absorbed by frequency shifts, and therefore result in *secular* terms: resonant contributions that grow rapidly with time and induce collapse. These resonant terms appear at  $\mathcal{O}(\epsilon^3)$  and can be expressed in terms of a source

$S(t)$  such that

$$\ddot{\phi}_3 + \hat{L}\phi_3 = S(t) \equiv 2(A_2 - \delta_2)\ddot{\phi}_1 + (\dot{A}_2 - \dot{\delta}_2)\dot{\phi}_1 + (A'_2 - \delta'_2)\phi'_1, \quad (3.12)$$

where  $A_2, \delta_2$  are the leading-order contributions to the metric functions in (3.7) that are determined by the  $\mathcal{O}(\epsilon^2)$  backreaction of the metric. Projecting onto the  $e_j(x)$  basis, the source term is

$$\ddot{c}_j^{(3)} + \omega_j^2 c_j^{(3)} = S_j. \quad (3.13)$$

To describe the growth of secular terms, [78] used renormalization techniques to absorb secular contributions into the  $\mathcal{O}(\epsilon^2)$  contributions to amplitudes and phases from (3.11). In particular, a set of renormalization flow equations were found that determined the time derivatives of the amplitudes and phases. As explained in [78], this procedure also allows for explicit expressions for the source term  $S_j$  to be calculated on resonance. These resonances occur for specific combinations of the frequencies found in  $S_j$ , such that the frequency of the  $\ell^{th}$  mode is equal to either  $\omega_i + \omega_j + \omega_k$ ,  $\omega_i - \omega_j - \omega_k$ , or  $\omega_i + \omega_j - \omega_k$ . After direct calculation of the source terms in each of these cases, [78] showed that the source terms naturally vanished for both the  $\omega_\ell = \omega_i + \omega_j + \omega_k$  and  $\omega_\ell = \omega_i - \omega_j - \omega_k$  channels. It was only for  $\omega_\ell = \omega_i + \omega_j - \omega_k$  that  $S(t) \neq 0$ .

### 3.3.2 Two-Time Formalism

The Two-Time Formalism (TTF) introduces a second time scale, the slow time  $\tau = \epsilon^2 t$ , that dictates the evolution of the amplitude and phase variables. In terms of  $\tau$ , the scalar field is

$$\phi(t, x) = \epsilon \sum_{j=0}^{\infty} A_j(\epsilon^2 t) \cos(\omega_j t + B_j(\epsilon^2 t)) e_j(x), \quad (3.14)$$

where  $A_j(\tau)$  and  $B_j(\tau)$  now contain both  $\mathcal{O}(1)$  and  $\mathcal{O}(\epsilon^2)$  contributions. In this description, the next non-trivial order in the equations of motion include gravitational self-interactions of the scalar field, and provides source terms for the time derivatives of  $A_j$  and  $B_j$ . Following the renormalization

procedure of [42] the derivatives of the  $\ell^{th}$  amplitudes and phases are given by

$$-\frac{2\omega_\ell}{\epsilon^2} \frac{dA_\ell}{dt} = \sum_{i \neq \ell} \sum_{j \neq \ell}^{\ell \leq i+j} S_{ij(i+j-\ell)\ell} A_i A_j A_{i+j-\ell} \sin(B_\ell + B_{i+j-\ell} - B_i - B_j), \quad (3.15)$$

$$\begin{aligned} -\frac{2\omega_\ell A_\ell}{\epsilon^2} \frac{dB_\ell}{dt} &= T_\ell A_\ell^3 + \sum_{i \neq \ell} R_{i\ell} A_i^2 A_\ell \\ &+ \sum_{i \neq \ell} \sum_{j \neq \ell}^{\ell \leq i+j} S_{ij(i+j-\ell)\ell} A_i A_j A_{i+j-\ell} \cos(B_\ell + B_{i+j-\ell} - B_i - B_j). \end{aligned} \quad (3.16)$$

*NB.* The remaining non-vanishing resonance condition allows us to write  $\omega_k = \omega_i + \omega_j - \omega_\ell$  above. The coefficients  $T_i, R_{ij}, S_{ijk}$  are calculated directly from integrals over the product of eigenmodes. Computationally, we find it more convenient to write these in terms of auxiliary coefficients with greater symmetry properties (as shown in [106]). The explicit expressions for these integrals in the interior gauge, in which  $\delta(t, x = 0) = 0$ , are given in appendix 3.B.

Using a complex amplitude of the form  $\mathcal{A}_j(\tau) = A_j \exp(-iB_j)$  in (3.14) allows us to combine equations (3.15) and (3.16) into a single equation

$$-2i\omega_\ell \frac{\mathcal{A}_\ell}{d\tau} = T_\ell |\mathcal{A}_\ell|^2 \mathcal{A}_\ell + \sum_{i \neq \ell} R_{i\ell} |\mathcal{A}_i|^2 \mathcal{A}_\ell + \sum_{i \neq \ell} \sum_{j \neq \ell}^{\ell \leq i+j} S_{ij(i+j-\ell)\ell} \mathcal{A}_i \mathcal{A}_j \bar{\mathcal{A}}_{i+j-\ell}, \quad (3.17)$$

where  $\bar{\mathcal{A}}$  denotes the complex conjugate. It was further demonstrated by [79] that the TTF theory resulted in a set of conserved quantities: the energy of the system,  $E$ , and particle number,  $N$ . The simultaneous conservation of both  $E$  and  $N$  imply the existence of inverse energy cascades that must balance direct cascades, thereby providing a mechanism through which two-mode data could remain stable.

## 3.4 Quasi-periodic Solutions in AdS<sub>4</sub>

The stability of the solutions to (3.17) can be examined using a *quasi-periodic* (QP) ansatz for the complex amplitude

$$\mathcal{A}_j = \alpha_j e^{i\beta_j \tau}, \quad (3.18)$$

where  $\alpha_j, \beta_j \in \mathbb{R}$ . Substituting (3.18) into (3.14) allows us to relate the QP modes  $\alpha_j$  and  $\beta_j$  to the amplitude/phase modes via  $A_j = 2\alpha_j$ ,  $B_j = \beta_j \tau$ . The time dependence in (3.17) is removed via the condition  $\beta_j = \beta_0 + j(\beta_1 - \beta_0)$ , leaving  $\beta_0$  and  $\beta_1$  as unknown parameters. Considering modes of (3.14) up to some  $j_{max}$ , the QP ansatz results in a set of  $j_{max} + 1$  algebraic equations for  $j_{max} + 3$  unknowns

$$2\omega_\ell \alpha_\ell \beta_\ell = T_\ell \alpha_\ell^3 + \sum_{i \neq \ell} R_{i\ell} \alpha_i^2 \alpha_\ell + \sum_{i \neq \ell} \sum_{j \neq \ell}^{\ell \leq i+j} S_{ij(i+j-\ell)\ell} \alpha_i \alpha_j \alpha_{i+j-\ell}. \quad (3.19)$$

As shown in [80, 82], the TTF is invariant under two  $U(1)$  transformations which lead to the conserved quantities

$$E = 4 \sum_j \omega_j^2 \alpha_j^2 \quad \text{and} \quad N = 4 \sum_j \omega_j \alpha_j^2. \quad (3.20)$$

These definitions allow for two of the free parameters to be fixed. Families of solutions can be examined by fixing  $\alpha_0 = 1$  and sampling a range of  $\alpha_1$  values in the range  $\alpha_1 \ll \alpha_0$ . The families of solutions can be distinguished by their “temperature”, or energy per particle number  $T = E/N$ .

Practically speaking, finding solutions to the  $j_{max}$  equations that arise from (3.17) requires truncating the series at a finite value  $j_{max} < \infty$ . Then, one of the free parameters (either  $\alpha_1$  or  $T$ ) is set and used to generate seed values so that (3.17) can be solved using a Newton-Raphson solver (see appendix 3.A for more details). Within a space spanned by  $\{\alpha_1, \dots, \alpha_{j_{max}}\}$  we can imagine a surface that represents all possible QP solutions. For a set of seed values, solving (3.19) with fixed  $\alpha_1$  ( $T$ )

is tantamount to moving along lines of constant  $\alpha_1$  ( $T$ ) until the solution surface is intersected<sup>7</sup>. For this reason, we refer to solving the QP equation (3.19) given seed values for  $[\alpha_2, \dots, \alpha_{j_{max}}]$  and one fixed value as *projecting back* to the solution surface.

### 3.4.1 Persistence at Large $j_{max}$

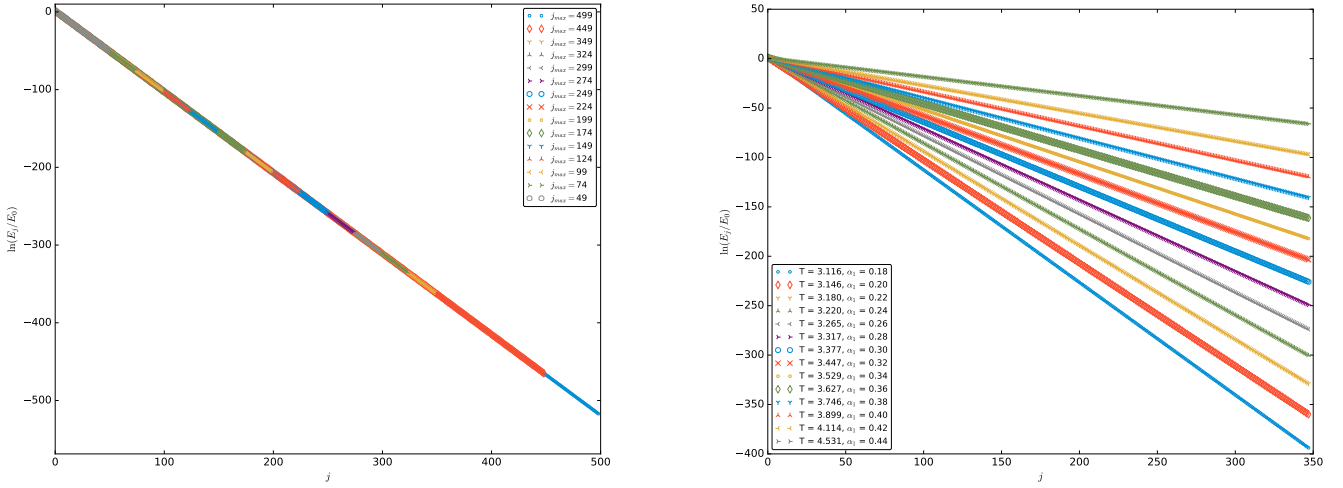
The question of edge effects in determining the robustness of a particular solution is important to investigate. For instance, if a particular solution to (3.19) is found for some  $\alpha_1$  when  $j_{max} = 50$ , does this continue to be a solution when we consider more modes, say  $j_{max} = 250$ ? By following the methods outlined in appendix 3.A, we are able to start with a low  $j_{max}$  solution and incrementally increase the number of modes being considered up to several hundred. This method was found to be more successful, given the optimization algorithms being used, than other seeding methods.

As an example, consider solutions to (3.19) with the conditions  $\alpha_0 = 1.0$  (since all QP solutions are defined up to an overall scale,  $\alpha_0 = 1.0$  is taken to always be true) and  $\alpha_1 = 0.2$ , which corresponds to a temperature of  $T \simeq 3.146$ . In figure 3.1a, we present an overlay of QP solutions generated by successive solving, fitting, and seeding from  $j_{max} = 50$  to  $j_{max} = 500$  for a family of QP solutions. Similar high  $j_{max}$  solutions were confirmed for  $\alpha_1 \leq 0.442$  and are shown in figure 3.1b.

When examining the range of  $\alpha_1$  values that yield low temperature QP solutions, it was found that any small  $j_{max}$  QP solution could be extended to large  $j_{max}$  with proper seeding and sufficient computing power; that is, there seem to be no solutions that exist at low  $j_{max}$  that cease to exist at high  $j_{max}$ . However, a hard limit exists at the maximum  $\alpha_1$  value of  $\alpha_1 = 0.442$ , corresponding to a temperature of  $T \simeq 4.643$ . Above this limit, no QP solutions can be found by directly solving (3.19), even with  $j_{max}$  values as low as  $j_{max} = 50$ . Conversely, there is no lower limit to  $\alpha_1$  values; as  $\alpha_1 \rightarrow 0$  with  $\alpha_j > \alpha_{j+1}$ , the TTF solution approaches the well-known single-mode solution.

---

<sup>7</sup>For low temperatures, the same QP solution is found whether travelling along lines of constant  $\alpha_1$  or  $T$ . For higher temperatures, however, this picture becomes more complicated.



(a) An overlay of QP solutions with  $\alpha_1 = 0.2$ , corresponding to  $T \simeq 3.146$ , for increasing values of  $j_{max}$ .

(b) QP solutions with  $j_{max} = 350$  spanning temperatures of  $3.116 \lesssim T \lesssim 4.531$ .

**Figure 3.1:** Energy spectra for various low temperature QP solutions.

### 3.5 High Temperature Perturbations

In [82], additional QP solutions were found by repeatedly perturbing away from existing solutions: the addition of some energy  $\delta E$  corresponds to the changes  $\alpha_j \rightarrow \alpha_j + u_j$  and  $\beta_j \rightarrow \beta_j + \theta_1 + \omega_j \theta_2$ . The perturbed quantities are given by the system of linear equations

$$\delta E = 4 \sum_j \omega_j^2 \alpha_j u_j \quad (3.21)$$

$$\delta N = 4 \sum_j \omega_j \alpha_j u_j = 0 \quad (3.22)$$

$$\begin{aligned} 0 = \omega_\ell (\alpha_\ell (\theta_1 + \omega_\ell \theta_2) + \beta_\ell u_\ell) + 6T_\ell \alpha_\ell^2 u_\ell + 2 \sum_{i \neq \ell} R_{i\ell} (\alpha_i^2 u_\ell + 2\alpha_i \alpha_\ell u_\ell) \\ + 2 \sum_{i \neq \ell} \sum_{j \neq \ell}^{\ell \leq i+j} S_{ij(i+j-\ell)\ell} [u_i \alpha_j \alpha_{i+j-\ell} + u_j \alpha_i \alpha_{i+j-\ell} + \alpha_i \alpha_j u_{i+j-\ell}]. \end{aligned} \quad (3.23)$$

Therefore, by solving (3.21)-(3.23) for  $\{u_j, \theta_1, \theta_2\}$ , the existing QP solution can be updated and the process can be repeated.

For a standard QP solution with  $\alpha_1 = 0.2$ , the initial temperature is  $T \simeq 3.146$ . By applying the

high temperature perturbation method described above, we are able to increase the temperature of the solution. However, this process must be examined with some scrutiny; applying repeated perturbations to a known solution does not guarantee the final result remains a valid solution. To investigate this further, we have implemented two high temperature solvers, both of which increment the energy of the system using (3.21)-(3.23) and are able to use the updated values of  $\alpha_j$  and  $\beta_j$  as seeds to solve (3.19) using a Newton-Raphson solver.

The projection used by the first solver follows the form used in [82] and takes an input  $\alpha_1$  value when projecting to the QP solution surface, while the second holds the temperature of the solution fixed during projection. To hold the temperature fixed, we use the definition of  $T$  and the freedom to rescale the  $\alpha_j$  such that  $\alpha_0 = 1$  to solve for  $\alpha_1$  via

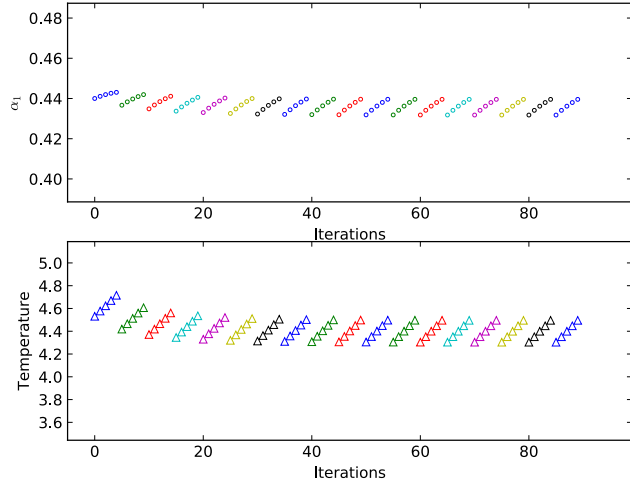
$$\alpha_1^2 = \frac{1}{\omega_1(T - \omega_1)} \left( \omega_0(\omega_0 - T) + \sum_{j \geq 2} \omega_j(\omega_j - T)\alpha_j^2 \right) \quad (3.24)$$

It can easily be seen that  $\alpha_1$  will become singular when  $T = \omega_1 = 5$  in AdS<sub>4</sub>. Since we are inputting a value for the temperature  $T$  instead of a  $\alpha_1$ , we are still solving a system of  $j_{max} + 1$  equations for  $j_{max} + 1$  unknowns.

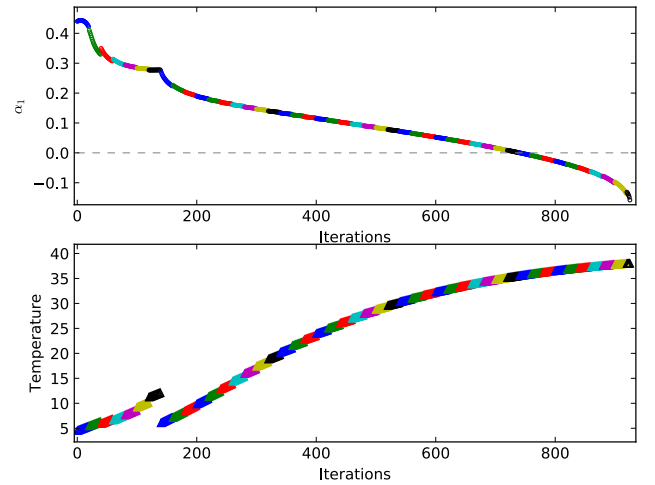
### 3.5.1 Projections at Constant $\alpha_1$

Let us first consider the results of the  $\alpha_1$  projection method, shown in figure 3.2. We have fixed the perturbation amount  $\delta E$  to 1% of the energy of the initial solution. Beginning with an  $\alpha_1 = 0.44$  solution with low  $j_{max}$ , we apply repeated energy perturbations and project back to the QP solution surface with a frequency of once per 5 temperature iterations (see appendix 3.C for further discussion on projection frequency and energy perturbation value). Figure 3.2a shows the resulting values of  $\alpha_1$  and  $T$  during these perturbations. We see that  $\alpha_1$  approaches an attractor solution of  $\alpha_1 \simeq 0.43$  with  $T \simeq 4.3$ . The energy perturbations between projections are insufficient to escape this local minimum, thus repeated projections return the same solution. However, when the projection frequency is decreased to once every 20 iterations, the resulting QP solution is able to bypass the

attractor solution (variations of the projection frequency and energy perturbations are discussed in appendix 3.C). Note that as the iteration number increases, we actually see a *decrease* in  $\alpha_1$  value while the temperature continues to increase. At iteration 150 in figure 3.2b, there is a cusp in  $\alpha_1$  and a discontinuity in the temperature. After several hundred iterations,  $\alpha_1$  becomes negative.



(a) Applying repeated energy perturbations to an initial QP solution with  $\alpha_1 = 0.44$ , then projecting back to the QP surface every five iterations.



(b) Beginning with the same  $\alpha_1 = 0.44$  QP solution, the same process of energy perturbations are applied, this time projecting back to the QP surface every 20 iterations.

**Figure 3.2:** The results of projecting a  $j_{max} = 50$ ,  $\alpha_1 = 0.44$  solution back to the QP surface at various frequencies during high temperature perturbations. Colour changes indicate that the solution has been projected back to the QP surface.

Let us examine the energy spectra of these solutions. In figure 3.3a we see that when we choose a high projection frequency, the resulting energy spectra do not deviate far from the initial solution (using the  $\alpha_1$  projection method) in either shape or temperature, but rather approach an attractor solution. The temperature of this attractor solution is robust against increases in  $j_{max}$ , as shown in table 3.1.

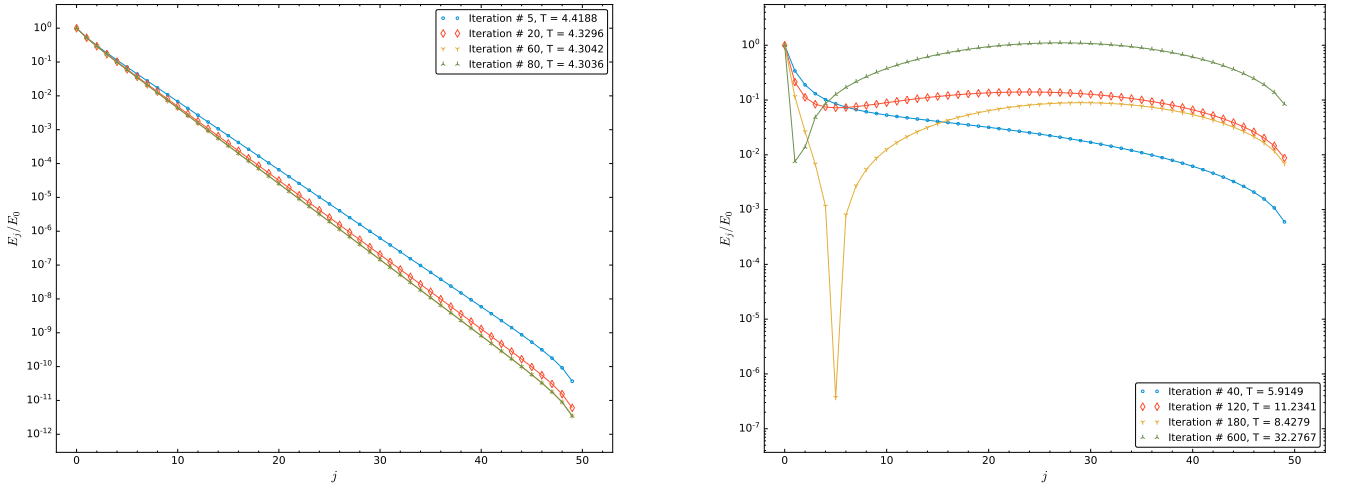
When the projection frequency is decreased, the solution is able to pass the attractor in temperature. However, as seen in figure 3.3b, projections back to the QP surface give  $\alpha_1 < 0$  and an energy spectrum that is no longer a smooth<sup>8</sup> function of  $j$  (*c.f.* spectra of iterations 120 and 180). This in itself is not necessarily a breakdown of the quasi-periodic nature of the solution. However, upon

<sup>8</sup>Here we appeal to the colloquial meaning of “smooth” instead of a strictly mathematical meaning, since  $E_j$  is a function of a discrete variable.

$j_{max}$	$T$	Iterations
50	4.30344575697724e+00	350
75	4.30344544264076e+00	210
100	4.30344544023857e+00	540
150	4.30344544024198e+00	280
200	4.30344544023915e+00	300

**Table 3.1:** The temperature of the attractor solution for various  $j_{max}$  values. Also included is the number of iterations applied (projecting back to the solution surface with constant  $\alpha_1$  after every five iterations).

examining the condition number of the matrix formed by (3.21)-(3.23), we find that in fact the problem becomes ill-conditioned. This results in an absolute value of  $u_i$  that is greater than  $\alpha_i$ ; that is, the perturbative condition required to derive the system of linear equations (3.21)-(3.23) breaks down. For many prospective high-temperature solutions, this break-down of the perturbative condition is signalled by the loss of a smooth energy spectrum due to the values of  $\alpha_j$  becoming negative.



**(a)** Energy spectra when projecting back to the QP solution surface every 5 iterations for an initial  $\alpha_1 = 0.44$ , QP solution (see figure 3.2a for temperature and  $\alpha_1$  as a function of iteration).

**(b)** The same initial QP solution as figure 3.3a is used, but is projected back to the QP surface every 20 iterations.

**Figure 3.3:** Comparing energy spectra of high-temperature perturbations of an  $\alpha_1 = 0.44$  QP solution that have been projected back to the QP surface at different frequencies.

### 3.5.2 Projections at Constant Temperature

We again use a series of small energy perturbations to seek high-temperature QP solutions, this time using a constant-temperature projection method at regular intervals. Starting from a standard  $\alpha_1 = 0.44$  QP solution, we apply successive perturbations to increase the temperature. After five increments, the temperature is calculated and used as the input to the second nonlinear solver. This ensures that the temperature is not changed when projecting back to the QP solution surface. The seed values were projected back to the QP solution surface when goal temperatures of  $T = 5.5, 6.0,$  and  $7.0$  were reached (or at the first perturbation when these temperatures were exceeded). The resulting spectra for each temperature goal over several choices of  $j_{max}$  are shown in figure 3.4. It is worth noting that we did not include the spectra for  $j_{max} = 250$  solutions with goal temperatures of  $T = 6.0$  and  $7.0$  because the fixed-temperature projection failed to find a solution.

Recall that solutions must be robust in the limit of  $j_{max} \rightarrow \infty$  in order to be considered solutions to the full TTF theory. While the upper panel of figure 3.4 suggests that solutions with temperatures at or near  $T = 5.5$  can be constructed in the large- $j_{max}$  limit, we do not find evidence that low  $j_{max}$  solutions with  $T = 6.0, 7.0$  extend to the full theory.

### 3.5.3 Building High-Temperature Solutions

In figure 3.4 we see that QP solutions with smooth spectra exist for goal temperatures of  $T = 6.0$  and  $7.0$  when  $j_{max} = 50$  but cease being smooth as  $j_{max}$  increases and the temperature is held constant. It is therefore reasonable to ask whether high temperature, low  $j_{max}$  QP solutions can be extended to higher  $j_{max}$  by using a fitting procedure to generate seed values for the fixed- $\alpha_1$  Newton-Raphson solver. In figure 3.5, instead of fitting  $\alpha_j$  values for modes  $[j_{max} - 30, j_{max} - 10]$  (as outlined in appendix 3.A), we have applied the fitting method to final 5 modes and used the result to generate seed values for a solution with  $j_{max} + 5$  modes. This method was successful in finding QP solutions with substantially higher temperatures than the previous seeding method.

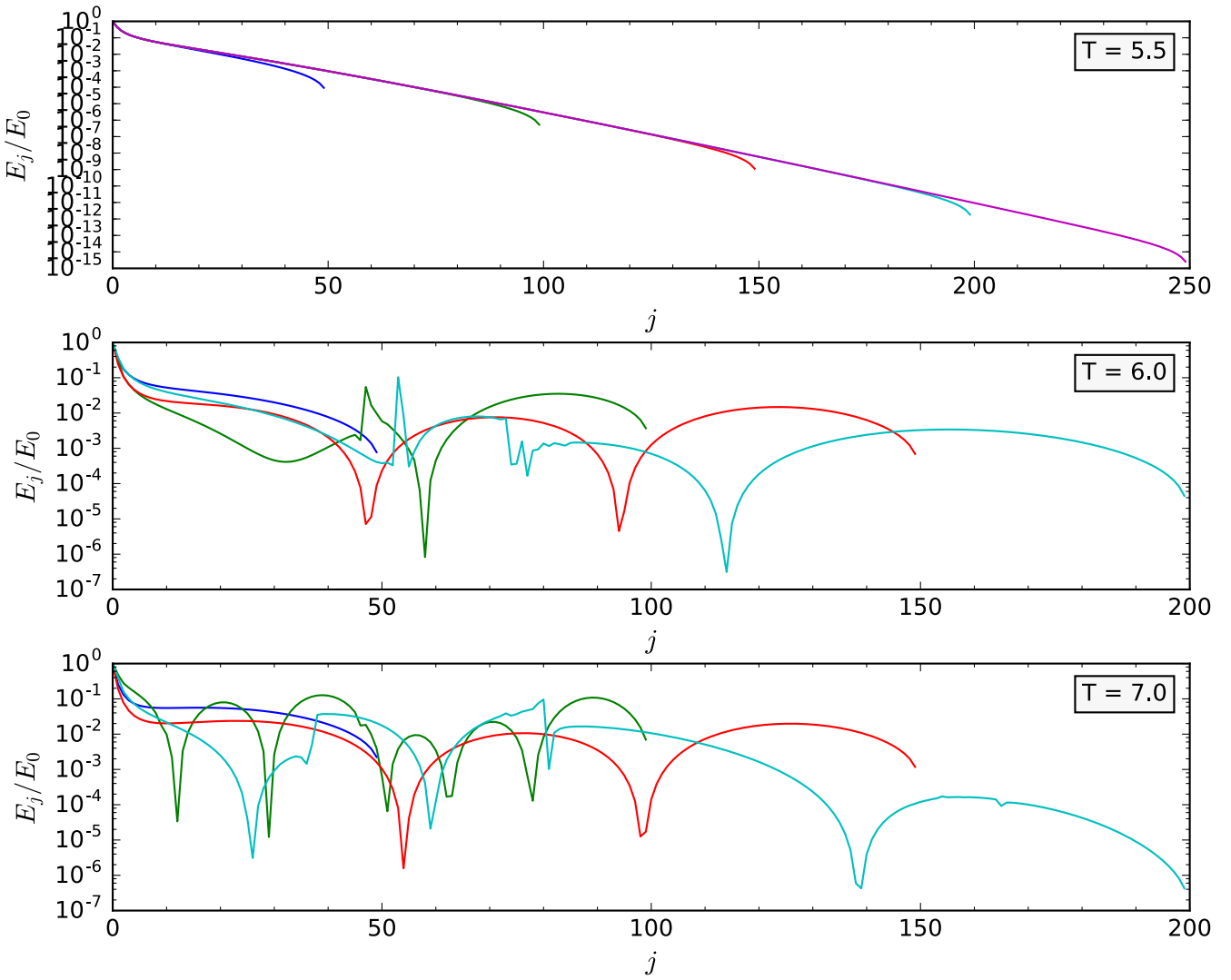


**Figure 3.4:** For each panel, a goal temperature (top right of plot) is set. Beginning with  $\alpha_1 = 0.44$  QP solutions with  $j_{max} = 50, 100, 150, 200, 250$  repeated energy perturbations are applied. After five energy perturbations, the data is projected back to the QP surface at constant  $T$ . When the goal temperature is either reached or exceeded for the first time, the data is again projected back at constant temperature.

However, the solutions were not robust with the addition of extra modes. Instead, the distribution of energy in the resulting spectra becomes increasingly concentrated in high- $j$  modes with the addition of as few as five extra modes. As we see in figure 3.5, fitting the tail of the  $j_{max} = 75$ ,  $T \simeq 27$  and producing seed values for a  $j_{max} = 80$  solution resulted in a QP solution with  $T \simeq 38$  after projecting back to the QP surface with constant  $\alpha_1$ . Because these solutions were not robust as  $j_{max}$  was increased, they do not provide evidence of solutions to the untruncated theory at those temperatures.

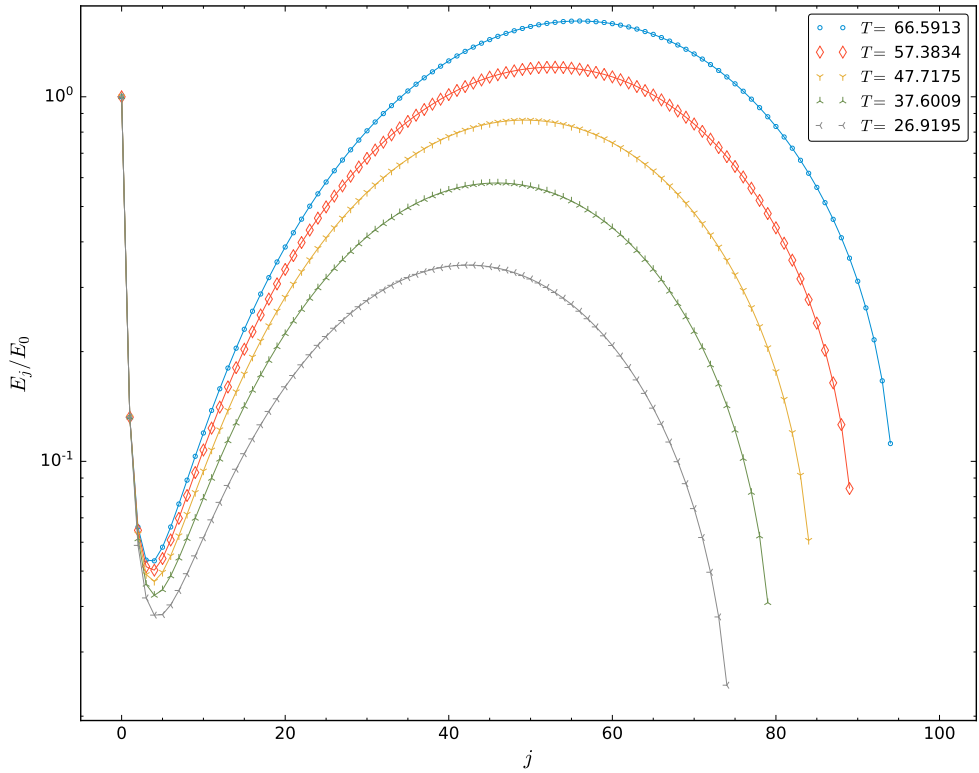


**Figure 3.5:** Beginning with the  $j_{max} = 75$ ,  $T \simeq 27$  solution (grey left-tri), a fit is applied to the final five modes to generate seed values that are used in the fixed- $\alpha_1$  Newton-Raphson solver find the next QP solution. The procedure is repeated to generate the  $j_{max} = 80$ ,  $T \simeq 38$  (green up-tri),  $j_{max} = 85$ ,  $T \simeq 48$  (yellow down-tri),  $j_{max} = 90$ ,  $T \simeq 57$  (red diamonds), and  $j_{max} = 95$ ,  $T \simeq 67$  (blue circles) QP spectra.

In [82], it was suggested that QP solutions should exist in a continuous region of temperature space  $T \in [T_{min}, T_{max}] = [d, 2j_{max} + d]$ . To produce high-temperature solutions, successive energy perturbations could be applied to a low-temperature solution with a low frequency of projecting back to the QP surface. However, we have found that the high temperature solutions produced using regular projections back to the solution surface are not robust as  $j_{max}$  increases and therefore do no

constitute physical solutions. In further pursuit of high temperature QP solutions, we investigated additional methods for generating these solutions.

First, we considered applying a similar fitting technique to a  $T \simeq 5.4$  QP solution as that which was used to extend low-temperature QP solutions. In this case, values were taken from the middle<sup>9</sup> of high temperature solutions with  $j_{max} = 50$  and fit with an exponential function (see figure 3.A.2 for a similar procedure with tail values) to produce 10 new modes,  $\{\alpha_{fit}\}$ . We then inserted the new values  $\alpha_{fit}$  with the existing data so that  $\alpha_j = \langle \alpha_{j < j_{mid}}, \alpha_{fit}, \alpha_{j > j_{mid}} \rangle$ . The result was to extend the data by 10 modes and slightly increase the temperature, thereby providing a good seed for the constant-temperature nonlinear solver. However, no solutions were found by the Newton-Raphson solver, starting either with  $j_{max} = 50$ ,  $T > 5.5$  data, or  $j_{max} = 200$ ,  $T \simeq 5.5$  data.

Next, we considered perturbing up to an intermediate temperature  $5.5 \ll T_{int} < T_{max}$  before attempting to project back to the QP surface using the  $T_{int}$  data as seed values. In particular, we repeatedly perturbed a  $T \simeq 4.5$  solution using the method described in § 3.5 to a temperature of  $T_{int} = 20$  without projecting back to the QP surface *at any point*. For  $j_{max} \lesssim 100$ , projection back to the solution surface finds a new solution with  $T < T_{int}$  that – much like the spectra shown in figure 3.3b – loses its smooth profile. Under evolution within the TTF theory (discussed below), the fractional energy in the low-frequency modes oscillates rapidly over several orders of magnitude during the evolution and the Ricci scalar reaches values  $\mathcal{O}(10^6)$ ; these solutions are almost certainly not quasi-periodic. The same result is found for high-temperature solutions created by fitting tail data (see figure 3.5 for example spectra). Finally, for  $j_{max} \geq 100$ , projection back to the QP solution surface once  $T = T_{int}$  fails entirely. Thus, we did not find evidence for QP solutions with temperatures above  $T \simeq 5.5$ .

---

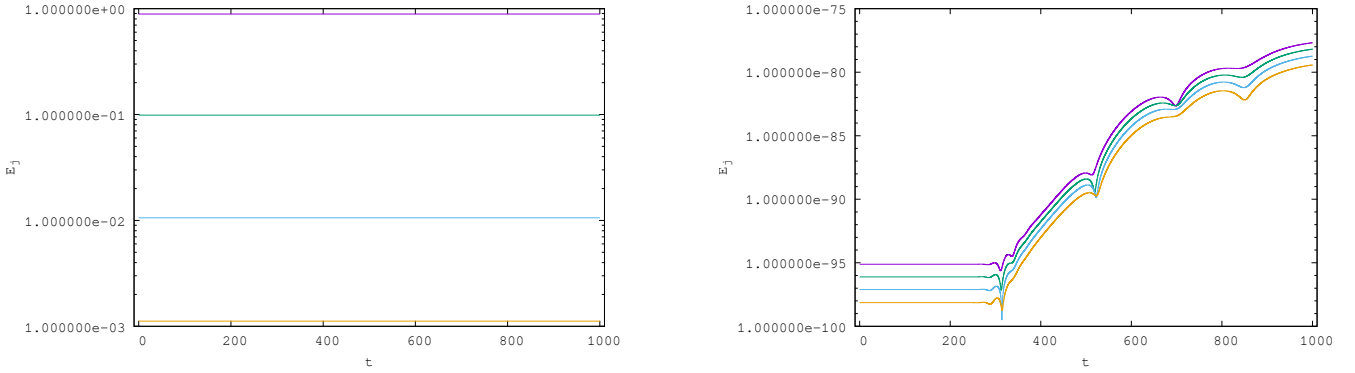
<sup>9</sup>Typically at  $j_{max}/2$ , where the power law scaling has not been affected by edge effects.

## 3.6 Time Evolution of Quasi-Periodic Solutions

The weakly turbulent behaviour of the scalar field in the TTF is captured by the  $\mathcal{O}(\epsilon^2)$  renormalization group flow equations (3.15)-(3.16). Having identified different families of quasi-periodic solutions, we wish to evolve these solutions within the TTF description. Furthermore, we may also be able to identify previously inaccessible solutions by evolving a QP solution within the TTF framework before attempting to project back to the QP surface. To achieve these aims, we use numerical methods first described by [111] and take both low-temperature and high-temperature QP solutions as initial data.

### 3.6.1 Low-temperature QP data

Let us consider the evolution of a “typical” QP solution: a solution to (3.19) with  $\alpha_1 = 0.2$  and  $j_{max} = 100$ , corresponding to a temperature of  $T \simeq 3.146$ . Choosing an amplitude of  $\epsilon = 0.01$  (note that the TTF equations are invariant under  $\mathcal{A}(\tau) \rightarrow \epsilon \mathcal{A}(\tau/\epsilon^2)$  and so the value of  $\epsilon$  does not change the physics), figure 3.6 shows the evolution of the fraction of the total energy per mode. We see that energy in the lowest- $j$  modes remains constant over the duration of the evolution, while the fraction in the highest- $j$  modes increases after  $t \simeq 300$ . Similar behaviour is observed for higher  $j_{max}$  solutions and over values of  $0.2 \leq \alpha_1 \leq 0.44$ . Given the scale of the energy in the modes  $j \geq 96$ , the growing energy fractions in these modes can mainly be attributed to numerical errors rather than direct energy cascades.



(a) From top to bottom:  $j = 0, 1, 2, 3$  (purple, green, blue, orange).

(b) From top to bottom:  $j = 96, 97, 98, 99$  (purple, green, blue, orange).

**Figure 3.6:** Fraction of the total energy in each mode during evolution of an  $\alpha_1 = 0.2$ ,  $j_{max} = 100$ , QP solution with  $\epsilon = 0.01$ .

We may also ask: does a given quasi-periodic solution remain unique under evolution? That is, will the solution project back to itself during its evolution? To answer this, we evolve the same low-temperature, QP solution and take the spectra at different times as seed values for projecting back to the QP surface. We see that seed values taken from data with  $t > 0$  are projected back to themselves (using the constant  $\alpha_1$  Newton-Raphson method) at all times during the evolution, and that the resulting solutions solve the QP equation (3.19) to a high degree of accuracy (see figure 3.7).

In an effort to find new QP solutions, we consider an alternative method for finding solutions that may not be accessible through established seeding methods. We pad a given quasi-periodic solution with extra modes that are initially set to zero and project back to the QP solution surface. Upon amplitude-phase evolution via (3.15)-(3.16), the energy in the lower- $j$  modes will flow into the higher- $j$  modes. This may lead to new quasi-periodic solution with the same temperature but larger  $j_{max}$ . In figure 3.8, we construct initial data from a known  $j_{max} = 100$ ,  $T \simeq 3.14$  solution by padding the data with zeros up to  $j_{max} = 200$ . As in the case of unpadded QP solution, the fraction of the total energy in the first four modes does not vary significantly during the evolution and the highest modes accumulate some numerical error before levelling off. Despite the somewhat normal profile of the spectra of padded QP solution (shown in figure 3.8c) and the relatively low value of the Ricci scalar (see figure 3.8d), we find that the Newton-Raphson solver – both constant- $\alpha_1$

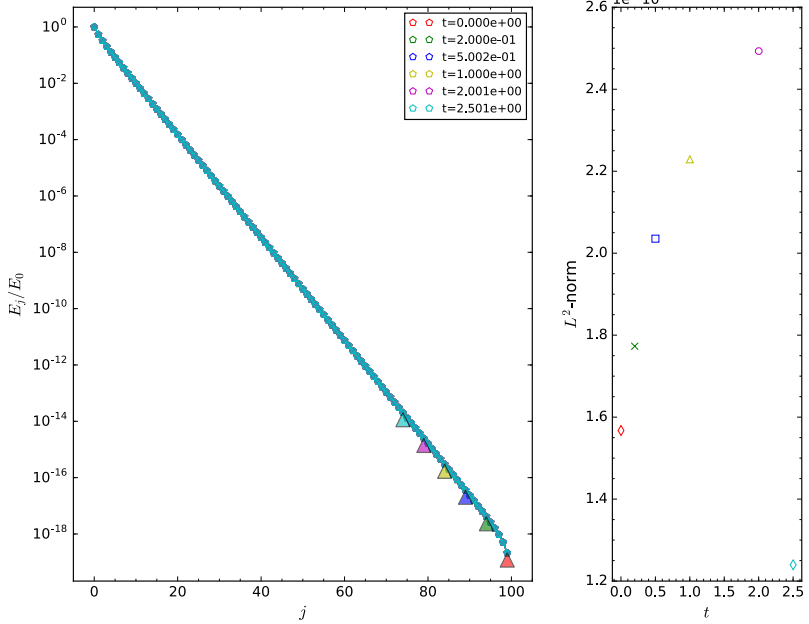
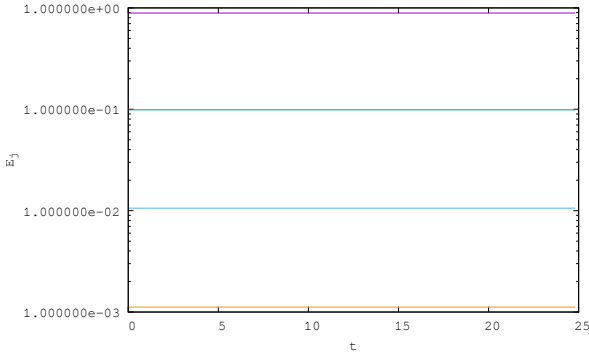


**Figure 3.7:** *Left:* Projecting a low-temperature solution back to the QP surface with constant  $\alpha_1$  during its evolution. Arrows are oriented from amplitude/phase seed values (circles) to QP surface projections (pentagons). *Right:* the  $L^2$ -norms of the errors between solutions at  $t \simeq 0.0, 0.2, 0.5, 1.0, 2.0, 2.5$  (red diamond, green cross, blue square, yellow triangle, magenta circle, blue diamond).

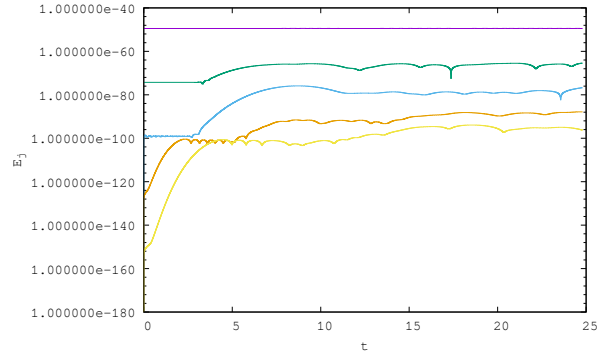
and constant- $T$  – is not able to project back to the QP surface when the evolved QP solution is used as seed data. To check whether the failure to project back to the QP surface is due to the addition of too many extra modes, we also investigated incrementally adding a small number of modes. Beginning with the same  $j_{max} = 100$  QP solution, we padded with only five modes. Despite a QP solution with  $j_{max} = 105$  already being known, the evolution did not result in the padded solution approaching the known solution.

### 3.6.2 High-Temperature QP Data

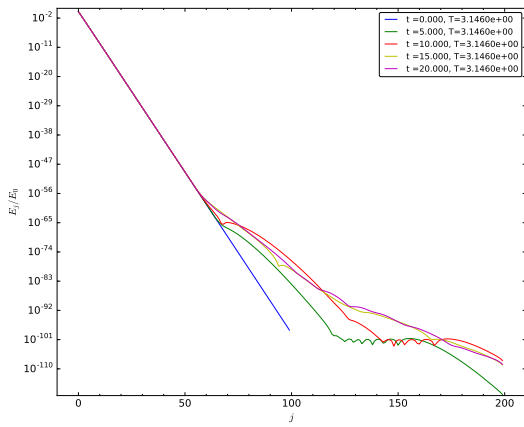
We now apply the same amplitude-phase evolution procedure to higher temperature QP data. First, we consider a QP solution with  $j_{max} = 100$  and  $T \simeq 5.4$ . Such a solution was demonstrated in figure 3.4 to be robust as  $j_{max}$  increased. In figure 3.9 we show the fractional energy per mode during evolution. Because of the initial profile of solutions with these temperatures, there is a much higher fraction of the total energy in the higher modes; therefore, the accumulation of numerical



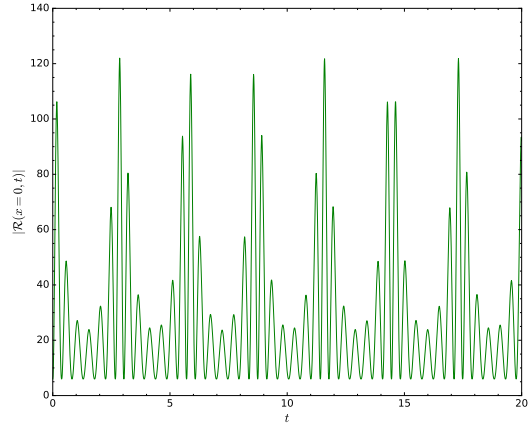
(a) The evolution of the first four modes of the padded QP solution:  $j = 0, 1, 2, 3$  (purple, green, blue, orange).



(b) Comparing the evolution of a selection of modes:  $j = 50, 75, 100, 125, 150$  (purple, green, blue, orange, yellow).



(c) The total spectrum of the padded QP solution as a function of time.



(d) The Ricci scalar at the origin as a function of time.

**Figure 3.8:** The evolution of the padded QP solution for  $\alpha_1 = 0.2$  and  $j_{max} = 200$ , with amplitude  $\epsilon = 0.27$  over  $t \in [0, 25]$ .

errors that were present in low-temperature solutions are not as significant. Close inspection of figure 3.9, shows small oscillations in the fractional energy of the high frequency components of the scalar field. However, these oscillations are not sufficient to produce a qualitative change in the full energy spectrum, as shown in the left pane of figure 3.10. Examination of the absolute value of the scalar curvature at the origin in the right pane of figure 3.10 shows that the large initial value of  $|\mathcal{R}|$  oscillates rapidly during evolution. Since the TTF description is inherently stable, the curvature will never become infinite; however, large values of curvature with rapid oscillations are good indicators of instability. It would be interesting to use such a solution as initial data for evolution in the fully nonlinear system to test if stability is maintained over the perturbative timescale.

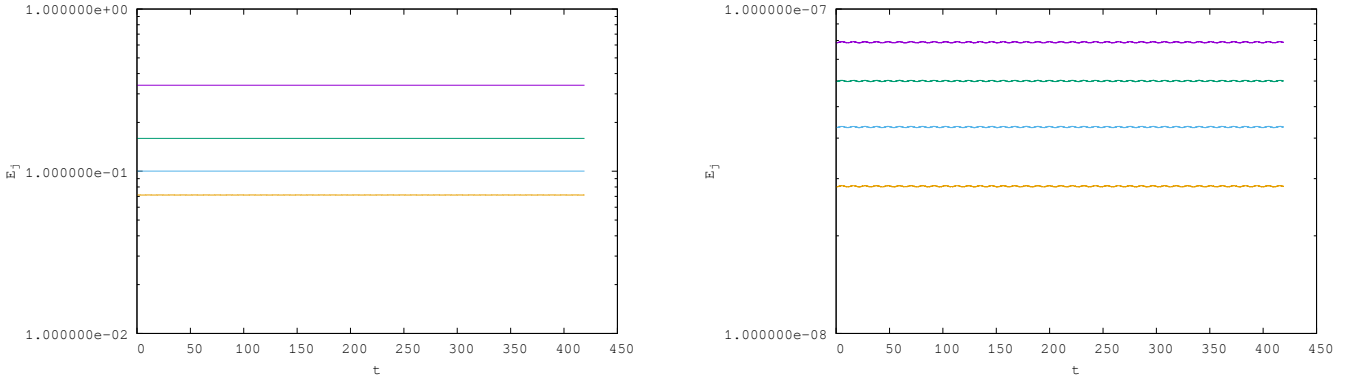


**Figure 3.9:** Examining the energy per mode during the evolution of a  $T \simeq 5.4$  QP solution with  $\epsilon = 0.1$  over  $t \in [0, 425]$ .  $E_j$  for  $j = 0, 1, 2, 3$  (purple, green, blue, orange) is on the left,  $E_j$  for  $j = 96, 97, 98, 99$  (purple, green, blue, orange) is on the right.

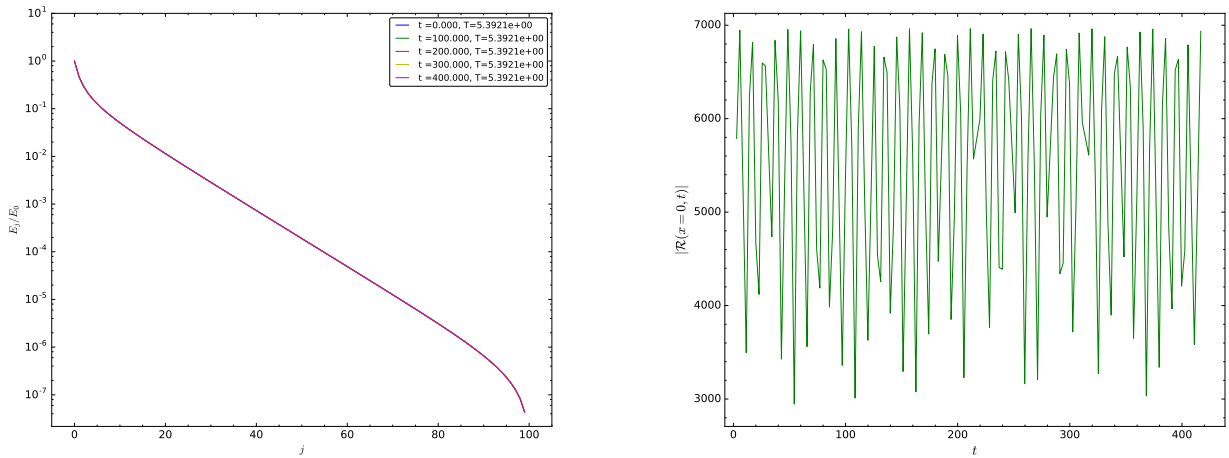


**Figure 3.10:** The evolution of the energy spectrum (left) and upper envelope of the Ricci scalar (right) for a  $T \simeq 5.4$  QP solution with  $\epsilon = 0.1$  over  $t \in [0, 425]$ .

As in the case of low-temperature QP solutions, we wish to expand the space of possible solutions by padding high temperature solutions with extra modes that are initially set to zero. To do so, we consider padding a  $T \simeq 5.4$  QP solution from  $j_{max} = 100$  to  $j_{max} = 200$  with  $\alpha_j = 0$  for  $j > 99$ . Figure 3.11 demonstrates that after evolving in time there are indications of large scale energy transfer amongst modes with higher frequencies. Interestingly, the magnitude and oscillation frequency of the Ricci scalar at the origin is significantly decreased compared to the

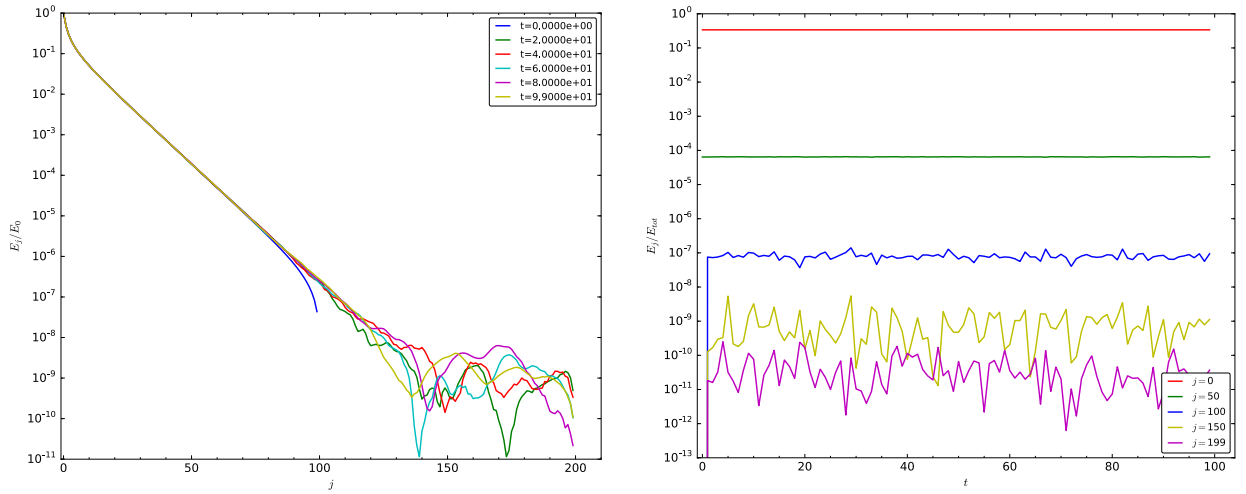


**Figure 3.11:** A  $T \simeq 5.4$  QP solution shown in figure 3.10 is padded with 100 extra modes and evolved with  $\epsilon = 0.1$  over  $t \in [0, 100]$

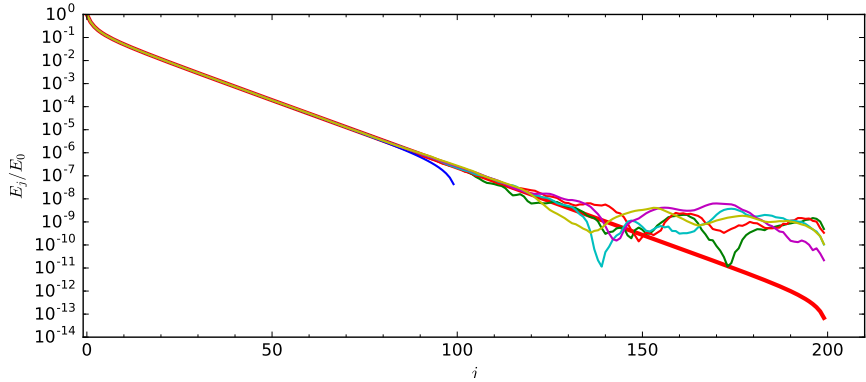


**Figure 3.12:** Overlay of the known  $T \simeq 5.4$  solution for  $j_{max} = 200$  (thick red line) with the spectra in figure 3.11.

$j_{max} = 100$ ,  $T \simeq 5.4$  solution. When compared against the known solution of the same temperature when  $j_{max} = 200$ , figure 3.12 indicates that the padded solution may not approach the known QP solution and instead may have produced a distinct, isothermal, but non quasi-periodic, solution.

## 3.7 Discussion

We have explored the space of quasi-periodic solutions within the perturbative description of a massless scalar field in  $\text{AdS}_4$ . Using the conserved quantities  $E$  and  $N$ , we constructed families of quasi-periodic solutions that were distinguished by the temperature  $T = E/N$  for different choices

of the truncation value  $j_{max}$ . We have demonstrated that low temperature QP solutions, i.e. those that are clearly accessible by solving (3.19) for a given  $\alpha_1$  such that  $\alpha_1 < \alpha_0 = 1$ , can be extended to arbitrarily large  $j_{max}$  values, and therefore constitute solutions to the TTF theory. We have also examined high temperature QP solutions, which are found by perturbing low temperature solutions by  $\delta E$  while keeping  $N$  fixed. We found that a high temperature solutions were robust against increasing  $j_{max}$  only for temperatures  $T \lesssim 5.5$ . We also applied several alternative methods for generating high temperature QP solutions. However, we were not able to find evidence of any solutions that could be extended to the untruncated TTF system. We constructed low- $j_{max}$  solutions with  $T \gg 5.5$ , but found that they were not robust with increasing  $j_{max}$  and therefore were not true solutions. Rather, only solutions with temperatures  $T \lesssim 5.5$  could be extended to large  $j_{max}$  values. The nature of this temperature threshold is not totally understood. It may be due to numerical limitations with the Newton-Raphson solving method, or it may be a physical limitation of the quasi-periodic ansatz.

By construction, TTF solutions are stable against gravitational collapse and therefore evolution within the TTF description will not produce a singularity. However, there are several indicators for instability in the fully nonlinear theory: the value of the Ricci scalar at the origin, the growth higher-order contributions to the lapse function  $\delta$ , and rapid growth/oscillations in the energy of high frequency modes. With these indicators in mind, we have shown that low temperature QP solutions constructed from directly solving (3.19) did produce oscillations in  $\mathcal{R}$ , however they did not exhibit other behaviour – such as the rapid transfer of energy from low- to high-frequency components – that would suggest instability in the fully nonlinear theory. At late times in their TTF evolution, these solutions project back to the QP surface without altering their energy spectra.

In an effort to find QP solutions through extensions of known solutions, we constructed seed data from low temperature QP solutions that had been padded with extra, zero-energy modes. However, attempting to project back to the solution surface resulted either in solutions that were not robust as  $j_{max}$  was increased, or failure to find any solution at all. When these data were taken as initial conditions for evolution within the TTF description, no new solutions were found as a result of the

evolution. Instead, the inclusion of extra modes caused an isothermal drift away from the known QP seed solution and the Newton-Raphson solver was not able to project the data back to the QP surface. In such cases, the scalar curvature became oscillatory with values ranging up to 20 times the initial curvature. Padding  $T \simeq 5.4$  QP solutions with zero-energy modes once again produced an isothermal drift during evolution and did not converge towards the known QP solution for that temperature and number of modes. These solutions, however, exhibit slow oscillations of scalar curvature over a narrow range of values, hinting at stability over perturbative timescales in the nonlinear theory.

With respect to the overall stability of AdS<sub>4</sub>, as well as the interpretation of stable data in the bulk as non-thermalizing states in the boundary theory, we did not find evidence of families of quasi-periodic solutions with high temperatures that are robust against increasing  $j_{max}$ . It is important to note that we have focused entirely on solutions where the dominant energy contribution is in the  $j = 0$  mode. Other configurations are possible where the dominant energy contribution is in the  $j_r$  mode, with  $r \neq 0$ . As shown in [82], QP solutions for temperatures in certain ranges are degenerate in the value of  $r$ . It may be that the observed temperature limit for QP data we have seen is an indication that the  $r = 0$  family of solutions no longer dominates, and instead the correct quasi-periodic solution is one of the  $r \neq 0$  families. Now that we have established the tools required to examine this possibility, it will be a focus of future research. Also to be considered in the future is the use of QP solutions as initial data for evolution within the fully nonlinear theory in order to help establish a more precise expression for the perturbative timescale  $t_p$ . With this, we can create hybrid evolutions for massless scalar field collapses that use TTF methods for evolutions when  $t < t_p$  before changing to fully nonlinear methods for  $t \geq t_p$ . This would decrease the computational power required to study such collapses without compromising the accuracy of the simulation.

**Acknowledgments** The work of ND is supported in part by a Natural Sciences and Engineering Research Council of Canada PGS-D grant to ND, NSF Grant PHY-1606654 at Cornell University, and by a grant from the Sherman Fairchild Foundation. The work of BC and AF is supported by the Natural Sciences and Engineering Research Council of Canada Discovery Grant program. This

research was enabled in part by support provided by WestGrid ([www.westgrid.ca](http://www.westgrid.ca)) and Compute Canada Calcul Canada ([www.computecanada.ca](http://www.computecanada.ca)).

# Appendix

## 3.A Seeding Methods For Non-Linear Solvers

To generate seed values for the  $\alpha_j$  with  $j \geq 2$ , [82] used the exponential relation

$$\alpha_j \sim \frac{3e^{-\mu j}}{2j + 3} \quad (3.25)$$

in AdS<sub>4</sub>, where  $\mu = \ln(3/5\alpha_1)$ . However, as  $j_{max}$  increased, the seed values diverged significantly from the true solutions (see figure 3.A.2 for a comparison between known QP  $\alpha_j$  values, the seeds generated by (3.25), and the result of the fitting procedure). Although this profile was sufficient for low  $j_{max}$  solutions, above  $j_{max} \gtrsim 150$ , (3.25) no longer provided an adequate starting guess. To overcome this problem, we applied an exponential fit to the tail values of a known QP solution with lower  $j_{max}$ . As explained below, this exponential fit was used to extrapolate the data to a higher  $j_{max}$ .

To err on the side of caution, the  $\alpha_j$  with  $j \in [j_{max} - 30, j_{max} - 10]$  were used from each QP solution to provide more accurate seed values when increasing  $j_{max}$  by 25. See figure 3.A.1 for a comparison of seed values generated by tail fitting to actual QP solutions. The solutions found using this method of seeding versus those found from the seeding given in (3.25) had relative differences on the order of  $10^{-14}$ .

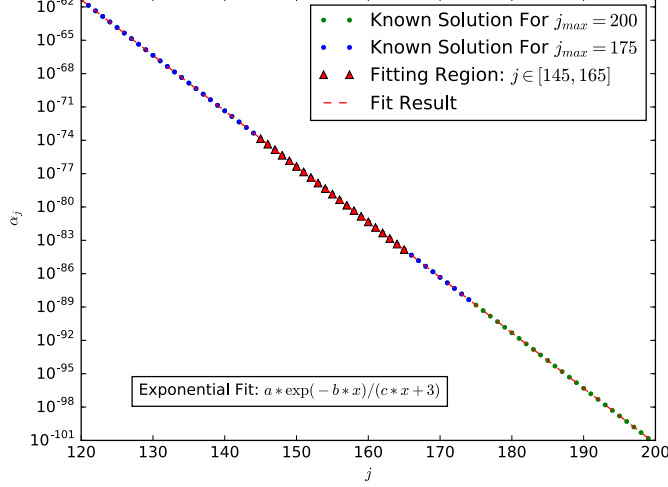


**Figure 3.A.1:** Fitting the tail of the  $j_{max} = 175$  spectrum to construct a seed for  $j_{max} = 200$  at fixed  $\alpha_1 = 0.2$ . Also included is actual QP spectrum for  $j_{max} = 200$ .

### 3.B Auxiliary Integrals For Calculating the $T, R, S$ Coefficients

The auxiliary coefficients  $X, Y, W, W^*, A$ , and  $V$  allow the symmetries of the  $T, R$  and  $S$  coefficients to be more easily recognized and therefore reduce the number of total calculations involved in determining (3.32) - (3.34). These auxiliary coefficients are written simply in terms of the eigenfunctions in (3.9) and their derivatives. Explicitly, they are

$$X_{ijkl} = \int_0^{\pi/2} dx e'_i(x) e_j(x) e_k(x) e_\ell(x) \sin(x) \cos(x) (\tan(x))^{d-1} \quad (3.26)$$

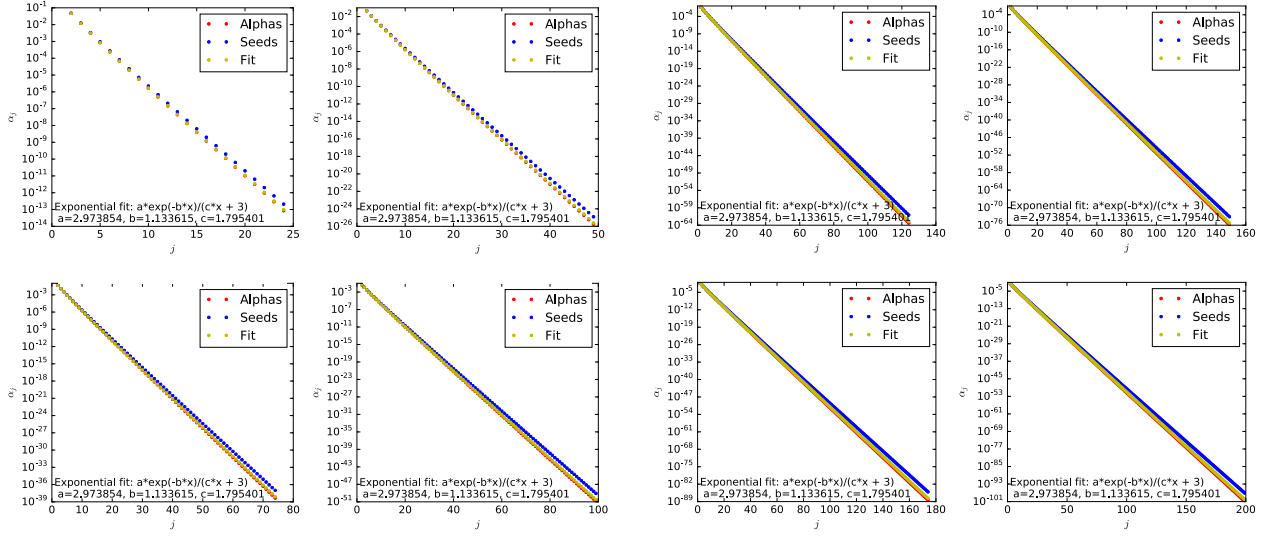
$$Y_{ijkl} = \int_0^{\pi/2} dx e'_i(x) e_j(x) e'_k(x) e'_\ell(x) \sin(x) \cos(x) (\tan(x))^{d-1} \quad (3.27)$$

$$W_{ijkl} = \int_0^{\pi/2} dx e_i(x) e_j(x) \sin(x) \cos(x) \int_0^x dy e_k(y) e_\ell(y) (\tan(y))^{d-1} \quad (3.28)$$

$$W_{ijkl}^* = \int_0^{\pi/2} dx e'_i(x) e'_j(x) \sin(x) \cos(x) \int_0^x dy e_k(y) e_\ell(y) (\tan(y))^{d-1} \quad (3.29)$$

$$A_{ij} = \int_0^{\pi/2} dx e'_i(x) e'_j(x) \sin(x) \cos(x) \quad (3.30)$$

$$V_{ij} = \int_0^{\pi/2} dx e_i(x) e_j(x) \sin(x) \cos(x) . \quad (3.31)$$



(a)  $\alpha_1 = 0.2$  QP solutions for  $j_{max} \in [25, 100]$ .

(b)  $\alpha_1 = 0.2$  QP solutions for  $j_{max} \in [140, 200]$ .

**Figure 3.A.2:** A comparison of seeds predicted by (3.25) to known QP solution. Also included for comparison are the results of fitting the QP solutions to a generic exponential fit.

In terms of these coefficients, the TTF source terms are given by

$$T_\ell = \frac{1}{2}\omega_\ell^2 X_{\ell\ell\ell\ell} + \frac{3}{2}Y_{\ell\ell\ell\ell} + 2\omega_\ell^4 W_{\ell\ell\ell\ell} + 2\omega_\ell^2 W_{\ell\ell\ell\ell}^* - \omega_\ell^2(A_{\ell\ell} + \omega_\ell^2 V_{\ell\ell}) \quad (3.32)$$

$$\begin{aligned} R_{i\ell} &= \frac{1}{2} \left( \frac{\omega_i^2 + \omega_\ell^2}{\omega_\ell^2 - \omega_i^2} \right) (\omega_\ell^2 X_{i\ell\ell i} - \omega_i^2 X_{\ell i i \ell}) + 2 \left( \frac{\omega_\ell^2 Y_{i\ell i \ell} - \omega_i^2 Y_{\ell i i \ell}}{\omega_\ell^2 - \omega_i^2} \right) \\ &\quad + \left( \frac{\omega_i^2 \omega_\ell^2}{\omega_\ell^2 - \omega_i^2} \right) (X_{i\ell\ell i} - X_{\ell i i \ell}) + \frac{1}{2}(Y_{i\ell\ell i} + Y_{\ell i i \ell}) + \omega_i^2 \omega_\ell^2 (W_{\ell i i \ell} + W_{i\ell\ell i}) \\ &\quad + \omega_i^2 W_{\ell i i \ell}^* + \omega_\ell^2 W_{i\ell\ell i}^* - \omega_\ell^2 (A_{ii} + \omega_i^2 V_{ii}) \end{aligned} \quad (3.33)$$

$$\begin{aligned} S_{ijkl} &= -\frac{1}{4} \left( \frac{1}{\omega_i + \omega_j} + \frac{1}{\omega_i - \omega_k} + \frac{1}{\omega_j - \omega_k} \right) (\omega_i \omega_j \omega_k X_{\ell i j k} - \omega_\ell Y_{i \ell j k}) \\ &\quad - \frac{1}{4} \left( \frac{1}{\omega_i + \omega_j} + \frac{1}{\omega_i - \omega_k} - \frac{1}{\omega_j - \omega_k} \right) (\omega_j \omega_k \omega_\ell X_{i j k \ell} - \omega_i Y_{j i k \ell}) \\ &\quad - \frac{1}{4} \left( \frac{1}{\omega_i + \omega_j} - \frac{1}{\omega_i - \omega_k} + \frac{1}{\omega_j - \omega_k} \right) (\omega_i \omega_k \omega_\ell X_{j i k \ell} - \omega_j Y_{i j k \ell}) \\ &\quad - \frac{1}{4} \left( \frac{1}{\omega_i + \omega_j} - \frac{1}{\omega_i - \omega_k} - \frac{1}{\omega_j - \omega_k} \right) (\omega_i \omega_j \omega_\ell X_{k i j \ell} - \omega_k Y_{i k j \ell}). \end{aligned} \quad (3.34)$$

### 3.C Frequency of Solution Checking

The frequency of applying the nonlinear solver to project back down to the QP solution surface is an important part of ensuring that the perturbative method remains applicable. If QP solutions are perturbed by too large an energy, or for too many iterations, the intermediate solutions may not be close enough to the solution surface to provide an adequate seed value. Such was the concern when examining the purported high-temperature solutions from existing sources.

For example, consider the process of applying perturbations of  $\delta E = 0.01\%$  up to some intermediate temperature without projecting back to the QP surface, then projecting back every 100 iterations until a maximum temperature is reached. Starting with the QP solution corresponding to  $\alpha_1 = 0.2$ , the lower panel of figure 3.C.1 shows the result of repeated perturbations of  $\delta E = 0.01\%$  that are not projected back the to QP surface.

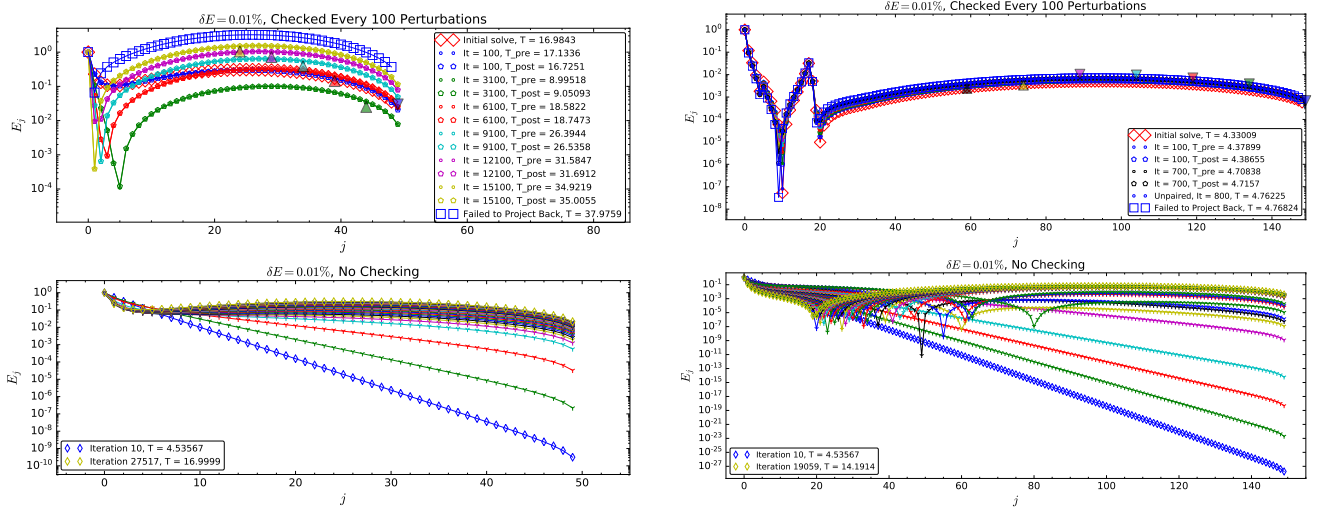


**Figure 3.C.1:** Left: the result of unchecked perturbations of a  $j_{max} = 50$  QP solution up to an intermediate temperature before switching to regular checking. Right: the same procedure is applied to a  $j_{max} = 150$  QP solution.

The behaviour of the spectra differ for the low and high  $j_{max}$  cases. For the  $j_{max} = 50$  solutions, the spectra in the lower panel of the figure can be remain smooth through more than 27,000 iterations of  $\delta E$  perturbations. When a temperature of approximately 17 is reached, the spectrum is used

as a seed value for the nonlinear solver and a smooth solution is found. Continuing with the same  $\delta E$ , but reapplying the nonlinear solver produces mixed results; the temperatures of increasing iterations do not increase monotonically, but do always project back to a solution with nearly the same temperature. However, the spectra themselves are no longer smooth by iteration 3,100. As discussed in § 3.5.1, loss of smoothness is merely indicative of a change of sign in the alpha values; however, this is also accompanies a breakdown of the perturbative conditions in § 3.5. Because only a small number of modes are considered, numerical solutions are still found by the Newton-Raphson solver but no longer represent physical states. Continuing this procedure, we find that the solver fails to find a solution even at the modest temperature of  $T \simeq 38$ .

The behaviour of the  $j_{max} = 150$  solutions is consistent with their lower-mode number counterparts, albeit more pronounced. We see that kinks in the spectrum develop even when the nonlinear solver has not been applied. The intermediate solution used as a seed for the nonlinear solver did not project back to a nearby temperature, instead falling from  $T \simeq 14.2$  to  $T \simeq 4.3$ . As the perturbative procedure continued, projection back to the QP surface was only possible in for a short time before no solutions could be found.

## 4 Perturbative Descriptions of Driven Instabilities in AdS

We have now seen how renormalization flow equations that arise in the TTF allow for secular terms to be absorbed into the definitions of the slowly varying amplitude and phases variables over the perturbative timescale. However, we have only considered gravitational systems whose holographic duals are constrained to instantaneous quenches so far. To better understand more general systems, we wish to extend the perturbative description of gravitational collapse in  $\text{AdS}_{d+1}$  from massless scalars with static boundary conditions to include all allowed masses (both positive and negative mass-squared), as well as time-dependent driving terms on the conformal boundary. This is the focus of the following project: to derive a perturbative theory for a more general class of scalar fields and to examine the effects of time-dependent sources for the fields. As the sole author on this work, all contributions were mine.

# Examining Instabilities Due to Driven Scalars in AdS

Submitted to JHEP [JHEP.252P.0420]

[arXiv:1912.07143](https://arxiv.org/abs/1912.07143)

Brad Cownden<sup>1</sup>

<sup>1</sup>*Department of Physics & Astronomy,*

*University of Manitoba*

*66 Chancellors Cir, Winnipeg, Manitoba R3T 2N2, Canada*

We extend the study of the non-linear perturbative theory of weakly turbulent energy cascades in  $\text{AdS}_{d+1}$  to include solutions of driven systems, i.e. those with time-dependent sources on the AdS boundary. This necessitates the activation of non-normalizable modes in the linear solution for the massive bulk scalar field, which couple to the metric and normalizable scalar modes. We determine analytic expressions for secular terms in the renormalization flow equations for any mass, and for various driving functions. Finally, we numerically evaluate these sources for  $d = 4$  and discuss what role these driven solutions play in the perturbative stability of AdS.

## 4.1 Introduction

Nonlinear instabilities in Anti-de Sitter space have been the subject of examinations on several grounds in addition to the holographic description of quantum quenches via the AdS/CFT correspondence [10, 125], including general stability of maximally-symmetric solutions in general relativity [49, 67, 128], and the study of the growth of secular terms in time-dependent perturbation theories [43, 129]. Numerical studies in holographic AdS show that the eventual collapse of a scalar field into a black hole in the bulk (which is dual to the thermalization of the boundary theory) is generic to any finite sized perturbation [67–69], but can be avoided or delayed for certain initial conditions [39, 83, 86, 88]. The mechanism of collapse in such systems is described as a weakly

turbulent energy cascade to short length scales. These dynamics can be captured by a non-linear perturbation theory at first non-trivial order through the introduction of a second, “slow time” that describes energy transfer between the fundamental modes. This is known as the Two-Time Formalism (TTF) [44] and yields a renormalization flow equation that allows for the absorption of secular terms into renormalized amplitudes and phases [42, 78, 106, 107]. Therefore, stability against a perturbation of order  $\epsilon$  is maintained over time scales of  $t \sim \epsilon^{-2}$ .

Conventional examinations of perturbative stability using TTF have focused on the reaction of the bulk space to some initial energy perturbation, and have aimed to study the balance between direct and inverse energy cascades [82, 111, 112, 130, 131]. Furthermore, numerical examinations of “pumped” scalars and their implications for thermalization of the dual theory have also been examined [30, 97, 98, 100, 132, 133]. However, extensions of the perturbative description to include time-dependent sources – corresponding to a driving term on the boundary of the bulk space – remain unaddressed.

With this in mind, we examine the effects that a time-dependent source on the conformal boundary has on the non-linear perturbative theory. The introduction of a driving term on the boundary means that we must include a second class of fundamental modes with arbitrary frequencies. Since these solutions will have non-finite inner products over the bulk space, they are known as non-normalizable. Non-normalizable modes couple to both the source on the boundary and the regular normalizable modes to bring energy into the system, where direct and inverse energy cascades proceed over perturbative time scales.

To capture these dynamics, we expand the fields in powers of a small perturbation and isolate the secular terms that appear at third order in  $\epsilon$ . Only modes whose frequencies satisfy certain resonance conditions will contribute terms that cannot be absorbed by simple frequency shifts. The form of the resonant terms depends on the specific physics of the system, as well as possible symmetries between frequencies. Finally, by evaluating the resonant third-order interactions when combinations of normalizable and non-normalizable modes are activated, we can write renormalization flow equations for the slowly varying amplitudes and phases.

This paper is organized as follows: section § 4.2 involves a brief discussion of how we arrive at the third order source term, as well as additional considerations due to the time-dependent boundary condition. As an exercise – and to provide explicit expressions for the resonant contributions when the scalar field has non-zero mass – § 4.3 examines the secular terms in the case of a massive scalar field in  $\text{AdS}_{d+1}$  with any mass-squared, up to and including the Breitenlohner-Freedman mass [37]:  $m_{BF}^2 \leq m^2$ . We demonstrate the natural vanishing of two of the three resonances, and then examine the effects of mass-dependence on the non-vanishing channel. Whenever values are calculated, the choice of  $d = 4$  is implied as to draw the most direct comparison to existing literature. In section § 4.4, we extend the boundary conditions to include a variety of periodic boundary sources that couple to non-normalizable modes in the bulk. For each choice of boundary condition, we derive analytic expressions for applicable resonances and evaluate these expressions for different ranges of scalar field masses. Finally, in § 4.5 we discuss the implications of non-vanishing resonances on the competing energy cascades, and the implications for the perturbative stability of such systems. For completeness, we include details of our derivation of the general source term in appendix 4.A, as well as a complete list of possible resonance channels and their resulting secular terms in appendix 4.B for the case of two, equal frequency non-normalizable modes.

## 4.2 Source Terms and Boundary Conditions

Let us first consider a minimally coupled, massive scalar field coupled to a spherically symmetric, asymptotically  $\text{AdS}_{d+1}$  spacetime in global coordinates, whose metric is given by

$$ds^2 = \frac{L^2}{\cos(x)} \left( -A(t, x) e^{-2\delta(t, x)} dt^2 + A^{-1}(t, x) dx^2 + \sin^2(x) d\Omega_{d-1}^2 \right), \quad (4.1)$$

where  $L$  is the AdS curvature (hereafter set to 1), and the radial coordinate  $x \in [0, \pi/2]$ . The dynamics of the system come from the Einstein and Klein-Gordon equations:

$$G_{\mu\nu} + \Lambda g_{\mu\nu} = 8\pi \left( \nabla_\mu \phi \nabla_\nu \phi - \frac{1}{2} g_{\mu\nu} (\nabla^\rho \phi \nabla_\rho \phi + m^2 \phi^2) \right) \quad \text{and} \quad \nabla^2 \phi - m^2 \phi = 0, \quad (4.2)$$

with the cosmological constant for AdS given by  $\Lambda = -d(d-1)/2$ .

Perturbing around static AdS, the scalar field is expanded in odd powers of epsilon

$$\phi(t, x) = \epsilon \phi_1(t, x) + \epsilon^3 \phi_3(t, x) + \dots \quad (4.3)$$

and the metric functions  $A$  and  $\delta$  in even powers,

$$A(t, x) = 1 + \epsilon^2 A_2(t, x) + \dots \quad (4.4)$$

$$\delta(t, x) = \epsilon^2 \delta_2(t, x) + \dots \quad (4.5)$$

We choose to work in the boundary gauge, where  $\delta(t, \pi/2) = 0$ , for reasons that we discuss below.

At linear order,  $\phi_1$  satisfies

$$\partial_t^2 \phi_1 + \hat{L} \phi_1 = 0 \quad \text{where} \quad \hat{L} \equiv \frac{1}{\mu} (\mu' \partial_x + \mu \partial_x^2) - \frac{m^2}{\cos^2(x)}, \quad (4.6)$$

and  $\mu \equiv \tan^{d-1}(x)$ . The general solution for (4.6) in the bulk is a linear combination of the eigenfunctions  $\Phi_I^\pm(x)$ , whose frequencies  $\omega_I$  are arbitrary. Examining each function's scaling when  $x \rightarrow \pi/2$ , we see that  $\Phi_I^+$  is normalizable and goes as  $(\cos x)^{\Delta^+}$  while  $\Phi_I^-$  is non-normalizable and goes as  $(\cos x)^{\Delta^-}$ . We denote the positive (negative) root of  $\Delta(\Delta - d) = m^2$  as  $\Delta^+(\Delta^-)$ .

For an arbitrary frequency, requiring regularity at the origin means that we must choose the linear combination [122]

$$E_I(x) = K_I (\cos(x))^{\Delta^+} {}_2F_1 \left( \frac{\Delta^+ + \omega_I}{2}, \frac{\Delta^+ - \omega_I}{2}, d/2; \sin^2(x) \right), \quad (4.7)$$

that solves the eigenvalue equation

$$\hat{L}E_I(x) = \omega_I^2 E_I(x). \quad (4.8)$$

For special integer values of the frequencies  $\omega_I = \omega_i = 2i + \Delta^+$  with  $i \in \mathbb{Z}^+$ , the functions  $\Phi_i^\pm(x)$  are individually regular at the origin. In this case, the normalizable part of the solution in (4.7) can be written as

$$E_I(x) = e_i(x) = k_i (\cos(x))^{\Delta^+} P_i^{(d/2-1, \Delta^+-d/2)}(\cos(2x)), \quad (4.9)$$

with the Jacobi polynomials  $P_n^{(a,b)}(x)$  providing an orthogonal basis so that  $\langle e_i(x), e_j(x) \rangle = \delta_{ij}$  when

$$k_i = 2 \sqrt{\frac{(i + \Delta^+/2)\Gamma(i+1)\Gamma(i + \Delta^+)}{\Gamma(i+d/2)\Gamma(i + \Delta^+ - d/2 + 1)}}. \quad (4.10)$$

For consistency with other frequency values, we choose to write the non-normalizable contributions in the general form of (4.7).

The interpretation of the driving term through the AdS/CFT dictionary is the addition of a time-dependent part of the boundary Hamiltonian. Therefore, the presence of non-normalizable modes corresponds to pumping energy in and out of the system. We will find it useful when calculating the third-order source term – which requires a triple sum over first-order modes – to be able to separate the contributions from either kind of mode. To that end, we write the first-order part of the scalar field as a sum over both normalizable and non-normalizable modes:

$$\begin{aligned} \phi_1(t, x) &= \sum_I c_I(t) E_I(x) \\ &= \sum_j a_j(t) \cos(\omega_i t + b_i(t)) e_j(x) + \sum_\alpha \bar{A}_\alpha \cos(\omega_\alpha t + \bar{B}_\alpha) E_\alpha(x). \end{aligned} \quad (4.11)$$

The values of  $\bar{A}_\alpha$  and  $\bar{B}_\alpha$  will be set by the driving term. This informs our choice of working in the

boundary gauge; the time  $t$  is the proper time measured on the boundary, as well as the time scale of oscillations from the driving term. In the simplest example, the driving term on the boundary is a single, periodic function

$$\phi_1(t, \pi/2) = \mathcal{A} \cos \bar{\omega} t . \quad (4.12)$$

In this case, (4.11) collapses into a single term so that

$$\sum_{\alpha} \bar{A}_{\alpha} \cos(\omega_{\alpha} t + \bar{B}_{\alpha}) E_{\alpha}(\pi/2) = \mathcal{A} \cos \bar{\omega} t \Rightarrow \bar{A}_{\bar{\omega}} E_{\bar{\omega}}(\pi/2) = \mathcal{A} \quad \text{and} \quad \bar{B}_{\bar{\omega}} = 0 . \quad (4.13)$$

Generalizing the boundary condition to a sum over Fourier modes would set further  $\bar{A}_{\alpha}$  and  $\bar{B}_{\alpha}$  to non-zero values.

Without specifying whether frequencies or basis functions have been chosen to be either normalizable or non-normalizable for the time being, we can show that the  $\mathcal{O}(\epsilon^3)$  part of the scalar field satisfies the equation

$$\ddot{\phi}_3 + \hat{L}\phi_3 = S = 2(A_2 - \delta_2)\ddot{\phi}_1 + (\dot{A}_2 - \dot{\delta}_2)\dot{\phi}_1 + (A'_2 - \delta'_2)\phi'_1 + m^2 A_2 \phi_1 \sec^2 x . \quad (4.14)$$

Following the steps outlined in appendix 4.A, we project (4.14) onto the basis of normalizable modes since all non-normalizable contributions have been fixed by the  $\mathcal{O}(\epsilon)$  boundary condition. Employing a ubiquitous time-dependent solution  $c_I(t) = a_I \cos(\omega_I t + b_I) = a_I \cos \theta_I$  with  $I \in \{i, \alpha\}$ , we find that the source term for the  $\ell^{\text{th}}$  mode is

$$\begin{aligned}
S_\ell = & \frac{1}{4} \sum_{\substack{I,J,K \\ K \neq \ell}}^{\infty} \frac{a_I a_J a_K \omega_K}{\omega_\ell^2 - \omega_K^2} \left[ Z_{IJK\ell}^- (\omega_I + \omega_J - 2\omega_K) \cos(\theta_I + \theta_J - \theta_K) \right. \\
& - Z_{IJK\ell}^- (\omega_I + \omega_J + 2\omega_K) \cos(\theta_I + \theta_J + \theta_K) + Z_{IJK\ell}^+ (\omega_I - \omega_J + 2\omega_K) \cos(\theta_I - \theta_J + \theta_K) \\
& \left. - Z_{IJK\ell}^+ (\omega_I - \omega_J - 2\omega_K) \cos(\theta_I - \theta_J - \theta_K) \right] \\
& + \frac{1}{2} \sum_{\substack{I,J,K \\ I \neq J}}^{\infty} a_I a_J a_K \omega_J \left( H_{IJK\ell} + m^2 V_{JKI\ell} - 2\omega_K^2 X_{IJK\ell} \right) \left[ \frac{1}{\omega_I - \omega_J} \left( \cos(\theta_I - \theta_J - \theta_K) \right. \right. \\
& \left. \left. + \cos(\theta_I - \theta_J + \theta_K) \right) - \frac{1}{\omega_I + \omega_J} \left( \cos(\theta_I + \theta_J - \theta_K) + \cos(\theta_I + \theta_J + \theta_K) \right) \right] \\
& - \frac{1}{4} \sum_{I,J,K}^{\infty} a_I a_J a_K \left[ (2\omega_J \omega_K X_{IJK\ell} + m^2 V_{IJK\ell}) \cos(\theta_I + \theta_J - \theta_K) \right. \\
& - (2\omega_J \omega_K X_{IJK\ell} - m^2 V_{IJK\ell}) \cos(\theta_I - \theta_J - \theta_K) + (2\omega_J \omega_K X_{IJK\ell} + m^2 V_{IJK\ell}) \cos(\theta_I - \theta_J + \theta_K) \\
& \left. - (2\omega_J \omega_K X_{IJK\ell} - m^2 V_{IJK\ell}) \cos(\theta_I + \theta_J + \theta_K) \right] \\
& + \frac{1}{4} \sum_{I,J}^{\infty} a_I a_J a_\ell \omega_\ell \left[ \tilde{Z}_{IJ\ell}^- (\omega_I + \omega_J - 2\omega_\ell) \cos(\theta_I + \theta_J - \theta_\ell) - \tilde{Z}_{IJ\ell}^- (\omega_I + \omega_J + 2\omega_\ell) \cos(\theta_I + \theta_J + \theta_\ell) \right. \\
& \left. + \tilde{Z}_{IJ\ell}^+ (\omega_I - \omega_J + 2\omega_\ell) \cos(\theta_I - \theta_J + \theta_\ell) - \tilde{Z}_{IJ\ell}^+ (\omega_I - \omega_J - 2\omega_\ell) \cos(\theta_I - \theta_J - \theta_\ell) \right] \\
& - \frac{1}{4} \sum_{I,J}^{\infty} a_I^2 a_J \left[ H_{IIJ\ell} + m^2 V_{JII\ell} - 2\omega_J^2 X_{IIJ\ell} \right] \left( \cos(2\theta_I - \theta_J) + \cos(2\theta_I + \theta_J) \right) \\
& - \frac{1}{2} \sum_{I,J}^{\infty} a_I^2 a_J \left[ H_{IIJ\ell} + m^2 V_{JII\ell} - 2\omega_J^2 X_{IIJ\ell} + 4\omega_I^2 \omega_J^2 P_{J\ell I} + 2\omega_I^2 (M_{J\ell I} + m^2 Q_{J\ell I}) \right] \cos \theta_J. \quad (4.15)
\end{aligned}$$

Note that sums and restrictions on indices must be interpreted as sums and restrictions on *frequencies* when any of the modes is non-normalizable, since  $\omega_\alpha \neq 2\alpha + \Delta^+$  in general.

As mentioned above, the growth of resonant terms with time, i.e. secular growth, at  $\mathcal{O}(\epsilon^3)$  can be absorbed into the time-dependent part of the scalar field at that order [43]. Thus, (4.14) tells us that

$$\ddot{c}_\ell^{(3)}(t) + \omega_\ell^2 c_\ell^{(3)}(t) = S_\ell^{(3)} \cos(\omega_\ell t + \varphi_\ell), \quad (4.16)$$

where  $S_\ell^{(3)}$  is a polynomial in  $a_I$  determined by evaluating the resonant contributions from (4.15), and  $\varphi_\ell$  is some combination of the  $b_I$ . To obtain the renormalization flow equations, we can rewrite the amplitudes and phases in terms of renormalized integration constants that exactly cancel the secular terms at each instant. Doing so yields the renormalization flow equations for the renormalized constants [42]

$$\frac{2\omega_\ell}{\epsilon^2} \frac{da_\ell}{dt} = -S_\ell^{(3)} \sin(b_\ell - \varphi_\ell) \quad (4.17)$$

$$\frac{2\omega_\ell a_\ell}{\epsilon^2} \frac{db_\ell}{dt} = -S_\ell^{(3)} \cos(b_\ell - \varphi_\ell) . \quad (4.18)$$

Note that the amplitudes and phases evolve with respect to the “slow time”  $\tau = \epsilon^2 t$ . In practice, once these flow equations can be written down, the perturbative evolution of the system is determined up to a timescale of  $t \sim \epsilon^{-2}$ .

To determine the exact form of  $S_\ell^{(3)}$ , we must consider all combinations of the frequencies  $\{\omega_I, \omega_J, \omega_K\}$  that satisfy the resonance condition

$$\omega_I \pm \omega_J \pm \omega_K = \pm \omega_\ell . \quad (4.19)$$

As an exercise, we first derive the resonant contributions when the boundary source is zero, and therefore only normalizable modes are present. These results agree numerically with previous work on normalizable modes for massless scalars in the interior time gauge ( $\delta(t, 0) = 0$ ) [134]. The definitions of the functions  $Z$ ,  $H$ ,  $X$ , etc. in (4.15) differ slightly from other works – in part because of the gauge choice, and in part because of a desire to separate out mass-dependent terms – and so are given explicitly in appendix 4.A.

## 4.3 Resonances From Normalizable Solutions

Consider the case where each of the basis functions are given by normalizable solutions. The possible combinations of frequencies that satisfy (4.19) can be separated into the three distinct cases:

$$\omega_i + \omega_j + \omega_k = \omega_\ell \quad (+++) \quad (4.20)$$

$$\omega_i - \omega_j - \omega_k = \omega_\ell \quad (+--) \quad (4.21)$$

$$\omega_i + \omega_j - \omega_k = \omega_\ell \quad (++-). \quad (4.22)$$

Note that the  $(+++)$  and  $(+--)$  resonances produce restrictions on the allowed values of the indices  $\{i, j, k\}$ , as well as on values of the mass, since  $\omega_i = 2i + \Delta^+$ . In the first case, the indices are restricted by  $i + j + k = \ell - \Delta^+$ , and so  $\Delta^+$  must be an integer and greater than  $\ell$  for resonance to occur. Similarly, the  $(+--)$  resonance condition becomes  $i - j - k = \ell + \Delta^+$ , which is resonant for any integer value of  $\Delta^+$ . We will see that these two resonance channels will non-trivially vanish whenever their respective resonance conditions are satisfied. This is in agreement with the results shown for the massless scalar in the interior time gauge (as they must be, since the choice of time gauge should not change the existence of resonant channels). Here we include the expressions for the naturally vanishing resonances, choosing to explicitly express the mass dependence.

### 4.3.1 Naturally Vanishing Resonances: $(+++)$ and $(+--)$

Resonant contributions that come from the condition  $\omega_i + \omega_j + \omega_k = \omega_\ell$  contribute to the total source term via

$$S_\ell = \underbrace{\sum_{i=0}^{\infty} \sum_{j=0}^{\infty} \sum_{k=0}^{\infty}}_{\omega_i + \omega_j + \omega_k = \omega_\ell} \Omega_{ijk\ell} a_i a_j a_k \cos(\theta_i + \theta_j + \theta_k) + \dots, \quad (4.23)$$

where the ellipsis denotes other resonances.  $\Omega_{ijkl}$  is given by

$$\begin{aligned}
\Omega_{ijkl} = & -\frac{1}{12}H_{ijkl}\frac{\omega_j(\omega_i + \omega_k + 2\omega_j)}{(\omega_i + \omega_j)(\omega_j + \omega_k)} - \frac{1}{12}H_{ikjl}\frac{\omega_k(\omega_i + \omega_j + 2\omega_k)}{(\omega_i + \omega_k)(\omega_j + \omega_k)} - \frac{1}{12}H_{jikl}\frac{\omega_i(\omega_j + \omega_k + 2\omega_i)}{(\omega_i + \omega_j)(\omega_i + \omega_k)} \\
& - \frac{m^2}{12}V_{ijkl}\left(1 + \frac{\omega_j}{\omega_j + \omega_k} + \frac{\omega_i}{\omega_i + \omega_k}\right) - \frac{m^2}{12}V_{jkl}\left(1 + \frac{\omega_j}{\omega_i + \omega_j} + \frac{\omega_k}{\omega_i + \omega_k}\right) \\
& - \frac{m^2}{12}V_{kijl}\left(1 + \frac{\omega_i}{\omega_i + \omega_j} + \frac{\omega_k}{\omega_j + \omega_k}\right) + \frac{1}{6}\omega_j\omega_kX_{ijkl}\left(1 + \frac{\omega_j}{\omega_i + \omega_k} + \frac{\omega_k}{\omega_i + \omega_j}\right) \\
& + \frac{1}{6}\omega_i\omega_kX_{jkl}\left(1 + \frac{\omega_i}{\omega_j + \omega_k} + \frac{\omega_k}{\omega_i + \omega_j}\right) + \frac{1}{6}\omega_i\omega_jX_{kijl}\left(1 + \frac{\omega_i}{\omega_j + \omega_k} + \frac{\omega_j}{\omega_i + \omega_k}\right) \\
& - \frac{1}{12}Z_{ijkl}^-\left(\frac{\omega_k}{\omega_i + \omega_j}\right) - \frac{1}{12}Z_{ikjl}^-\left(\frac{\omega_j}{\omega_i + \omega_k}\right) - \frac{1}{12}Z_{jkl}^-\left(\frac{\omega_i}{\omega_j + \omega_k}\right). \tag{4.24}
\end{aligned}$$

The second naturally vanishing resonance comes from the condition  $\omega_i - \omega_j - \omega_k = \omega_\ell$ , and contributes to the total source term via

$$S_\ell = \sum_{j=0}^{\infty} \sum_{k=0}^{\infty} \Gamma_{(j+k+\ell+\Delta+)} a_j a_k a_{(j+k+\ell+\Delta+)} \cos(\theta_{(j+k+\ell+\Delta+)} - \theta_j - \theta_k) + \dots, \tag{4.25}$$

where

$$\begin{aligned}
\Gamma_{ijkl} = & \frac{1}{4}H_{ijkl}\frac{\omega_j(\omega_k - \omega_i + 2\omega_j)}{(\omega_i - \omega_j)(\omega_j + \omega_k)} + \frac{1}{4}H_{jkl}\frac{\omega_k(\omega_j - \omega_i + 2\omega_k)}{(\omega_i - \omega_k)(\omega_j + \omega_k)} + \frac{1}{4}H_{kijl}\frac{\omega_i(\omega_j + \omega_k - 2\omega_i)}{(\omega_i - \omega_j)(\omega_i - \omega_k)} \\
& - \frac{1}{2}\omega_j\omega_kX_{ijkl}\left(\frac{\omega_k}{\omega_i - \omega_j} + \frac{\omega_j}{\omega_i - \omega_k} - 1\right) + \frac{1}{2}\omega_i\omega_kX_{jkl}\left(\frac{\omega_k}{\omega_i - \omega_j} + \frac{\omega_i}{\omega_j + \omega_k} - 1\right) \\
& + \frac{1}{2}\omega_i\omega_jX_{kijl}\left(\frac{\omega_j}{\omega_i - \omega_k} + \frac{\omega_i}{\omega_j + \omega_k} - 1\right) + \frac{m^2}{4}V_{jkl}\left(\frac{\omega_j}{\omega_i - \omega_j} + \frac{\omega_k}{\omega_i - \omega_k} - 1\right) \\
& - \frac{m^2}{4}V_{kijl}\left(\frac{\omega_i}{\omega_i - \omega_j} + \frac{\omega_k}{\omega_j + \omega_k} + 1\right) - \frac{m^2}{4}V_{ijkl}\left(\frac{\omega_i}{\omega_i - \omega_k} + \frac{\omega_j}{\omega_j + \omega_k} + 1\right) \\
& + \frac{1}{4}Z_{kijl}^-\left(\frac{\omega_i}{\omega_j + \omega_k}\right) - \frac{1}{4}Z_{ijkl}^+\left(\frac{\omega_k}{\omega_i - \omega_j}\right) - \frac{1}{4}Z_{jkl}^+\left(\frac{\omega_j}{\omega_i - \omega_k}\right). \tag{4.26}
\end{aligned}$$

Building on the work done with massless scalars, we are able to show numerically that (4.24) and (4.26) continue to vanish for massive scalars ( $m^2 \geq m_{BF}^2$ ) in the boundary gauge; thus, the dynamics governing the weakly turbulent transfer of energy are determined only from the remaining resonance channel. When non-normalizable modes are introduced, we will see that naturally vanish-

ing resonances are not present and so the total third-order source term is the sum over all resonant channels.

### 4.3.2 Non-vanishing Resonance: (+ + -)

The first non-vanishing contributions arise when  $\omega_i + \omega_j = \omega_k + \omega_\ell$ . This contribution can be split into three coefficients that are evaluated for certain subsets of the allowed values for the indices, namely

$$S_\ell = T_\ell a_\ell^3 \cos(\theta_\ell + \theta_\ell - \theta_\ell) + \sum_{i \neq \ell}^{\infty} R_{i\ell} a_i^2 a_\ell \cos(\theta_i + \theta_\ell - \theta_i) + \sum_{i \neq \ell}^{\infty} \sum_{j \neq \ell}^{\infty} S_{ij(i+j-\ell)\ell} a_i a_j a_{(i+j-\ell)} \cos(\theta_i + \theta_j - \theta_{i+j-\ell}), \quad (4.27)$$

where the coefficients are given by

$$\begin{aligned} S_{ijkl} = & -\frac{1}{4} H_{kijl} \frac{\omega_i(\omega_j - \omega_k + 2\omega_i)}{(\omega_i - \omega_k)(\omega_i + \omega_j)} - \frac{1}{4} H_{ijkl} \frac{\omega_j(\omega_i - \omega_k + 2\omega_j)}{(\omega_j - \omega_k)(\omega_i + \omega_j)} - \frac{1}{4} H_{jkil} \frac{\omega_k(\omega_i + \omega_j - 2\omega_k)}{(\omega_i - \omega_k)(\omega_j - \omega_k)} \\ & - \frac{1}{2} \omega_j \omega_k X_{ijkl} \left( \frac{\omega_j}{\omega_i - \omega_k} - \frac{\omega_k}{\omega_i + \omega_j} + 1 \right) - \frac{1}{2} \omega_i \omega_k X_{jkil} \left( \frac{\omega_i}{\omega_j - \omega_k} - \frac{\omega_k}{\omega_i + \omega_j} + 1 \right) \\ & + \frac{1}{2} \omega_i \omega_j X_{kijl} \left( \frac{\omega_i}{\omega_j - \omega_k} + \frac{\omega_j}{\omega_i - \omega_k} + 1 \right) - \frac{m^2}{4} V_{ijkl} \left( \frac{\omega_i}{\omega_i - \omega_k} + \frac{\omega_j}{\omega_j - \omega_k} + 1 \right) \\ & + \frac{m^2}{4} V_{jkl} \left( \frac{\omega_k}{\omega_i - \omega_k} - \frac{\omega_j}{\omega_i + \omega_j} - 1 \right) + \frac{m^2}{4} V_{kijl} \left( \frac{\omega_k}{\omega_j - \omega_k} - \frac{\omega_i}{\omega_i + \omega_j} - 1 \right) \\ & + \frac{1}{4} Z_{ijkl}^- \left( \frac{\omega_k}{\omega_i + \omega_j} \right) + \frac{1}{4} Z_{ikjl}^+ \left( \frac{\omega_j}{\omega_i - \omega_k} \right) + \frac{1}{4} Z_{jkil}^+ \left( \frac{\omega_i}{\omega_j - \omega_k} \right), \end{aligned} \quad (4.28)$$

$$\begin{aligned} R_{i\ell} = & \left( \frac{\omega_i^2}{\omega_\ell^2 - \omega_i^2} \right) (Y_{i\ell\ell i} - Y_{i\ell i\ell} + \omega_\ell^2 (X_{i\ell i\ell} - X_{\ell i i\ell})) + \left( \frac{\omega_i^2}{\omega_\ell^2 - \omega_i^2} \right) (H_{\ell i i\ell} + m^2 V_{i i\ell\ell} - 2\omega_i^2 X_{\ell i i\ell}) \\ & - \left( \frac{\omega_\ell^2}{\omega_\ell^2 - \omega_i^2} \right) (H_{i\ell i\ell} + m^2 V_{\ell i i\ell} - 2\omega_i^2 X_{i\ell i\ell}) - \frac{m^2}{4} (V_{i\ell i\ell} + V_{i i\ell\ell}) + \omega_i^2 \omega_\ell^2 (P_{i\ell i\ell} - 2P_{\ell i i\ell}) \\ & - \omega_i \omega_\ell X_{i\ell i\ell} - \frac{3m^2}{2} V_{i\ell i\ell} - \frac{1}{2} H_{i i\ell\ell} + \omega_\ell^2 B_{i i\ell} - \omega_i^2 M_{\ell i i\ell} - m^2 \omega_i^2 Q_{\ell i i\ell}, \end{aligned} \quad (4.29)$$

and

$$T_\ell = \frac{1}{2} \omega_\ell^2 (X_{\ell\ell\ell} + 4B_{\ell\ell\ell} - 2M_{\ell\ell\ell} - 2m^2 Q_{\ell\ell\ell}) - \frac{3}{4} (H_{\ell\ell\ell} + 3m^2 V_{\ell\ell\ell}) . \quad (4.30)$$

Following the form of (4.17) - (4.18), these resonant terms set the evolution of the renormalized integration coefficients to be [78]

$$\frac{2\omega_\ell}{\epsilon^2} \frac{da_\ell}{dt} = - \sum_{i \neq \ell}^{\infty} \sum_{j \neq \ell}^{\infty} S_{ij(i+j-\ell)\ell} a_i a_j a_{(i+j-\ell)} \sin(b_\ell + b_{(i+j-\ell)} - b_i - b_j) , \quad (4.31)$$

$$\begin{aligned} \frac{2\omega_\ell a_\ell}{\epsilon^2} \frac{db_\ell}{dt} &= -T_\ell a_\ell^3 - \sum_{i \neq \ell}^{\infty} R_{i\ell} a_i^2 a_\ell \\ &\quad - \sum_{i \neq \ell}^{\infty} \sum_{j \neq \ell}^{\infty} S_{ij(i+j-\ell)\ell} a_i a_j a_{(i+j-\ell)} \cos(b_\ell + b_{(i+j-\ell)} - b_i - b_j) . \end{aligned} \quad (4.32)$$

To examine the effects of non-zero masses on  $R$ ,  $S$ , and  $T$ , we evaluate (4.28)-(4.30) for tachyonic, massless, and massive scalars in figure 4.1. The result is a vertical shift in the coefficient value that is proportional to the choice of mass-squared. By inspection, there is an indication that this shift increases with increasing  $\ell$  values; however, a numerical fit of the data would be needed to claim this definitively.

## 4.4 Resonances From Non-normalizable Modes

Now let us consider the excitation of non-normalizable modes by a driving term on the boundary of AdS. Having set  $\omega_\ell$  to be a normalizable mode, we may ask what restrictions exist on our choices for the other frequencies,  $\{\omega_i, \omega_j, \omega_k\}$ . Aside from the trivial case where all modes are normalizable, we could imagine that one of the modes is non-normalizable. However, this would violate the resonance condition (4.19); thus, at least two modes must be non-normalizable. When three non-normalizable modes exist, there are two possibilities: first, that any combination of generically non-integer frequencies gives a non-integer value and so does not contribute a secular term when

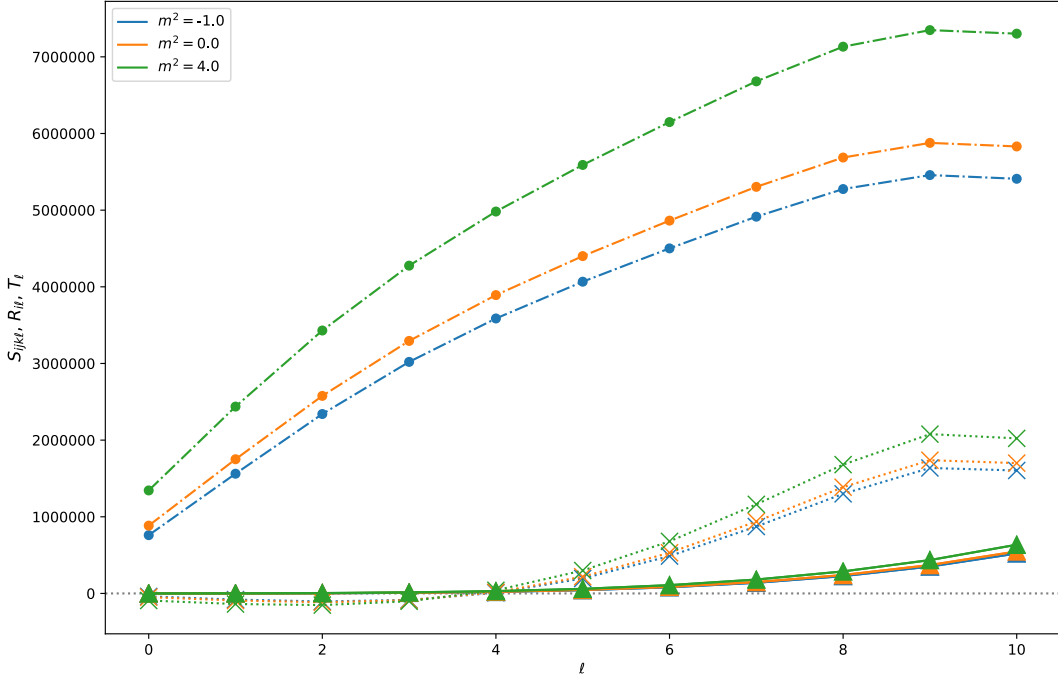


**Figure 4.1:** Evaluating (4.28)-(4.30) over different values of  $m^2$  for  $\ell \leq 10$ .  $S_{ij(i+j-\ell)\ell}$  is denoted by filled circles connected by dash-dotted lines;  $R_{\ell\ell}$  is denoted by filled triangles connected by solid lines;  $T_{\ell\ell}$  is denoted by large Xs connected by dotted lines. Different values of  $m^2$  are denoted by the colour of each series.

projected onto the  $\omega_\ell$  basis; second, some particular combination of the non-normalizable frequencies gives an integer frequency, in which case there are resonant contributions to  $S_\ell^{(3)}$ . Therefore, the pertinent question is what resonances are possible when two of  $\{\omega_i, \omega_j, \omega_j\}$  are non-normalizable? Because this choice breaks some of the symmetries that contributed to the previous expressions for resonance channels, the resonance conditions must be re-examined starting from the source expression (4.15).

Before proceeding further, an important consideration is what the effect of non-normalizable modes are on the perturbative expansion that leads to the source equations. Since non-normalizable solutions do not have well-defined norms, we do not know *a priori* that the inner products described in appendix 4.A are still finite. To investigate this, consider the generic expression for the second-order metric function

$$A_2 = -\nu \int_0^x dy \mu \left( (\dot{\phi}_1)^2 + (\phi'_1)^2 + m^2 \phi_1^2 \sec^2 x \right), \quad (4.33)$$

in the limit of  $x \rightarrow \pi/2$ , and let the scalar field  $\phi_1$  be given by a generic superposition of normalizable and non-normalizable eigenfunctions as in (4.11). Ignoring the time-dependent contributions, we find that

$$\lim_{\tilde{x} \rightarrow 0} A_2(\tilde{x} \equiv \pi/2 - x) = \tilde{x}^{-\xi} \left( \frac{2\tilde{x}^{2+d}}{2-\xi} - \frac{\tilde{x}^d(1+(\Delta^-)^2)}{\xi} \right), \quad (4.34)$$

where we have defined  $\xi = \sqrt{d^2 + 4m^2}$ . In the massless case,  $\xi = d$  and all powers of  $\tilde{x}$  are non-negative; thus, the limit is finite. For tachyonic masses,  $m_{BF}^2 < m^2 < 0$  so that  $0 < \xi < d$  and the limit is again finite. However, when  $m^2 > 0$ , part of the limit diverges. In order for the boundary to remain asymptotically AdS, counter-terms in the bulk action would be required to cancel such divergences – a case we will not address presently. Furthermore, for masses that saturate the Breitenlohner-Freedman bound, the limit would have to be re-evaluated. We will therefore restrict our discussion to  $m_{BF}^2 < m^2 \leq 0$  to avoid these issues. A similar check on the near-boundary behaviour of  $\delta_2$  shows that the gauge condition  $\delta_2(t, \pi/2) = 0$  remains unchanged by the addition of non-normalizable modes given the same restrictions on the mass of the scalar field. With these restrictions in mind, let us now examine the resonances produced by the activation of non-normalizable modes.

#### 4.4.1 Two Non-normalizable Modes with Equal Frequencies

As a first case, let us assume that the two non-normalizable modes have equal, constant, and arbitrary frequencies,  $\bar{\omega}$  (and therefore amplitudes  $\bar{A}_{\bar{\omega}}$ ). The resonance condition (4.19) will only be satisfied when one of  $\{\omega_I, \omega_J, \omega_K\}$  are normalizable. In particular, we find that the following combinations are resonant:

$$\omega_i - \omega_j + \omega_k - \omega_\ell = 0 \quad \Rightarrow \quad \text{either } \omega_i \text{ or } \omega_k \text{ is normalizable} \quad (4.35)$$

$$\omega_i + \omega_j - \omega_k - \omega_\ell = 0 \quad \Rightarrow \quad \text{either } \omega_i \text{ or } \omega_j \text{ is normalizable} \quad (4.36)$$

$$\omega_i - \omega_j - \omega_k + \omega_\ell = 0 \quad \Rightarrow \quad \text{either } \omega_j \text{ or } \omega_k \text{ is normalizable.} \quad (4.37)$$

When any of these resonance conditions is met, the remaining normalizable mode will have a frequency equal to  $\omega_\ell$ , collapsing all sums over frequencies so that

$$S_\ell = \bar{T}_\ell a_\ell \bar{A}_\omega^2 \cos(\theta_\ell) + \dots , \quad (4.38)$$

where the amplitudes of the non-normalizable modes  $\bar{A}_\omega$  are set by the choice of boundary condition. Collecting the appropriate terms in (4.15) and evaluating each possible resonance, we find that

$$\begin{aligned} \bar{T}_\ell = & \left[ \frac{1}{2} Z_{\ell\bar{\omega}\omega\ell}^- \left( \frac{\bar{\omega}}{\omega_\ell + \bar{\omega}} \right) + \frac{1}{2} Z_{\ell\bar{\omega}\omega\ell}^+ \left( \frac{\bar{\omega}}{\omega_\ell - \bar{\omega}} \right) + H_{\ell\bar{\omega}\omega\ell} \left( \frac{\bar{\omega}^2}{\omega_\ell^2 - \bar{\omega}^2} \right) - H_{\bar{\omega}\ell\bar{\omega}\ell} \left( \frac{\omega_\ell^2}{\omega_\ell^2 - \bar{\omega}^2} \right) \right]_{\bar{\omega} \neq \omega_\ell} \\ & - m^2 V_{\ell\bar{\omega}\omega\ell} \left( \frac{\omega_\ell^2}{\omega_\ell^2 - \bar{\omega}^2} \right) + m^2 V_{\bar{\omega}\omega\ell\ell} \left( \frac{\bar{\omega}^2}{\omega_\ell^2 - \bar{\omega}^2} \right) + 2X_{\bar{\omega}\omega\ell\ell} \left( \frac{\bar{\omega}^2 \omega_\ell^2}{\omega_\ell^2 - \bar{\omega}^2} \right) - 2X_{\ell\bar{\omega}\bar{\omega}\ell} \left( \frac{\bar{\omega}^4}{\omega_\ell^2 - \bar{\omega}^2} \right) \\ & + \omega_\ell^2 X_{\bar{\omega}\omega\ell\ell} - \bar{\omega}^2 X_{\ell\bar{\omega}\bar{\omega}} - \frac{3}{2} m^2 V_{\ell\bar{\omega}\bar{\omega}\ell} - \frac{1}{2} m^2 V_{\bar{\omega}\omega\ell\ell} - \frac{1}{2} H_{\bar{\omega}\omega\ell\ell} + \omega_\ell^2 \tilde{Z}_{\bar{\omega}\omega\ell}^+ - 2\bar{\omega}^2 \omega_\ell^2 P_{\ell\bar{\omega}\bar{\omega}} \\ & - \bar{\omega}^2 (\omega_\ell^2 P_{\ell\bar{\omega}\bar{\omega}} - B_{\ell\bar{\omega}\bar{\omega}}) . \end{aligned} \quad (4.39)$$

Notice that the terms in the square braces only contribute when  $\bar{\omega} \neq \omega_\ell$ . Beginning from (4.15), only terms in the square braces that are proportional to  $Z^\pm$  are limited in this way; the remaining terms have no such restriction. However, it can be shown that integral functions with permuted indices are equal when the non-normalizable frequency equals the normalizable frequency. Upon simplification, factors of  $\omega_\ell^2 - \bar{\omega}^2$  are cancelled, and the overall contribution to  $T_\ell$  from the terms in the braces is zero. Thus, these terms are grouped with those that have natural restrictions on the indices.

With the resonant contributions determined, the renormalization flow equations for two equal, constant, non-normalizable frequencies follow from (4.17) - (4.18) and are

$$\frac{2\omega_\ell}{\epsilon^2} \frac{da_\ell}{dt} = 0 \quad \text{and} \quad \frac{2\omega_\ell a_\ell}{\epsilon^2} \frac{db_\ell}{dt} = -\bar{T}_\ell a_\ell \bar{A}_\omega^2 . \quad (4.40)$$

Qualitatively, we see that instead of both the amplitude and the phase running with respect to  $\tau$ , only the phase changes in time. Indeed, (4.40) tells us that  $b_\ell$  is a linear function of  $\tau$  with a slope

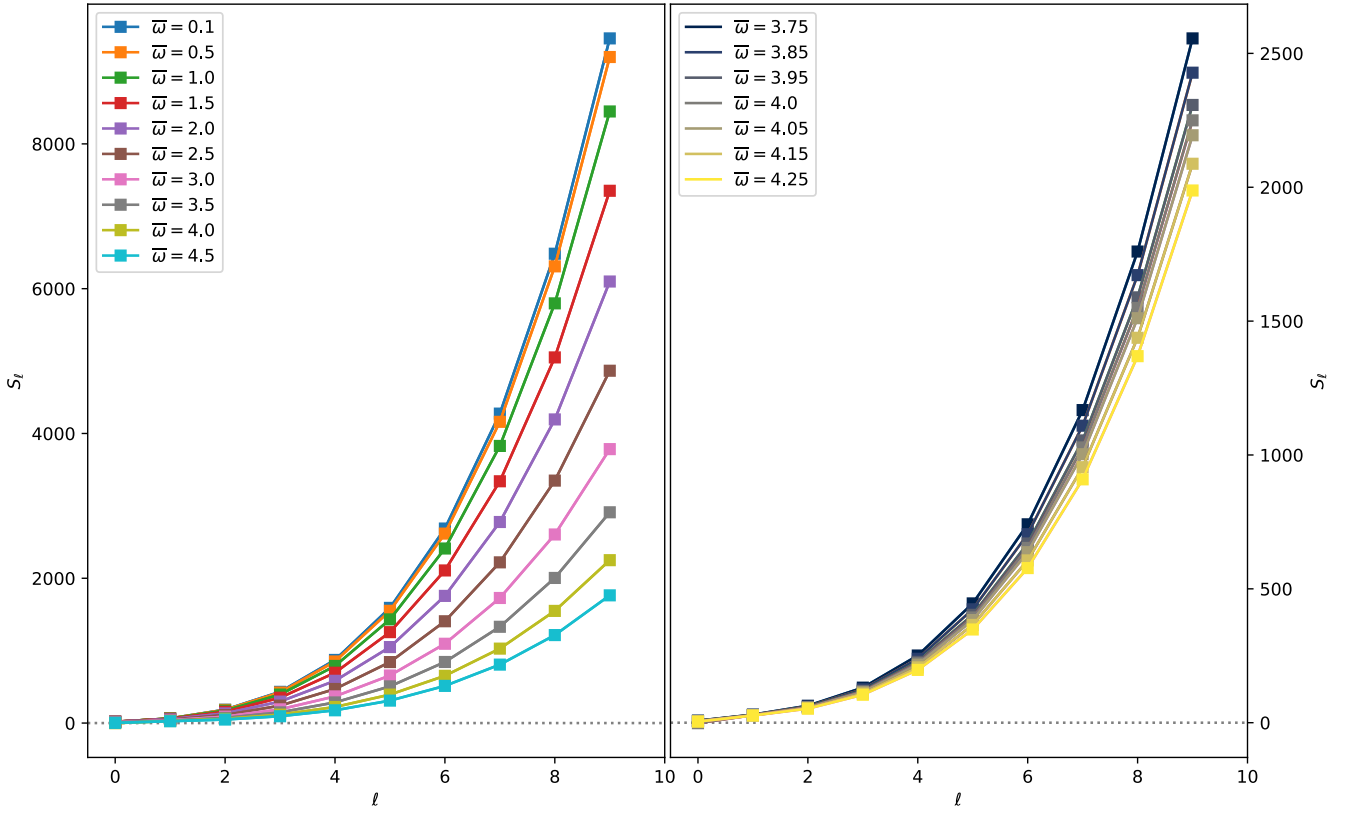


**Figure 4.2:** Left: Evaluating (4.39) when  $m^2 = 0$  for various choices of  $\bar{\omega}$ . Right: The behaviour of  $S_\ell$  for  $\bar{\omega}$  values near  $\omega_0$ .

that is determined by the  $\mathcal{O}(\epsilon^3)$  physics encapsulated by  $\bar{T}_\ell$ .

Other resonant contributions become possible for more restrictive values of the non-normalizable frequency, such as if  $\bar{\omega}$  is allowed to be an integer. These contributions are denoted by the ellipsis in (4.38) and are listed in appendix 4.B. In figures 4.2 and 4.3, we evaluate (4.39) for  $\ell < 10$  over a variety of  $\bar{\omega}$  values first for a massless scalar, then for a tachyonic scalar. For both values of mass-squared,  $T_\ell$  demonstrates power law-type behaviour as a function of  $\ell$  with a leading coefficient that is proportional to the non-normalizable frequency  $\bar{\omega}$ . We also see that the limit of (4.39) as  $\bar{\omega} \rightarrow \omega_0$  is well-defined in both cases.

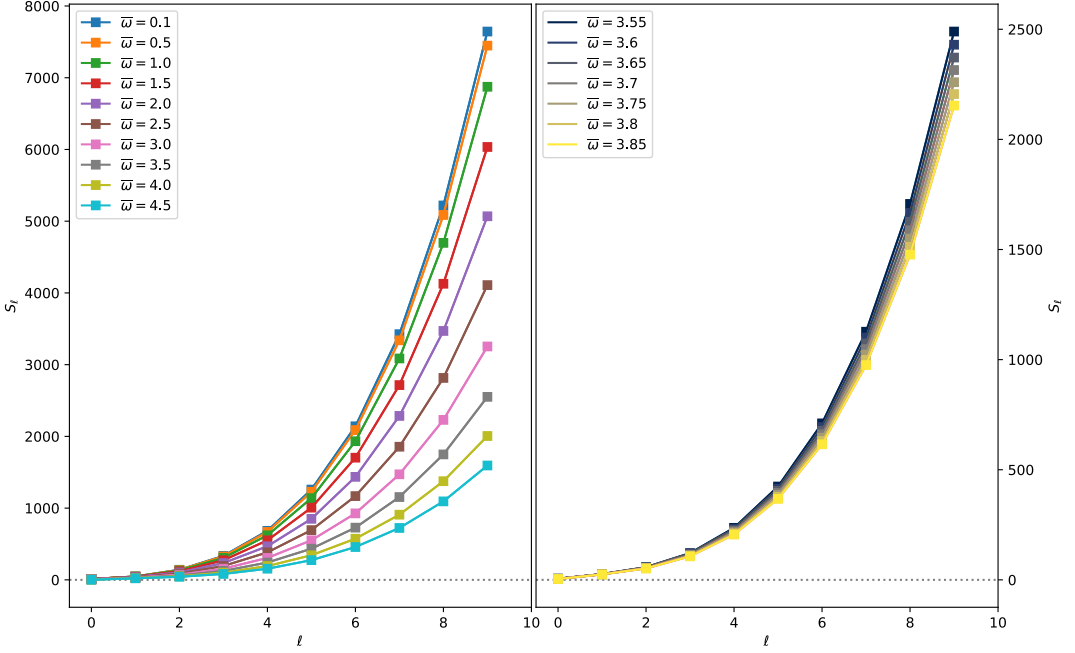


**Figure 4.3:** *Left:* Evaluating  $\bar{T}_\ell$  for a tachyon with  $m^2 = -1.0$ . *Right:* The behaviour of  $S_\ell$  near  $\omega_0 = \Delta^+ \approx 3.7$ .

#### 4.4.2 Special Values of Non-normalizable Frequencies

Let us now consider special values of non-normalizable frequencies that will lead to a greater number of resonance channels. While general non-normalizable frequencies do not require any such restrictions, we will find it informative to examine these special cases as they possess more symmetry in index/frequency values than the case of equal non-normalizable frequencies, but less than all-normalizable modes.

##### 4.4.2.1 Add to an integer

First, we choose two of the modes to be non-normalizable with frequencies  $\bar{\omega}_1$  and  $\bar{\omega}_2$  that add to give an integer:  $\bar{\omega}_1 + \bar{\omega}_2 = 2n$  where  $n = 1, 2, 3, \dots$  (note that the  $n = 0$  case means that both  $\bar{\omega}_1$  and  $\bar{\omega}_2$  would need to be zero by the positive-frequency requirement and so would not contribute). Furthermore, either frequency need not be an integer and therefore the difference  $|\bar{\omega}_1 - \bar{\omega}_2|$  will, in general, not be an integer. In § 4.4.3, we examine the case when the difference of non-normalizable

frequencies is an integer.

When we consider possible resonance channels, we see that resonances can be grouped into

$$(++) : \omega_i + 2n = \omega_\ell \quad \forall \ell \geq n \quad (4.41)$$

$$(+-) : \omega_i - 2n = \omega_\ell \quad \forall n \quad (4.42)$$

for any  $m_{BF}^2 < m^2 < 0$ . However, for a massless scalar, we have an additional channel

$$(-+) : -\omega_i + 2n = \omega_\ell \quad \forall n \geq \ell + d. \quad (4.43)$$

Adding the channels together, the total source term is

$$\begin{aligned} S_\ell = & \sum_{\bar{\omega}_1 + \bar{\omega}_2 = 2n} \left[ \Theta(n - \ell - d) \bar{R}_{(n-\ell-d)\ell}^{(-+)} \bar{A}_1 \bar{A}_2 a_{(n-\ell-d)} \cos(\theta_{(n-\ell-d)} - \theta_1 - \theta_2) \right]_{m^2=0} \\ & + \sum_{\bar{\omega}_1 + \bar{\omega}_2 = 2n} \Theta(\ell - n) \bar{R}_{(\ell-n)\ell}^{(++)} \bar{A}_1 \bar{A}_2 a_{(\ell-n)} \cos(\theta_{(\ell-n)} + \theta_1 + \theta_2) \\ & + \sum_{\bar{\omega}_1 + \bar{\omega}_2 = 2n} \bar{R}_{(\ell+n)\ell}^{(+-)} \bar{A}_1 \bar{A}_2 a_{(\ell+n)} \cos(\theta_{(\ell+n)} - \theta_1 - \theta_2) \\ & + \bar{T}_\ell \bar{A}_1 \bar{A}_2 a_\ell \cos(\theta_\ell) \end{aligned} \quad (4.44)$$

where the Heaviside step function  $\Theta(x)$  enforces the restrictions on the indices in (4.41) and (4.43) and  $\theta_1 = \bar{\omega}_1 t + \bar{B}_1$ , etc.

In the following expressions, the sum over all  $\bar{\omega}_1, \bar{\omega}_2$  such that  $\bar{\omega}_1 + \bar{\omega}_2 = 2n$  is implied, and only the restrictions on individual frequencies are included. Examining each channel in (4.44) individually,

we find

$$\begin{aligned}
\bar{R}_{i\ell}^{(++)} = & -\frac{1}{4} \sum_{\bar{\omega}_2 \neq \omega_\ell} \frac{\bar{\omega}_2}{\omega_\ell - \bar{\omega}_2} Z_{i12\ell}^- - \frac{1}{4} \sum_{\bar{\omega}_1 \neq \omega_\ell} \frac{\bar{\omega}_1}{\omega_\ell - \bar{\omega}_1} Z_{i21\ell}^- - \frac{1}{8n} (\omega_\ell - 2n) Z_{12i\ell}^- \\
& - \frac{1}{4} \sum_{\omega_i \neq \bar{\omega}_1} \frac{1}{\omega_\ell - \bar{\omega}_2} \left[ \bar{\omega}_1 (H_{i12\ell} + m^2 V_{12i\ell} - 2\bar{\omega}_2^2 X_{i12\ell}) + (\omega_\ell - 2n) (H_{1i2\ell} + m^2 V_{i21\ell} - 2\bar{\omega}_2^2 X_{1i2\ell}) \right] \\
& - \frac{1}{4} \sum_{\omega_i \neq \bar{\omega}_2} \frac{1}{\omega_\ell - \bar{\omega}_1} \left[ \bar{\omega}_2 (H_{i21\ell} + m^2 V_{21i\ell} - 2\bar{\omega}_1^2 X_{i21\ell}) + (\omega_\ell - 2n) (H_{2i1\ell} + m^2 V_{i12\ell} - 2\bar{\omega}_1^2 X_{2i1\ell}) \right] \\
& - \frac{1}{8n} \sum_{\bar{\omega}_1 \neq \bar{\omega}_2} \left[ \bar{\omega}_1 H_{21i\ell} + \bar{\omega}_2 H_{12i\ell} + m^2 (\bar{\omega}_1 V_{1i2\ell} + \bar{\omega}_2 V_{2i1\ell}) - (\omega_\ell - 2n)^2 (\bar{\omega}_1 X_{21i\ell} + \bar{\omega}_2 X_{12i\ell}) \right] \\
& + \frac{1}{2} \left[ \bar{\omega}_1 \bar{\omega}_2 X_{i12\ell} + (\omega_\ell - 2n) (\bar{\omega}_1 X_{21i\ell} + \bar{\omega}_2 X_{12i\ell}) - \frac{m^2}{2} (V_{i12\ell} + V_{i21\ell} + V_{12i\ell}) \right]. \tag{4.45}
\end{aligned}$$

The notation  $X_{i12\ell}$  corresponds to evaluating  $X_{ijk\ell}$  with  $\omega_j = \bar{\omega}_1$  and  $\omega_k = \bar{\omega}_2$ . Next, we find that

$$\begin{aligned}
\bar{R}_{i\ell}^{(+)} = & -\frac{1}{4} \left[ \frac{(\omega_\ell + 2n)}{2n} Z_{12i\ell}^- + 2(\omega_\ell + 2n) (\bar{\omega}_1 X_{21i\ell} + \bar{\omega}_2 X_{12i\ell}) \right. \\
& - \frac{\bar{\omega}_1}{(\omega_\ell + \bar{\omega}_2)} (H_{i12\ell} + m^2 V_{12i\ell} - 2\bar{\omega}_2^2 X_{i12\ell}) + \frac{(\omega_\ell + 2n)}{(\omega_\ell + \bar{\omega}_2)} (H_{1i2\ell} + m^2 V_{i21\ell} - 2\bar{\omega}_2^2 X_{1i2\ell}) \\
& - \frac{\bar{\omega}_2}{(\omega_\ell + \bar{\omega}_1)} (H_{i21\ell} + m^2 V_{21i\ell} - 2\bar{\omega}_1^2 X_{i21\ell}) + \frac{(\omega_\ell + 2n)}{(\omega_\ell + \bar{\omega}_1)} (H_{2i1\ell} + m^2 V_{i12\ell} - 2\bar{\omega}_1^2 X_{2i1\ell}) \\
& \left. - 2\bar{\omega}_1 \bar{\omega}_2 X_{i12\ell} + m^2 (V_{12i\ell} + V_{i12\ell} + V_{i21\ell}) \right] + \frac{1}{4} \sum_{\bar{\omega}_2 \neq \omega_\ell} \frac{\bar{\omega}_1 \bar{\omega}_2 (\omega_\ell + 2n)}{\omega_\ell + \bar{\omega}_2} (X_{21i\ell} - X_{\ell i12}) \\
& + \frac{1}{4} \sum_{\bar{\omega}_1 \neq \omega_\ell} \frac{\bar{\omega}_1 \bar{\omega}_2 (\omega_\ell + 2n)}{\omega_\ell + \bar{\omega}_1} (X_{12i\ell} - X_{\ell i12}). \tag{4.46}
\end{aligned}$$

When  $m^2 = 0$ , we have contributions from

$$\begin{aligned}
\bar{R}_{i\ell}^{(-+)} &= \frac{1}{4} \sum_{\bar{\omega}_2 \neq \omega_\ell} \frac{\bar{\omega}_2}{\omega_\ell - \bar{\omega}_2} Z_{i12\ell}^+ + \frac{1}{4} \sum_{\bar{\omega}_1 \neq \omega_\ell} \frac{\bar{\omega}_1}{\omega_\ell - \bar{\omega}_1} Z_{i21\ell}^+ + \frac{1}{4} \sum_{i \neq \ell} \left( \frac{2n - \omega_\ell}{2n} \right) Z_{12i\ell}^- \\
&\quad + \frac{1}{4} \sum_{\bar{\omega}_1 \neq \omega_i} \frac{1}{\omega_i - \bar{\omega}_1} \left[ \bar{\omega}_1 (H_{i12\ell} - 2\bar{\omega}_2^2 X_{i12\ell}) - (2n - \omega_\ell) (H_{1i2\ell} - 2\bar{\omega}_2^2 X_{1i2\ell}) \right] \\
&\quad + \frac{1}{4} \sum_{\bar{\omega}_2 \neq \omega_i} \frac{1}{\omega_i - \bar{\omega}_2} \left[ \bar{\omega}_2 (H_{i21\ell} - 2\bar{\omega}_1^2 X_{i21\ell}) - (2n - \omega_\ell) (H_{2i1\ell} - 2\bar{\omega}_1^2 X_{2i1\ell}) \right] \\
&\quad - \frac{1}{8n} \sum_{\bar{\omega}_1 \neq \bar{\omega}_2} \left[ \bar{\omega}_1 H_{21i\ell} + \bar{\omega}_2 H_{12i\ell} - 2(2n - \omega_\ell)^2 (\bar{\omega}_1 X_{21i\ell} + \bar{\omega}_2 X_{12i\ell}) \right] \\
&\quad - \frac{1}{2} \left[ (2n - \omega_\ell) (\bar{\omega}_1 X_{21i\ell} + \bar{\omega}_2 X_{12i\ell}) - \bar{\omega}_1 \bar{\omega}_2 X_{i12\ell} \right]. \tag{4.47}
\end{aligned}$$

*NB.* In (4.47) only,  $\omega_i = 2i + \Delta^+ = 2i + d$  since this term requires that  $m^2 = 0$  to contribute. We maintain the same notation out of convenience, despite the special case. Finally,

$$\begin{aligned}
\bar{T}_\ell &= \frac{1}{2} \omega_\ell^2 \left( \tilde{Z}_{11\ell}^+ + \tilde{Z}_{22\ell}^+ \right) - \frac{1}{2} \left[ H_{11\ell\ell} + H_{22\ell\ell} + m^2 (V_{\ell11\ell} + V_{\ell22\ell}) - 2\omega_\ell^2 (X_{11\ell\ell} + X_{22\ell\ell}) \right. \\
&\quad \left. + 4\omega_\ell^2 (\bar{\omega}_1^2 P_{\ell\ell 1} + \bar{\omega}_2^2 P_{\ell\ell 2}) + 2\bar{\omega}_1^2 M_{\ell\ell 1} + 2\bar{\omega}_2^2 M_{\ell\ell 2} + 2m^2 (\bar{\omega}_1^2 Q_{\ell\ell 1} + \bar{\omega}_2^2 Q_{\ell\ell 2}) \right]. \tag{4.48}
\end{aligned}$$

In figure 4.4, we compute the total source term (modulo the amplitudes  $a_i$  and  $\bar{A}_\alpha$ ) for a tachyonic scalar with  $n = 2$ . Figure 4.5 provides a comparison between the value of the source term for a massless scalar between two choices of  $n$ : one that includes contributions from  $\bar{R}_{i\ell}^{(-+)}$  and one that does not. As expected, the source terms are symmetric in  $\bar{\omega}_1 \leftrightarrow \bar{\omega}_2$ , hence only  $\bar{\omega}_1 \leq n$  data are shown. As a function of  $\ell$ , (4.44) starts near zero before becoming increasingly negative as  $\ell$  becomes large. As a check for naturally vanishing channels, the absolute value of the sum of  $S_\ell$  is also plotted; however, there is no indication that any channel vanishes for any of the  $\bar{\omega}_1, \bar{\omega}_2$  values considered.

The renormalization flow equations include the sum of all the channels (none of which vanish

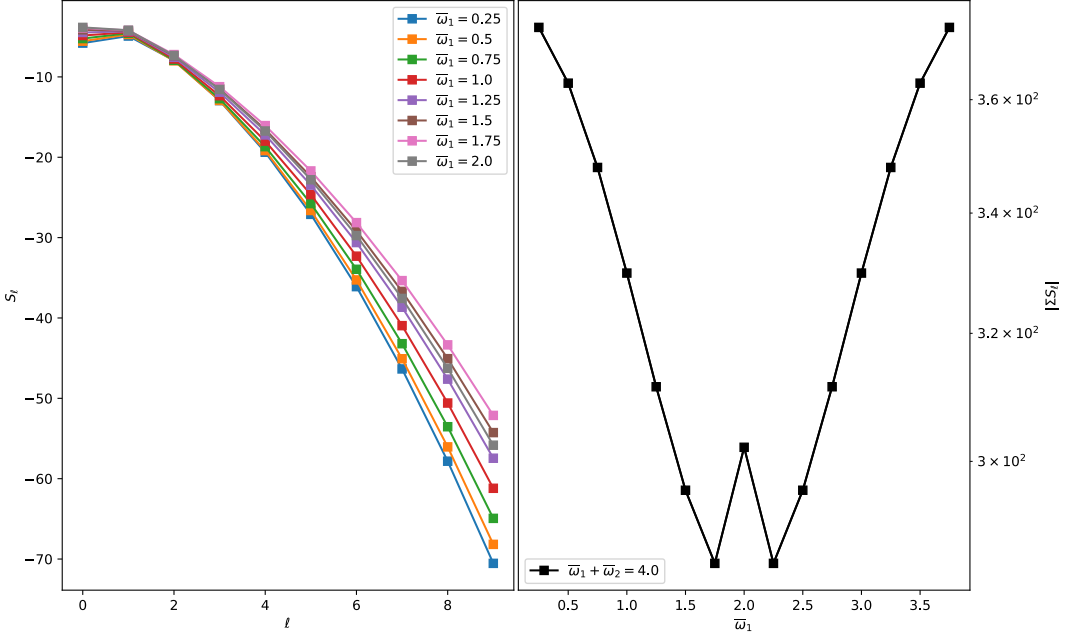


**Figure 4.4:** Left: Source term values for a tachyonic scalar with  $m^2 = -1.0$  when the frequencies of non-normalizable modes sum to 4.0. Right: The absolute value of the sum of the source terms for each choice of  $\bar{\omega}_1$ ,  $\bar{\omega}_2$ .

naturally), and are

$$\begin{aligned} \frac{2\omega_\ell}{\epsilon^2} \frac{da_\ell}{dt} = & - \sum_{\bar{\omega}_1 + \bar{\omega}_2 = 2n} \left[ \Theta(n - \ell - d) \bar{R}_{(n-\ell-d)\ell}^{(-+)} \bar{A}_1 \bar{A}_2 a_{(n-\ell-d)} \sin(b_{(n-\ell-d)} - \bar{B}_1 - \bar{B}_2) \right]_{m^2=0} \\ & - \sum_{\bar{\omega}_1 + \bar{\omega}_2 = 2n} \Theta(\ell - n) \bar{R}_{(\ell-n)\ell}^{(++)} \bar{A}_1 \bar{A}_2 a_{(\ell-n)} \sin(b_{(\ell-n)} + \bar{B}_1 + \bar{B}_2) \\ & - \sum_{\bar{\omega}_1 + \bar{\omega}_2 = 2n} \bar{R}_{(\ell+n)\ell}^{(+-)} \bar{A}_1 \bar{A}_2 a_{(\ell+n)} \sin(b_{(\ell+n)} - \bar{B}_1 - \bar{B}_2) , \end{aligned} \quad (4.49)$$

and

$$\begin{aligned} \frac{2\omega_\ell a_\ell}{\epsilon^2} \frac{db_\ell}{dt} = & - \sum_{\bar{\omega}_1 + \bar{\omega}_2 = 2n} \left[ \Theta(n - \ell - d) \bar{R}_{(n-\ell-d)\ell}^{(-+)} \bar{A}_1 \bar{A}_2 a_{(n-\ell-d)} \cos(b_{(n-\ell-d)} - \bar{B}_1 - \bar{B}_2) \right]_{m^2=0} \\ & - \sum_{\bar{\omega}_1 + \bar{\omega}_2 = 2n} \Theta(\ell - n) \bar{R}_{(\ell-n)\ell}^{(++)} \bar{A}_1 \bar{A}_2 a_{(\ell-n)} \cos(b_{(\ell-n)} + \bar{B}_1 + \bar{B}_2) \\ & - \sum_{\bar{\omega}_1 + \bar{\omega}_2 = 2n} \bar{R}_{(\ell+n)\ell}^{(+-)} \bar{A}_1 \bar{A}_2 a_{(\ell+n)} \cos(b_{(\ell+n)} - \bar{B}_1 - \bar{B}_2) - \bar{T}_\ell \bar{A}_1 \bar{A}_2 a_\ell . \end{aligned} \quad (4.50)$$

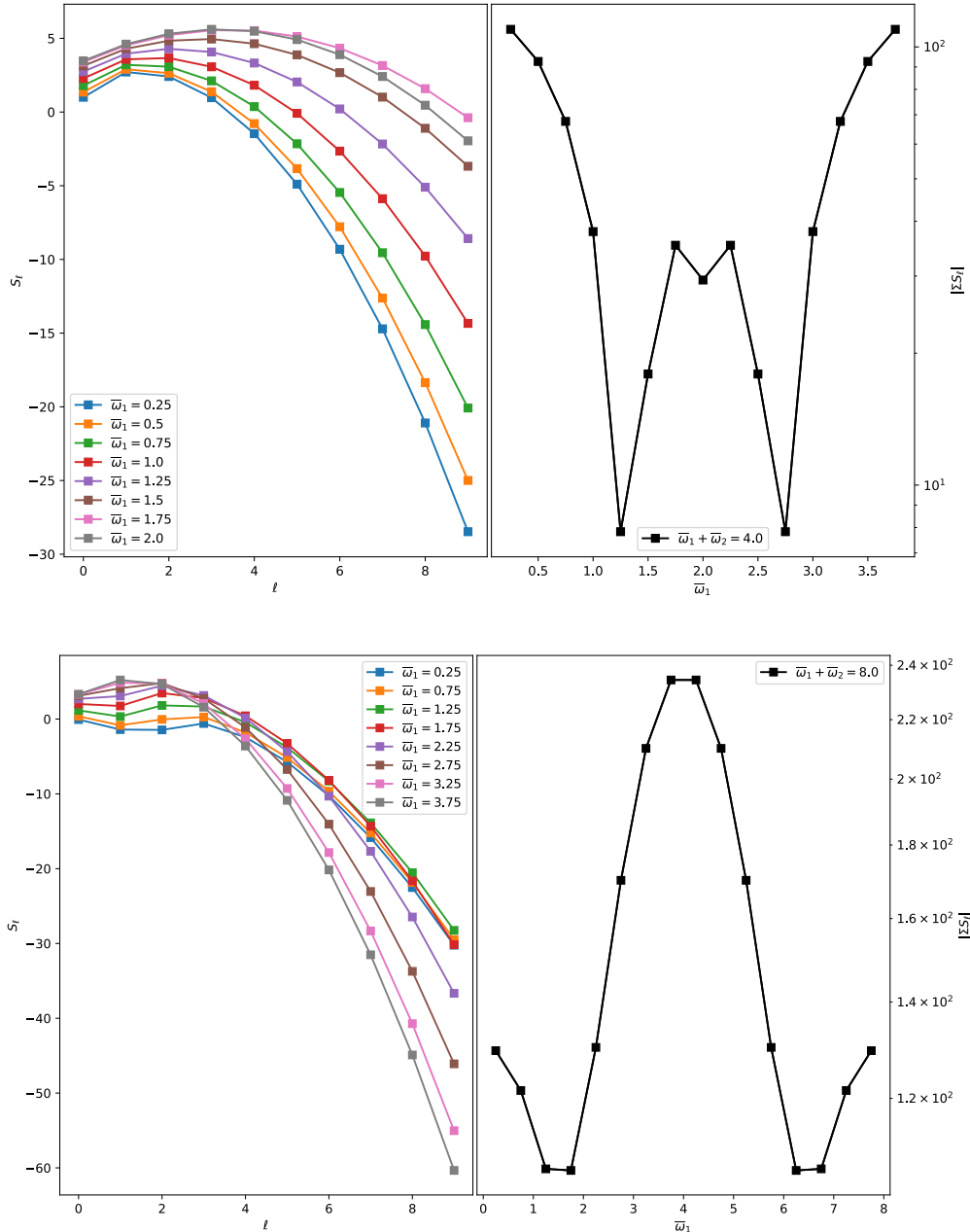


**Figure 4.5:** Above: The value of (4.44) as a function of  $\ell$  for a massless scalar with values of  $\bar{\omega}_1$  and  $\bar{\omega}_2$  chosen so that  $\bar{\omega}_1 + \bar{\omega}_2 = 4$ . Below: The same plot but with values chosen to satisfy  $\bar{\omega}_1 + \bar{\omega}_2 = 8$ .

#### 4.4.3 Integer Plus $\chi$

Finally, let us consider the case where the non-normalizable frequencies are non-integer, but differ from integer values by a set amount. In analogue to the case where all modes are normalizable, we

consider the non-normalizable frequencies to be shifted away from integer values by

$$\omega_\gamma = 2\gamma + \chi, \quad (4.51)$$

where  $\gamma \in \mathbb{Z}^+$  (greek letters are chosen to differentiate these non-normalizable modes from normalizable modes with integer frequencies, which use roman letters). We furthermore limit  $\chi$  to be non-integer<sup>10</sup> and set  $m^2 = 0$  throughout. For this choice of non-normalizable frequencies there are no resonant contributions from the all-plus channel, unlike the naturally vanishing resonance found in § 4.3.1. Only when either  $\omega_i + \omega_\gamma = \omega_\beta - \omega_\ell$ , or  $\omega_i + \omega_\gamma = \omega_\beta + \omega_\ell$  with  $i + \gamma \geq \ell$ , are resonant terms present. Let us examine each case separately.

#### 4.4.3.1 $\omega_i + \omega_\gamma = \omega_\beta - \omega_\ell$

When the resonance condition  $\omega_i + \omega_\gamma = \omega_\beta - \omega_\ell$  is met, the contribution to the source term is of the form

$$S_\ell = \sum_{i \neq \ell} \sum_{\gamma \neq \beta} \bar{S}_{i(\gamma+\ell)\gamma\ell}^{(1)} a_i \bar{A}_{(i+\gamma+\ell)} \bar{A}_\gamma \cos(\theta_i - \theta_{(i+\gamma+\ell)} + \theta_\gamma) + \sum_\beta \bar{R}_{\beta\ell}^{(1)} a_\ell \bar{A}_\beta^2 \cos(\theta_\ell + \theta_\beta - \theta_\beta) + \dots, \quad (4.52)$$

where

$$\begin{aligned} \bar{S}_{i\beta\gamma\ell}^{(1)} &= \frac{1}{4} H_{\beta\gamma i\ell} \frac{\omega_\gamma(\omega_i - \omega_\beta + 2\omega_\gamma)}{(\omega_\beta - \omega_\gamma)(\omega_i + \omega_\gamma)} - \frac{1}{4} H_{\gamma\beta i\ell} \frac{\omega_\beta(\omega_i + \omega_\gamma - 2\omega_\beta)}{(\omega_i - \omega_\beta)(\omega_\beta - \omega_\gamma)} - \frac{1}{4} H_{\gamma i\beta\ell} \frac{\omega_i(\omega_\gamma - \omega_\beta + 2\omega_i)}{(\omega_i - \omega_\beta)(\omega_i + \omega_\gamma)} \\ &+ \frac{1}{2} \omega_i \omega_\gamma X_{\beta\gamma i\ell} \left( \frac{\omega_\gamma}{\omega_i - \omega_\beta} - \frac{\omega_i}{\omega_\beta + \omega_\gamma} + 1 \right) + \frac{1}{2} \omega_i \omega_\beta X_{\gamma\beta i\ell} \left( \frac{\omega_i}{\omega_\beta - \omega_\gamma} + \frac{\omega_\beta}{\omega_i + \omega_\gamma} - 1 \right) \\ &+ \frac{1}{2} \omega_\beta \omega_\gamma X_{i\beta\gamma\ell} \left( \frac{\omega_\beta}{\omega_i + \omega_\gamma} - \frac{\omega_\gamma}{\omega_i - \omega_\beta} - 1 \right) - \frac{1}{4} Z_{\beta\gamma i\ell}^+ \left( \frac{\omega_i}{\omega_i + \omega_\ell} \right) \\ &+ \frac{1}{4} Z_{i\gamma\beta\ell}^- \left( \frac{\omega_\beta}{\omega_\ell - \omega_\beta} \right) + \frac{1}{4} Z_{i\beta\gamma\ell}^+ \left( \frac{\omega_\gamma}{\omega_\ell + \omega_\gamma} \right), \end{aligned} \quad (4.53)$$

---

<sup>10</sup>Indeed, for integer values of  $\chi$ , the sum or difference of two non-normalizable modes could be an integer. This would either be covered by the work in § 4.4.2.1, or be a slight variation of it.

and

$$\begin{aligned} \bar{R}_{\beta\ell}^{(1)} &= \frac{1}{4}Z_{\ell\beta\beta\ell}^-\left(\frac{\omega_\beta}{\omega_\ell + \omega_\beta}\right) + \frac{1}{4}Z_{\ell\beta\beta\ell}^+\left(\frac{\omega_\beta}{\omega_\ell - \omega_\beta}\right) + \frac{1}{2}H_{\ell\beta\beta\ell}\left(\frac{\omega_\beta^2}{\omega_\ell^2 - \omega_\beta^2}\right) - \frac{1}{2}H_{\beta\ell\beta\ell}\left(\frac{\omega_\ell^2}{\omega_\ell^2 - \omega_\beta^2}\right) \\ &+ X_{\beta\ell\beta\ell}\left(\frac{\omega_\ell^4}{\omega_\ell^2 - \omega_\beta^2}\right) - \frac{1}{2}\omega_\beta^2X_{\ell\beta\beta\ell}\left(\frac{\omega_\ell^2 + \omega_\beta^2}{\omega_\ell^2 - \omega_\beta^2}\right) - \frac{1}{2}H_{\ell\beta\beta\ell} + \omega_\ell^2\tilde{Z}_{\beta\beta\ell}^+ - 2\omega_\beta^2\omega_\ell^2P_{\ell\ell\beta} - \omega_\beta^2M_{\ell\ell\beta}. \end{aligned} \quad (4.54)$$

#### 4.4.3.2 $\omega_i + \omega_\gamma = \omega_\beta + \omega_\ell$

Similarly, when the resonance condition  $\omega_i + \omega_\gamma = \omega_\beta + \omega_\ell$  is met, the contribution to the source term is

$$\begin{aligned} S_\ell &= \underbrace{\sum_{i \neq \ell} \sum_{\gamma \neq \beta} \overline{S}_{i(i+\gamma-\ell)\gamma\ell}^{(2)} a_i \bar{A}_{(i+\gamma-\ell)} \bar{A}_\gamma \cos(\theta_i - \theta_{(i+\gamma-\ell)} + \theta_\gamma)}_{i+\gamma \geq \ell} \\ &+ \sum_\beta \bar{R}_{\beta\ell}^{(2)} a_\ell \bar{A}_\beta^2 \cos(\theta_\ell + \theta_\beta - \theta_\beta) + \dots, \end{aligned} \quad (4.55)$$

where

$$\begin{aligned} \overline{S}_{i\beta\gamma\ell}^{(2)} &= \frac{1}{4}H_{\beta\gamma i\ell}\frac{\omega_\gamma(\omega_i - \omega_\beta)}{(\omega_\beta - \omega_\gamma)(\omega_i - \omega_\gamma)} - \frac{1}{4}H_{\gamma\beta i\ell}\frac{\omega_\beta(\omega_\ell - \omega_\beta)}{(\omega_\beta - \omega_\gamma)(\omega_i - \omega_\beta)} + \frac{1}{4}H_{\beta i\gamma\ell}\frac{\omega_i(\omega_\gamma - \omega_\beta)}{(\omega_i - \omega_\beta)(\omega_i - \omega_\gamma)} \\ &+ \frac{1}{2}\omega_i\omega_\gamma X_{\beta\gamma i\ell}\left(\frac{\omega_\gamma}{\omega_i - \omega_\beta} - \frac{\omega_i}{\omega_\beta - \omega_\gamma} + 1\right) + \frac{1}{2}\omega_i\omega_\beta X_{\gamma\beta i\ell}\left(\frac{\omega_i}{\omega_\beta - \omega_\gamma} - \frac{\omega_\beta}{\omega_i - \omega_\gamma} - 1\right) \\ &+ \frac{1}{2}\omega_\beta\omega_\gamma X_{i\beta\gamma\ell}\left(\frac{\omega_\beta}{\omega_i - \omega_\gamma} - \frac{\omega_\gamma}{\omega_i - \omega_\beta} - 1\right) + \frac{1}{4}Z_{i\gamma\beta\ell}^-\left(\frac{\omega_\beta}{\omega_\ell + \omega_\beta}\right) \\ &+ \frac{1}{4}Z_{i\beta\gamma\ell}^+\left(\frac{\omega_\gamma}{\omega_\ell - \omega_\gamma}\right) - \frac{1}{4}Z_{\beta\gamma i\ell}^+\left(\frac{\omega_i}{\omega_i - \omega_\ell}\right), \end{aligned} \quad (4.56)$$

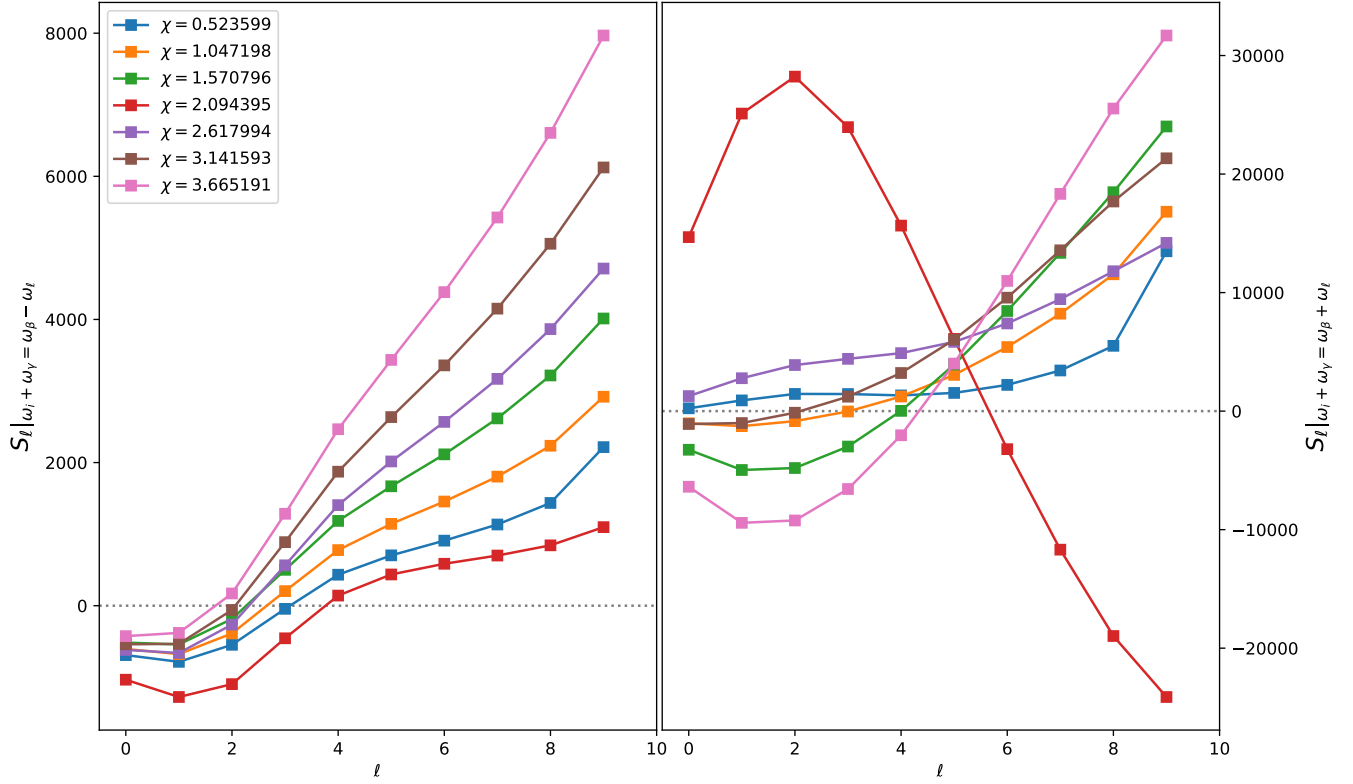


**Figure 4.6:** Left: Evaluating the source term (4.52) for various values of  $\chi$  for  $\ell < 10$ . Right: Evaluating the source term (4.55) subject to  $i + \gamma \geq \ell$  for the same values of  $\chi$  and the same range of  $\ell$ .

and

$$\begin{aligned} \bar{R}_{\beta\ell}^{(2)} = & \frac{1}{4}Z_{\ell\beta\beta\ell}^-\left(\frac{\omega_\beta}{\omega_\ell + \omega_\beta}\right) + \frac{1}{4}Z_{\ell\beta\beta\ell}^+\left(\frac{\omega_\beta}{\omega_\ell - \omega_\beta}\right) + \frac{1}{2}H_{\ell\beta\beta\ell}\left(\frac{\omega_\beta^2}{\omega_\ell^2 - \omega_\beta^2}\right) - \frac{1}{2}H_{\beta\ell\beta\ell}\left(\frac{\omega_\ell^2}{\omega_\ell^2 - \omega_\beta^2}\right) \\ & + X_{\beta\beta\ell\ell}\left(\frac{\omega_\ell^2}{\omega_\ell^2 - \omega_\beta^2}\right) + \frac{1}{2}\omega_\beta^2X_{\ell\beta\beta\ell}\left(\frac{\omega_\ell^2 + \omega_\beta^2}{\omega_\ell^2 - \omega_\beta^2}\right) - \frac{1}{2}H_{\beta\beta\ell\ell} + \omega_\ell^2\tilde{Z}_{\beta\beta\ell}^+ - 2\omega_\beta^2\omega_\ell^2P_{\ell\ell\beta} - \omega_\beta^2M_{\ell\ell\beta}. \end{aligned} \quad (4.57)$$

Unlike the case with all normalizable modes where two of the three resonance channels naturally vanished, both of the resonant channels contribute when the non-normalizable modes have frequencies given by (4.51). Therefore, the renormalization flow equations will contain contributions from

both channels:

$$\begin{aligned} \frac{2\omega_\ell}{\epsilon^2} \frac{da_\ell}{dt} = & - \sum_{i \neq \ell} \sum_{\gamma \neq \beta} \bar{S}_{i(i+\gamma+\ell)\gamma\ell}^{(1)} a_i \bar{A}_{(i+\gamma+\ell)} \bar{A}_\gamma \sin(b_\ell + \bar{B}_{(i+\gamma+\ell)} - b_i - \bar{B}_\gamma) \\ & - \underbrace{\sum_{i \neq \ell} \sum_{\gamma \neq \beta}}_{i+\gamma \geq \ell} \bar{S}_{i(i+\gamma-\ell)\gamma\ell}^{(2)} a_i \bar{A}_{(i+\gamma-\ell)} \bar{A}_\gamma \sin(b_\ell + \bar{B}_{(i+\gamma-\ell)} - b_i - \bar{B}_\gamma), \end{aligned} \quad (4.58)$$

$$\begin{aligned} \frac{2\omega_\ell a_\ell}{\epsilon^2} \frac{db_\ell}{dt} = & - \sum_{\beta} \bar{R}_{\beta\ell}^{(1)} a_\ell \bar{A}_\beta^2 - \sum_{\beta} \bar{R}_{\beta\ell}^{(2)} a_\ell \bar{A}_\beta^2 \\ & - \sum_{i \neq \ell} \sum_{\gamma \neq \beta} \bar{S}_{i(i+\gamma+\ell)\gamma\ell}^{(1)} a_i \bar{A}_{(i+\gamma+\ell)} \bar{A}_\gamma \cos(b_\ell + \bar{B}_{(i+\gamma+\ell)} - b_i - \bar{B}_\gamma) \\ & - \underbrace{\sum_{i \neq \ell} \sum_{\gamma \neq \beta}}_{i+\gamma \geq \ell} \bar{S}_{i(i+\gamma-\ell)\gamma\ell}^{(2)} a_i \bar{A}_{(i+\gamma-\ell)} \bar{A}_\gamma \cos(b_\ell + \bar{B}_{(i+\gamma-\ell)} - b_i - \bar{B}_\gamma). \end{aligned} \quad (4.59)$$

In figure 4.6, we evaluate both resonant contributions channels' and plot their contributions for various values of  $\chi$ . In particular, we examine the values  $\chi \in \{\pi/6, \dots, 7\pi/6\}$ . Again, there is no indication of any channel vanishing naturally. Interestingly, both sources demonstrate anomalous behaviour when  $\chi \sim 2$  for reasons that are not immediately clear. The source term (4.52) is generally more positive for larger  $\chi$  except for  $\chi = 2\pi/3$ , which is translated negatively with respect to the source terms produced by other  $\chi$  values. Again, when (4.55) is evaluated for  $\chi = 2\pi/3$ , the result differs significantly from other choices of  $\chi$ : seemingly reflected through the  $x$  axis with respect to other results. The significance of the choice  $\chi = 2\pi/3 \sim d/2$  is possibly explained by the non-normalizable modes being *nearly* equal to the normalizable ones. In this event,  $S_\ell$  would contain additional terms, such as those present in § 4.3. The departure of the  $\chi = 2\pi/3$  data from other data sets is perhaps a signal of these missing resonances.

## 4.5 Discussion

We have seen that the inclusion of a time-dependent boundary term in the holographic dual of a quantum quench allows energy to enter the bulk spacetime through coupling with non-normalizable modes. The dynamics of the weakly turbulent energy cascades that trigger instability were captured by secular terms at third-order that could not be removed by frequency shifts alone. Using the Two-Time Formalism, we have determined the renormalization group flow equations for the slowly varying amplitudes and phases that are tuned to cancel the secular terms that give rise to instability.

Unlike when only normalizable modes are considered, the introduction of non-normalizable modes results in no naturally vanishing resonance channels for the frequencies considered. The flow equations for  $a_\ell$  and  $b_\ell$  are now linear, since the non-normalizable amplitudes and phases are set by the first-order boundary condition and thus remain constant. In practice, this means the evolution of the system will be different than in the case where only normalizable modes are activated. Furthermore, periodic pumping of energy into and out of the bulk theory will undoubtably add interesting dynamics to the evolution already observed for quasi-periodic solutions with static boundary conditions [84].

With the renormalization flow equations established, future work will examine whether equilibrium solutions can be derived. Then, general non-collapsing solutions will be constructed and their evolution within the perturbative description will be examined. Comparisons to established numerical pumped solutions in the full theory may be instructive in understanding the space of stable and nearly-stable data.

Properties of the boundary CFT can also be determined from the perturbative theory in the bulk. For instance, the AdS/CFT dictionary relates the leading coefficient of the normalizable modes of the scalar field at the boundary to the expectation value of an operator  $\langle \mathcal{O}_\phi \rangle$ ; the leading part of the non-normalizable modes are related to a time-dependent driving term in the boundary Hamiltonian  $s(t)$ . The Ward identity for time translations gives the time dependence of the energy density in

the CFT in terms of these quantities, and allows us to examine the evolution of the energy density in boundary theory in terms of the leading contributions to bulk variables.

**Acknowledgments** The author would like to thank A. R. Frey for their guidance and insight with this project. This work is supported by the Natural Sciences and Engineering Research Council of Canada's Discovery Grant program.

# Appendix

## 4.A Derivation of Source Terms For Massive Scalars

The derivation of the general expression for the  $\mathcal{O}(\epsilon^3)$  source term for massive scalars closely follows the massless case, particularly if one chooses not to write out the explicit mass dependence as was done in [134]. However, since we have chosen to write our equations in a slightly different way – and in a different gauge – than previous authors, one may find it instructive to see the differences in the derivations. Below we have included the intermediate steps involved in deriving the third-order source term  $S_\ell$ .

Continuing the expansion of the equations of motion in powers of  $\epsilon$ , we see that the backreaction between the metric and the scalar field appears at second order in the perturbation,

$$A'_2 = -\mu\nu \left[ (\dot{\phi}_1)^2 + (\phi'_1)^2 + m^2\phi_1^2 \sec^2 x \right] + \nu' A_2/\nu, \quad (4.60)$$

which can be directly integrated to give

$$A_2 = -\nu \int_0^x dy \mu \left( (\dot{\phi}_1)^2 + (\phi'_1)^2 + m^2\phi_1^2 \sec^2 x \right). \quad (4.61)$$

For convenience, we have also defined the functions

$$\mu(x) = (\tan x)^{d-1} \quad \text{and} \quad \nu(x) = (d-1)/\mu'. \quad (4.62)$$

Similarly, the first non-trivial contribution to the lapse (in the boundary time gauge) is

$$\delta_2 = \int_x^{\pi/2} dy \mu \nu \left( (\dot{\phi}_1)^2 + (\phi'_1)^2 \right). \quad (4.63)$$

Projecting each of the terms in (4.14) individually onto the eigenbasis  $\{e_\ell\}$  will involve evaluating inner products involving multiple integrals. To aide in evaluating these expressions, it is useful to derive several identities. First, from the equation for the scalar field's time-dependent coefficients  $c_i$ ,

$$\ddot{c}_i + \omega_i^2 c_i = 0 \quad \Rightarrow \quad \partial_t (\dot{c}_i^2 + \omega_i^2 c_i^2) = \partial_t \mathbb{C}_i = 0. \quad (4.64)$$

Next, from the definition of  $\hat{L}$ ,

$$\hat{L} e_j = -\frac{1}{\mu} (\mu e'_j)' + m^2 \sec^2 x e_j \quad \Rightarrow \quad (\mu e'_j)' = \mu (m^2 \sec^2 x - \omega_j^2) e_j. \quad (4.65)$$

By considering the expression  $(\mu e'_i e_j)'$ , we see that

$$(\mu e'_i e_j)' = (m^2 \sec^2 x - \omega_i^2) \mu e_i e_j + \mu e'_i e'_j, \quad (4.66)$$

which, after permuting  $i, j$  and subtracting from above, gives

$$\frac{[\mu(e'_i e_j \omega_j^2 - e'_i e'_j \omega_i^2)]'}{(\omega_j^2 - \omega_i^2)} = \mu m^2 \sec^2 x e_i e_j + \mu e'_i e'_j. \quad (4.67)$$

Using these identities, we evaluate each of the inner products and find that

$$\begin{aligned} \langle \delta_2 \ddot{\phi}_1, e_\ell \rangle &= - \sum_{i=0}^{\infty} \sum_{j=0}^{\infty} \sum_{\substack{k=0 \\ k \neq \ell}}^{\infty} \frac{\omega_k^2 c_k}{\omega_\ell^2 - \omega_k^2} [\dot{c}_i \dot{c}_j (X_{k\ell ij} - X_{\ell kij}) + c_i c_j (Y_{ij\ell k} - Y_{ijk\ell})] \\ &\quad - \sum_{i=0}^{\infty} \sum_{j=0}^{\infty} \omega_\ell^2 c_\ell [\dot{c}_i \dot{c}_j P_{ij\ell} + c_i c_j B_{ij\ell}] , \end{aligned} \quad (4.68)$$

$$\begin{aligned} \langle A_2 \ddot{\phi}_1, e_\ell \rangle &= 2 \sum_{i=0}^{\infty} \sum_{j=0}^{\infty} \sum_{\substack{k=0 \\ i \neq j}}^{\infty} \frac{\omega_k^2 c_k}{\omega_j^2 - \omega_i^2} X_{ijk\ell} (\dot{c}_i \dot{c}_j + \omega_j^2 c_i c_j) \\ &\quad + \sum_{i=0}^{\infty} \sum_{j=0}^{\infty} \omega_j^2 c_j (\mathbb{C}_i P_{j\ell i} + c_i^2 X_{iij\ell}) , \end{aligned} \quad (4.69)$$

$$\begin{aligned} \langle \dot{\delta}_2 \dot{\phi}_1, e_\ell \rangle &= \sum_{i=0}^{\infty} \sum_{j=0}^{\infty} \sum_{\substack{k=0 \\ k \neq \ell}}^{\infty} \frac{\dot{c}_k}{\omega_\ell^2 - \omega_k^2} [\partial_t (\dot{c}_i \dot{c}_j) (X_{k\ell ij} - X_{\ell kij}) + \partial_t (c_i c_j) (Y_{ij\ell k} - Y_{ijk\ell})] \\ &\quad + \sum_{i=0}^{\infty} \sum_{j=0}^{\infty} \dot{c}_\ell [\partial_t (\dot{c}_i \dot{c}_j) P_{ij\ell} + \partial_t (c_i c_j) B_{ij\ell}] , \end{aligned} \quad (4.70)$$

$$\langle \dot{A}_2 \dot{\phi}_1, e_\ell \rangle = -2 \sum_{i=0}^{\infty} \sum_{j=0}^{\infty} \sum_{k=0}^{\infty} \dot{c}_k \dot{c}_j c_i X_{ijk\ell} , \quad (4.71)$$

$$\begin{aligned} \langle (A'_2 - \delta'_2) \phi'_1, e_\ell \rangle &= -2 \sum_{i=0}^{\infty} \sum_{j=0}^{\infty} \sum_{\substack{k=0 \\ i \neq j}}^{\infty} \frac{c_k (\dot{c}_i \dot{c}_j + \omega_j^2 c_i c_j)}{\omega_j^2 - \omega_i^2} H_{ijk\ell} - m^2 \sum_{i=0}^{\infty} \sum_{j=0}^{\infty} \sum_{k=0}^{\infty} c_i c_j c_k V_{ijk\ell} \\ &\quad - \sum_{i=0}^{\infty} \sum_{j=0}^{\infty} c_j [c_i^2 H_{iij\ell} + \mathbb{C}_i M_{j\ell i}] , \end{aligned} \quad (4.72)$$

$$\begin{aligned} \langle A_2 \phi_1 \sec^2 x, e_\ell \rangle &= -2 \sum_{i=0}^{\infty} \sum_{j=0}^{\infty} \sum_{\substack{k=0 \\ i \neq j}}^{\infty} \frac{c_k (\dot{c}_i \dot{c}_j + \omega_j^2 c_i c_j)}{\omega_j^2 - \omega_i^2} V_{jki\ell} \\ &\quad - \sum_{i=0}^{\infty} \sum_{j=0}^{\infty} c_j (c_i^2 V_{jiil} + \mathbb{C}_i Q_{j\ell i}) , \end{aligned} \quad (4.73)$$

where the forms of X, Y, V, H, B, M, P, and Q are given by

$$X_{ijkl} = \int_0^{\pi/2} dx \mu^2 \nu e'_i e'_j e'_k e'_\ell \quad (4.74)$$

$$Y_{ijkl} = \int_0^{\pi/2} dx \mu^2 \nu e'_i e'_j e'_k e'_\ell \quad (4.75)$$

$$V_{ijkl} = \int_0^{\pi/2} dx \mu^2 \nu e_i e_j e'_k e_\ell \sec^2 x \quad (4.76)$$

$$H_{ijkl} = \int_0^{\pi/2} dx \mu^2 \nu' e'_i e'_j e'_k e'_\ell \quad (4.77)$$

$$B_{ij\ell} = \int_0^{\pi/2} dx \mu \nu e'_i e'_j \int_0^x dy \mu e_\ell^2 \quad (4.78)$$

$$M_{ij\ell} = \int_0^{\pi/2} dx \mu \nu' e'_i e_j \int_0^x dy \mu e_\ell^2 \quad (4.79)$$

$$P_{ij\ell} = \int_0^{\pi/2} dx \mu \nu e_i e_j \int_0^x dy \mu e_\ell^2 \quad (4.80)$$

$$Q_{ij\ell} = \int_0^{\pi/2} dx \mu \nu e_i e_j \sec^2 x \int_0^x dy \mu e_\ell^2. \quad (4.81)$$

Note that, using integration by parts to remove the derivative from  $\nu$  in the definitions of  $H_{ijkl}$  and  $M_{ij\ell}$ , we can show that

$$H_{ijkl} = \omega_i^2 X_{kij\ell} + \omega_k^2 X_{ijkl} - Y_{ij\ell k} - Y_{\ell kji} - m^2 V_{kji\ell} - m^2 V_{ijkl}, \quad (4.82)$$

$$M_{ij\ell} = \omega_i^2 P_{ij\ell} - B_{ij\ell} - m^2 Q_{ij\ell}. \quad (4.83)$$

Collecting (4.68) - (4.73) gives the expression for  $S_\ell = \langle S, e_\ell \rangle$ :

$$\begin{aligned}
S_\ell &= \sum_{\substack{i,j,k \\ k \neq \ell}}^{\infty} \frac{1}{\omega_\ell^2 - \omega_k^2} \left[ F_k(\dot{c}_i \dot{c}_j) (X_{k\ell ij} - X_{\ell kij}) + F_k(c_i c_j) (Y_{ij\ell k} - Y_{ijk\ell}) \right] \\
&\quad + 2 \sum_{\substack{i,j,k \\ i \neq j}}^{\infty} \frac{c_k D_{ij}}{\omega_j^2 - \omega_i^2} \left[ 2\omega_k^2 X_{ijkl} - H_{ijkl} - m^2 V_{jkil} \right] - \sum_{i,j,k}^{\infty} c_i \left[ 2\dot{c}_j \dot{c}_k X_{ijkl} + m^2 c_j c_k V_{ijkl} \right] \\
&\quad + \sum_{i,j}^{\infty} \left[ F_\ell(\dot{c}_i \dot{c}_j) P_{ij\ell} + F_\ell(c_i c_j) B_{ij\ell} + 2\omega_j^2 c_j (c_i^2 X_{iij\ell} + \mathbb{C}_i P_{j\ell i}) \right. \\
&\quad \left. - c_j (c_i^2 (H_{iij\ell} + m^2 V_{jiil}) + \mathbb{C}_i (M_{j\ell i} + m^2 Q_{j\ell i})) \right], \tag{4.84}
\end{aligned}$$

where  $F_k(z) = \dot{c}_k \dot{z} - 2\omega_k^2 c_k z$ ,  $D_{ij} = \dot{c}_i \dot{c}_j + \omega_j^2 c_i c_j$ , and  $\mathbb{C}_i = \dot{c}_i^2 + \omega_i^2 c_i^2$ . Additionally, we have combined some integrals into their own expressions, namely

$$Z_{ijkl}^\pm = \omega_i \omega_j (X_{k\ell ij} - X_{\ell kij}) \pm (Y_{ij\ell k} - Y_{ijk\ell}) \quad \text{and} \quad \tilde{Z}_{ij\ell}^\pm = \omega_i \omega_j P_{ij\ell} \pm B_{ij\ell}. \tag{4.85}$$

Finally, using the solution for the time-dependent coefficients,  $c_i(t) = a_i(t) \cos(\omega_i t + b_i(t)) \equiv a_i \cos \theta_i$ , we arrive at (4.15).

## 4.B Two Non-normalizable Modes with Equal Frequencies

Let us return to the case of two, equal, non-normalizable modes with frequency  $\bar{\omega}$ . Within the space of resonant frequency values, there are frequencies that happen to satisfy  $\bar{\omega} = \omega_\ell$  numerically and may produce extra resonances subject to restrictions on the normalizable frequency. These instances were excluded from the discussion in § 4.4.1, and we address them here. When considering special

integer values of  $\bar{\omega}$  each choice of  $\bar{\omega}$  below will contribute a  $\bar{T}$ -type term to the total source:

$$\bar{T}_i^{(1)} : \quad \omega_i = \omega_\ell + 2\bar{\omega} \quad \forall \bar{\omega} \in \mathbb{Z}^+ \quad (4.86)$$

$$\bar{T}_i^{(2)} : \quad \omega_i = \omega_\ell - 2\bar{\omega} \quad \forall \bar{\omega} \in \mathbb{Z}^+ \text{ such that } \ell \geq \bar{\omega} \quad (4.87)$$

$$\bar{T}_i^{(3)} : \quad \omega_i = 2\bar{\omega} - \omega_\ell \quad \forall \bar{\omega} \in \mathbb{Z}^+ \text{ such that } \bar{\omega} \leq \ell + \Delta^+, \quad (4.88)$$

with  $\omega_i \neq \omega_\ell$  in each case. These special values contribute to the case of two, equal non-normalizable modes via

$$\begin{aligned} S_\ell = & \bar{A}_{\bar{\omega}}^2 \bar{T}_{(\ell+\bar{\omega})}^{(1)} a_{(\ell+\bar{\omega})} \cos(\theta_{(\ell+\bar{\omega})} - 2\bar{\omega}t) + \bar{A}_{\bar{\omega}}^2 \bar{T}_{(\ell-\bar{\omega})}^{(2)} a_{(\ell-\bar{\omega})} \cos(\theta_{(\ell-\bar{\omega})} + 2\bar{\omega}t) \\ & + \bar{A}_{\bar{\omega}}^2 \bar{T}_{(\bar{\omega}-\ell-\Delta^+)}^{(3)} a_{(\bar{\omega}-\ell-\Delta^+)} \cos(2\bar{\omega}t - \theta_{(\bar{\omega}-\ell-\Delta^+)}) \end{aligned} \quad (4.89)$$

under their respective conditions on the value of  $\bar{\omega}$ . The total resonant contribution for all possible  $\bar{\omega}$  values is the addition of (4.89) and (4.38). Evaluating (4.15) in each case of the cases described by (4.86) - (4.88), we find that

$$\begin{aligned} \bar{T}_i^{(1)} = & \frac{1}{2} \left[ H_{i\bar{\omega}\bar{\omega}\ell} \left( \frac{\bar{\omega}}{\omega_i - \bar{\omega}} \right) - H_{\bar{\omega}i\bar{\omega}\ell} \left( \frac{\omega_i}{\omega_i - \bar{\omega}} \right) + m^2 V_{\bar{\omega}\bar{\omega}i\ell} \left( \frac{\bar{\omega}}{\omega_i - \bar{\omega}} \right) \right. \\ & \left. - m^2 V_{i\bar{\omega}\bar{\omega}\ell} \left( \frac{\omega_i}{\omega_i - \bar{\omega}} \right) - 2\bar{\omega}^2 X_{i\bar{\omega}\bar{\omega}\ell} \left( \frac{\bar{\omega}}{\omega_i - \bar{\omega}} \right) + 2\bar{\omega}^2 X_{\bar{\omega}i\bar{\omega}\ell} \left( \frac{\omega_i}{\omega_i - \bar{\omega}} \right) \right]_{\omega_i \neq \bar{\omega}} \\ & - \frac{1}{2} \left[ Z_{i\bar{\omega}\bar{\omega}\ell}^+ \left( \frac{\bar{\omega}}{\omega_\ell + \bar{\omega}} \right) \right]_{\omega_\ell \neq \bar{\omega}} + \frac{1}{4} Z_{\bar{\omega}\bar{\omega}i\ell}^- \left( \frac{\omega_\ell + 2\bar{\omega}}{2\bar{\omega}} \right) + \frac{1}{2} \bar{\omega}^2 X_{i\bar{\omega}\bar{\omega}\ell} - \frac{m^2}{4} V_{\bar{\omega}\bar{\omega}i\ell} \\ & - \bar{\omega} \omega_i X_{\bar{\omega}\bar{\omega}i\ell} - \frac{m^2}{2} V_{i\bar{\omega}\bar{\omega}\ell}, \end{aligned} \quad (4.90)$$

$$\begin{aligned}
\bar{T}_i^{(2)} = & -\frac{1}{2} \left[ H_{i\bar{\omega}\omega\ell} \left( \frac{\bar{\omega}}{\omega_i + \bar{\omega}} \right) + H_{\bar{\omega}i\bar{\omega}\ell} \left( \frac{\omega_i}{\omega_i + \bar{\omega}} \right) + m^2 V_{\bar{\omega}\bar{\omega}i\ell} \left( \frac{\bar{\omega}}{\omega_i + \bar{\omega}} \right) \right. \\
& + m^2 V_{i\bar{\omega}\omega\ell} \left( \frac{\omega_i}{\omega_i + \bar{\omega}} \right) - 2\bar{\omega}^2 X_{i\bar{\omega}\omega\ell} \left( \frac{\bar{\omega}}{\omega_i + \bar{\omega}} \right) - 2\bar{\omega}^2 X_{\bar{\omega}\bar{\omega}i\ell} \left( \frac{\omega_i}{\omega_i + \bar{\omega}} \right) \Big]_{\omega_i \neq \bar{\omega}} \\
& - \frac{1}{2} \left[ Z_{i\bar{\omega}\omega\ell}^- \left( \frac{\bar{\omega}}{\omega_\ell - \bar{\omega}} \right) \right]_{\omega_\ell \neq \bar{\omega}} - \frac{1}{4} Z_{\bar{\omega}\bar{\omega}i\ell}^- \left( \frac{\omega_\ell - 2\bar{\omega}}{\bar{\omega}} \right) + \frac{1}{2} \bar{\omega}^2 X_{i\bar{\omega}\omega\ell} + \frac{m^2}{4} V_{\bar{\omega}\bar{\omega}i\ell} \\
& + \bar{\omega} \omega_i X_{\bar{\omega}\bar{\omega}i\ell} + \frac{m^2}{2} V_{i\bar{\omega}\omega\ell}, 
\end{aligned} \tag{4.91}$$

and

$$\begin{aligned}
\bar{T}_i^{(3)} = & \frac{1}{2} \left[ H_{i\bar{\omega}\omega\ell} \left( \frac{\bar{\omega}}{\omega_i - \bar{\omega}} \right) - H_{\bar{\omega}i\bar{\omega}\ell} \left( \frac{\omega_i}{\omega_i - \bar{\omega}} \right) + m^2 V_{\bar{\omega}\bar{\omega}i\ell} \left( \frac{\bar{\omega}}{\omega_i - \bar{\omega}} \right) \right. \\
& - m^2 V_{i\bar{\omega}\omega\ell} \left( \frac{\omega_i}{\omega_i - \bar{\omega}} \right) - 2\bar{\omega}^2 X_{i\bar{\omega}\omega\ell} \left( \frac{\bar{\omega}}{\omega_i - \bar{\omega}} \right) + 2\omega_i^2 X_{\bar{\omega}\bar{\omega}i\ell} \left( \frac{\bar{\omega}}{\omega_i - \bar{\omega}} \right) \\
& - Z_{i\bar{\omega}\omega\ell}^+ \left( \frac{\bar{\omega}}{\omega_i - \bar{\omega}} \right) \Big]_{\omega_i \neq \bar{\omega}} + \frac{1}{4} Z_{\bar{\omega}\bar{\omega}i\ell}^- \left( \frac{2\bar{\omega} - \omega_\ell}{2\bar{\omega}} \right) + \frac{1}{2} \bar{\omega}^2 X_{i\bar{\omega}\omega\ell} - \frac{m^2}{4} V_{\bar{\omega}\bar{\omega}i\ell} \\
& - \bar{\omega} \omega_i X_{\bar{\omega}\bar{\omega}i\ell} - \frac{m^2}{2} V_{i\bar{\omega}\omega\ell}.
\end{aligned} \tag{4.92}$$

These resonance channels can then be added into the right hand side of the equation for  $da_\ell/dt$  in (4.40).

## 5 Conclusion

In this thesis, we have addressed several facets of scalar field collapse in Anti-de Sitter spacetime as it relates to dynamical processes in strongly-coupled gauge theories. By considering a wide range of Gaussian initial data in  $\text{AdS}_5$  in the nonperturbative (but small amplitude) regime, we have mapped out the islands of stability for a real scalar of mass  $\mu$  and width  $\sigma$ . In addition to stable and unstable data, we have uncovered two new classes: those that exhibit metastability at finite amplitudes and scale like  $t_H \propto \epsilon^{-p}$  for  $p > 2$ , and those that have non-monotonically increasing horizon formation times with decreasing amplitude. There is evidence for weakly chaotic evolution of data within the latter class, even for massless scalars. The root of the chaotic behaviour is yet to be determined, however there are indications that self-interaction occurs between regions of increased density produced by gravitational focusing. While similar chaotic evolutions have been observed between thin shells of infalling matter, this is the first time it has been observed in continuous initial data without higher-derivative couplings in the action. To determine the ultimate fate of irregular and metastable data in the nonlinear theory as  $\epsilon \rightarrow 0$ , greater computing power is required; however, this is exactly the regime where the perturbative theory is applicable. Therefore, future progress may be made by a combination of perturbative and nonlinear evolutions.

Next, we examined perturbatively stable solutions through the Two-Time Formalism. Using renormalization flow methods, the secular growth of resonant contributions was absorbed into amplitude and phase variables so that the (massless) scalar field remained stable over perturbative timescales of  $t \sim \epsilon^{-2}$ . By introducing a quasi-periodic ansatz for the renormalized amplitudes, we found numerical solutions to the truncated system characterized by the ratio of conserved quantities in the theory,  $T = E/N$ . These solutions were tested for robustness against the choice of truncation value

for different values of  $T$ . At this time, our results remain in tension with those in the literature, as we were unable to verify the entire range of proposed solutions.

Since the islands of stability seem to be “anchored” near single-mode data, and since the TTF description of the scalar field is a sum single modes weighted by time-dependent coefficients, it is natural to consider whether all data within the islands of stability could be written in terms of quasi-periodic TTF solutions. Any reduction in the space of QP solutions, such as a threshold temperature  $T_{th}$ , would make this description less likely. Future work may include examining the metastable and irregular data from nonlinear theory in the perturbative framework to see if existing QP families of solutions can describe these initial conditions.

Ideally, scalar fields with amplitudes  $\epsilon$  could be evolved with less computational cost using the TTF framework over perturbative timescales, switching over to nonlinear evolution only when required. However, predicting a value for when the perturbative theory begins to break down is not possible, since we only know that the perturbative theory is valid when  $\epsilon^2 t \sim 1$ . An important future contribution to the understanding of both the nonlinear and perturbative description of scalar field collapse would be to compare the evolutions in either scheme to establish some time scale for the applicability of the TTF.

Finally, we extended the TTF description to include massive scalars, as well as time dependent boundary conditions. We saw that some of the symmetries that lead to the natural vanishing of two of the three resonance channels were broken by the presence of mass-dependent terms. In such cases, the renormalized amplitude and phase equations include contributions from multiple resonance channels. The inclusion of non-zero boundary terms requires the activation of non-normalizable modes. We explicitly calculated the  $\mathcal{O}(\epsilon^3)$  source term for several choices of non-normalizable frequencies, which – unlike normalizable modes – are not constrained to be fully integer. Because energy enters the bulk through the boundary term, the evolution of such pumped systems will differ qualitatively from adiabatic evolution. The focus of future work will be constructing equilibrium solutions and analyzing their evolution. Like the more familiar massless scalars, there must exist inverse energy cascades to balance the transfer of energy to short length scales, thereby providing

stability against collapse. This has yet to be addressed in the literature.

As research continues into the stability of Anti-de Sitter space, we will develop a better understanding not only of gravitational collapse, but also of dynamical processes in the strongly-coupled regimes of the dual theories. We have seen that even the simplest case, that of a minimally-coupled scalar field, has uncovered a surprising breadth of phenomena. Constructing a holographic dual to a realistic system, such as the high energy collision of heavy ions, introduces myriad complexities that may produce even more intriguing results. With each new discovery, we will gain a greater appreciation for curious relationship between gauge theories and higher-dimensional gravity.

# Bibliography

- [1] J. M. Maldacena, *The Large  $N$  limit of superconformal field theories and supergravity*, *Int. J. Theor. Phys.* **38** (1999) 1113–1133, [[hep-th/9711200](#)].
- [2] G. T. Horowitz and J. Polchinski, *Gauge/gravity duality*, [gr-qc/0602037](#).
- [3] G. 't Hooft, *Dimensional reduction in quantum gravity*, *Conf. Proc. C930308* (1993) 284–296, [[gr-qc/9310026](#)].
- [4] L. Susskind, *The World as a hologram*, *J. Math. Phys.* **36** (1995) 6377–6396, [[hep-th/9409089](#)].
- [5] J. L. Petersen, *Introduction to the Maldacena conjecture on  $AdS / CFT$* , *Int. J. Mod. Phys. A14* (1999) 3597–3672, [[hep-th/9902131](#)].
- [6] O. Aharony, S. S. Gubser, J. M. Maldacena, H. Ooguri and Y. Oz, *Large  $N$  field theories, string theory and gravity*, *Phys. Rept.* **323** (2000) 183–386, [[hep-th/9905111](#)].
- [7] B. Zwiebach, *A First Course in String Theory*. Cambridge University Press, Cambridge, UK, 2nd ed., 2009.
- [8] J. Polchinski, *String theory. Vol. 2: Superstring theory and beyond*. Cambridge Monographs on Mathematical Physics. Cambridge University Press, 2007, [10.1017/CBO9780511618123](#).
- [9] S. A. Hartnoll, A. Lucas and S. Sachdev, *Holographic quantum matter*, [1612.07324](#).
- [10] V. E. Hubeny, *The  $AdS/CFT$  Correspondence*, *Class. Quant. Grav.* **32** (2015) 124010, [[1501.00007](#)].

- [11] I. R. Klebanov and E. Witten, *AdS / CFT correspondence and symmetry breaking*, *Nucl. Phys.* **B556** (1999) 89–114, [[hep-th/9905104](#)].
- [12] J. M. Maldacena, *Wilson loops in large N field theories*, *Phys. Rev. Lett.* **80** (1998) 4859–4862, [[hep-th/9803002](#)].
- [13] S. Ryu and T. Takayanagi, *Holographic derivation of entanglement entropy from AdS/CFT*, *Phys. Rev. Lett.* **96** (2006) 181602, [[hep-th/0603001](#)].
- [14] A. Lewkowycz and J. Maldacena, *Generalized gravitational entropy*, *JHEP* **08** (2013) 090, [[1304.4926](#)].
- [15] S. S. Gubser, I. R. Klebanov and A. M. Polyakov, *Gauge theory correlators from noncritical string theory*, *Phys. Lett.* **B428** (1998) 105–114, [[hep-th/9802109](#)].
- [16] E. Witten, *Anti-de Sitter space and holography*, *Adv. Theor. Math. Phys.* **2** (1998) 253–291, [[hep-th/9802150](#)].
- [17] J. D. Bekenstein, *Black holes and entropy*, *Phys. Rev.* **D7** (1973) 2333–2346.
- [18] T. Jacobson, *Introductory lectures on black hole thermodynamics*, 1996.
- [19] J. M. Bardeen, B. Carter and S. W. Hawking, *The Four laws of black hole mechanics*, *Commun. Math. Phys.* **31** (1973) 161–170.
- [20] A. Bernamonti, F. Galli, R. C. Myers and J. Oppenheim, *Holographic second laws of black hole thermodynamics*, *JHEP* **07** (2018) 111, [[1803.03633](#)].
- [21] S. W. Hawking, *Black hole explosions*, *Nature* **248** (1974) 30–31.
- [22] S. W. Hawking, *Particle Creation by Black Holes*, *Commun. Math. Phys.* **43** (1975) 199–220.
- [23] S. M. Carroll, *Spacetime and geometry: An introduction to general relativity*. Addison-Wesley, 2004.
- [24] S. W. Hawking and D. N. Page, *Thermodynamics of Black Holes in Anti-de Sitter Space*, *Commun. Math. Phys.* **87** (1983) 577.

- [25] A. N. Schellekens, *Conformal Field Theory*, 2016.
- [26] E. Witten, *Anti-de Sitter space, thermal phase transition, and confinement in gauge theories*, *Adv. Theor. Math. Phys.* **2** (1998) 505–532, [[hep-th/9803131](#)].
- [27] J. Casalderrey-Solana, H. Liu, D. Mateos, K. Rajagopal and U. A. Wiedemann, *Gauge/String Duality, Hot QCD and Heavy Ion Collisions*, [1101.0618](#).
- [28] V. Balasubramanian, A. Bernamonti, J. de Boer, N. Copland, B. Craps, E. Keski-Vakkuri et al., *Holographic Thermalization*, *Phys. Rev.* **D84** (2011) 026010, [[1103.2683](#)].
- [29] V. E. Hubeny, M. Rangamani and T. Takayanagi, *A Covariant holographic entanglement entropy proposal*, *JHEP* **07** (2007) 062, [[0705.0016](#)].
- [30] A. Buchel, R. C. Myers and A. van Niekerk, *Nonlocal probes of thermalization in holographic quenches with spectral methods*, *JHEP* **02** (2015) 017, [[1410.6201](#)].
- [31] E. da Silva, E. Lopez, J. Mas and A. Serantes, *Collapse and Revival in Holographic Quenches*, *JHEP* **04** (2015) 038, [[1412.6002](#)].
- [32] J. Dziarmaga, *Dynamics of a quantum phase transition and relaxation to a steady state*, *Advances in Physics* **59** (2010) 1063–1189,  
[\[http://dx.doi.org/10.1080/00018732.2010.514702\]](http://dx.doi.org/10.1080/00018732.2010.514702).
- [33] A. Lamacraft and J. Moore, *Potential insights into non-equilibrium behavior from atomic physics*, *ArXiv e-prints* (jun, 2011) , [[1106.3567](#)].
- [34] P. Bosch, A. Buchel and L. Lehner, *Unstable horizons and singularity development in holography*, [1704.05454](#).
- [35] P. Mikula, M. E. Carrington and G. Kunstatter, *Nonequilibrium approach to holographic superconductors using gradient flow*, *Phys. Rev.* **D100** (2019) 046004, [[1902.08669](#)].
- [36] D. Poland, S. Rychkov and A. Vichi, *The Conformal Bootstrap: Theory, Numerical Techniques, and Applications*, *Rev. Mod. Phys.* **91** (2019) 015002, [[1805.04405](#)].

- [37] P. Breitenlohner and D. Z. Freedman, *Positive Energy in Anti-de Sitter Backgrounds and Gauged Extended Supergravity*, *Phys. Lett.* **B115** (1982) 197–201.
- [38] D. Tong, *String Theory*, [0908.0333](#).
- [39] N. Deppe and A. R. Frey, *Classes of Stable Initial Data for Massless and Massive Scalars in Anti-de Sitter Spacetime*, *JHEP* **12** (2015) 004, [[1508.02709](#)].
- [40] G. Kunstatter, H. Maeda and T. Taves, *Hamiltonian dynamics of Lovelock black holes with spherical symmetry*, *Class. Quant. Grav.* **30** (2013) 065002, [[1210.1566](#)].
- [41] V. Balasubramanian, A. Buchel, S. R. Green, L. Lehner and S. L. Liebling, *Reply to Comment on “Holographic Thermalization, Stability of Anti-de Sitter Space, and the Fermi-Pasta-Ulam Paradox”*, *Phys. Rev. Lett.* **115** (2015) 049102, [[1506.07907](#)].
- [42] B. Craps, O. Evnin and J. Vanhoof, *Renormalization group, secular term resummation and AdS (in)stability*, *JHEP* **10** (2014) 048, [[1407.6273](#)].
- [43] L.-Y. Chen, N. Goldenfeld and Y. Oono, *The Renormalization group and singular perturbations: Multiple scales, boundary layers and reductive perturbation theory*, *Phys. Rev. E* **54** (1996) 376–394, [[hep-th/9506161](#)].
- [44] V. Balasubramanian, A. Buchel, S. R. Green, L. Lehner and S. L. Liebling, *Holographic Thermalization, Stability of Anti-de Sitter Space, and the Fermi-Pasta-Ulam Paradox*, *Phys. Rev. Lett.* **113** (2014) 071601, [[1403.6471](#)].
- [45] T. Hertog and G. T. Horowitz, *Towards a big crunch dual*, *JHEP* **07** (2004) 073, [[hep-th/0406134](#)].
- [46] Y. Brihaye, B. Hartmann and S. Tojiev, *Stability of charged solitons and formation of boson stars in 5-dimensional Anti-de Sitter space-time*, *Class. Quant. Grav.* **30** (2013) 115009, [[1301.2452](#)].
- [47] E. J. Copeland, M. Gleiser and H. R. Muller, *Oscillons: Resonant configurations during bubble collapse*, *Phys. Rev.* **D52** (1995) 1920–1933, [[hep-ph/9503217](#)].

- [48] O. J. C. Dias, J. E. Santos and B. Way, *Numerical Methods for Finding Stationary Gravitational Solutions*, *Class. Quant. Grav.* **33** (2016) 133001, [[1510.02804](#)].
- [49] O. J. C. Dias, G. T. Horowitz, D. Marolf and J. E. Santos, *On the Nonlinear Stability of Asymptotically Anti-de Sitter Solutions*, *Class. Quant. Grav.* **29** (2012) 235019, [[1208.5772](#)].
- [50] G. Fodor, P. Forgács and P. Grandclément, *Self-gravitating scalar breathers with negative cosmological constant*, *Phys. Rev.* **D92** (2015) 025036, [[1503.07746](#)].
- [51] D. Astefanesei and E. Radu, *Boson stars with negative cosmological constant*, *Nucl. Phys.* **B665** (2003) 594–622, [[gr-qc/0309131](#)].
- [52] A. Buchel, S. L. Liebling and L. Lehner, *Boson stars in AdS spacetime*, *Phys. Rev.* **D87** (2013) 123006, [[1304.4166](#)].
- [53] S. Hu, J. T. Liu and L. A. Pando Zayas, *Charged Boson Stars in AdS and a Zero Temperature Phase Transition*, [1209.2378](#).
- [54] M. Choptuik, R. Masachs and B. Way, *Multioscillating Boson Stars*, *Phys. Rev. Lett.* **123** (2019) 131101, [[1904.02168](#)].
- [55] M. Bañados, C. Teitelboim and J. Zanelli, *The Black hole in three-dimensional space-time*, *Phys. Rev. Lett.* **69** (1992) 1849–1851, [[hep-th/9204099](#)].
- [56] F. Pretorius and M. W. Choptuik, *Gravitational collapse in (2+1)-dimensional AdS space-time*, *Phys. Rev.* **D62** (2000) 124012, [[gr-qc/0007008](#)].
- [57] V. Husain and M. Olivier, *Scalar field collapse in three-dimensional AdS space-time*, *Class. Quant. Grav.* **18** (2001) L1–L10, [[gr-qc/0008060](#)].
- [58] M. Maliborski and A. Rostworowski, *Time-Periodic Solutions in an Einstein AdS-Massless-Scalar-Field System*, *Phys. Rev. Lett.* **111** (2013) 051102, [[1303.3186](#)].
- [59] P. Basu, D. Das, S. R. Das and T. Nishioka, *Quantum Quench Across a Zero Temperature Holographic Superfluid Transition*, *JHEP* **03** (2013) 146, [[1211.7076](#)].

- [60] P. Bizoń and J. Jałmużna, *Globally regular instability of  $AdS_3$* , *Phys. Rev. Lett.* **111** (2013) 041102, [[1306.0317](#)].
- [61] M. W. Choptuik, *Universality and scaling in gravitational collapse of a massless scalar field*, *Phys. Rev. Lett.* **70** (1993) 9–12.
- [62] C. Gundlach, *Critical phenomena in gravitational collapse*, *Phys. Rept.* **376** (2003) 339–405, [[gr-qc/0210101](#)].
- [63] M. Maliborski, *Instability of Flat Space Enclosed in a Cavity*, *Phys. Rev. Lett.* **109** (2012) 221101, [[1208.2934](#)].
- [64] A. Buchel, L. Lehner and S. L. Liebling, *Scalar Collapse in  $AdS$* , *Phys. Rev.* **D86** (2012) 123011, [[1210.0890](#)].
- [65] G. Clement and A. Fabbri, *Critical collapse in (2+1)-dimensional  $AdS$  space-time: Quasi CSS solutions and linear perturbations*, *Nucl. Phys.* **B630** (2002) 269–292, [[gr-qc/0109002](#)].
- [66] D. Birmingham, *Choptuik scaling and quasinormal modes in the  $AdS$  / CFT correspondence*, *Phys. Rev.* **D64** (2001) 064024, [[hep-th/0101194](#)].
- [67] P. Bizoń and A. Rostworowski, *On weakly turbulent instability of anti-de Sitter space*, *Phys. Rev. Lett.* **107** (2011) 031102, [[1104.3702](#)].
- [68] D. Garfinkle and L. A. Pando Zayas, *Rapid Thermalization in Field Theory from Gravitational Collapse*, *Phys. Rev.* **D84** (2011) 066006, [[1106.2339](#)].
- [69] J. Jałmużna, A. Rostworowski and P. Bizoń, *A Comment on  $AdS$  collapse of a scalar field in higher dimensions*, *Phys. Rev.* **D84** (2011) 085021, [[1108.4539](#)].
- [70] D. Garfinkle, L. A. Pando Zayas and D. Reichmann, *On Field Theory Thermalization from Gravitational Collapse*, *JHEP* **02** (2012) 119, [[1110.5823](#)].
- [71] D. Garfinkle and C. Gundlach, *Perturbations of an exact solution for (2+1)-dimensional critical collapse*, *Phys. Rev.* **D66** (2002) 044015, [[gr-qc/0205107](#)].

- [72] D. Garfinkle, *An Exact solution for 2+1 dimensional critical collapse*, *Phys. Rev.* **D63** (2001) 044007, [[gr-qc/0008023](#)].
- [73] R. Baier, S. A. Stricker and O. Taanila, *Critical scalar field collapse in  $AdS_3$ : an analytical approach*, *Class. Quant. Grav.* **31** (2014) 025007, [[1309.1629](#)].
- [74] G. Clément and A. Fabbri, *Comment on “Critical scalar field collapse in  $AdS_3$ : an analytical approach”*, *Class. Quant. Grav.* **31** (2014) 098001, [[1401.4093](#)].
- [75] B. Freivogel and I.-S. Yang, *Coherent Cascade Conjecture for Collapsing Solutions in Global  $AdS$* , *Phys. Rev.* **D93** (2016) 103007, [[1512.04383](#)].
- [76] O. Evnin and R. Nivesvivat,  *$AdS$  perturbations, isometries, selection rules and the Higgs oscillator*, *JHEP* **01** (2016) 151, [[1512.00349](#)].
- [77] D. S. Menon and V. Suneeta, *Necessary conditions for an  $AdS$ -type instability*, *Phys. Rev.* **D93** (2016) 024044, [[1509.00232](#)].
- [78] B. Craps, O. Evnin and J. Vanhoof, *Renormalization, averaging, conservation laws and  $AdS$  (in)stability*, *JHEP* **01** (2015) 108, [[1412.3249](#)].
- [79] A. Buchel, S. R. Green, L. Lehner and S. L. Liebling, *Conserved quantities and dual turbulent cascades in anti-de Sitter spacetime*, *Phys. Rev.* **D91** (2015) 064026, [[1412.4761](#)].
- [80] B. Craps and O. Evnin,  *$AdS$  (in)stability: an analytic approach*, *Fortsch. Phys.* **64** (2016) 336–344, [[1510.07836](#)].
- [81] P. Bizoń and A. Rostworowski, *Comment on “Holographic Thermalization, Stability of Anti-de Sitter Space, and the Fermi-Pasta-Ulam Paradox”*, *Phys. Rev. Lett.* **115** (2015) 049101, [[1410.2631](#)].
- [82] S. R. Green, A. Maillard, L. Lehner and S. L. Liebling, *Islands of stability and recurrence times in  $AdS$* , *Phys. Rev.* **D92** (2015) 084001, [[1507.08261](#)].

- [83] S. L. Liebling and G. Khanna, *Scalar collapse in AdS with an OpenCL open source code*, *Class. Quant. Grav.* **34** (2017) 205012, [[1706.07413](#)].
- [84] B. Cownden, N. Deppe and A. R. Frey, In preparation, (2020) .
- [85] H. Okawa, J. C. Lopes and V. Cardoso, *Collapse of massive fields in anti-de Sitter spacetime*, [1504.05203](#).
- [86] B. Cownden, N. Deppe and A. R. Frey, *Phase Diagram of Stability for Massive Scalars in Anti-de Sitter Spacetime*, [1711.00454](#).
- [87] M. Maliborski and A. Rostworowski, *What drives AdS spacetime unstable?*, *Phys. Rev.* **D89** (2014) 124006, [[1403.5434](#)].
- [88] M. Choptuik, J. E. Santos and B. Way, *Charting Islands of Stability with Multioscillators in anti-de Sitter space*, *Phys. Rev. Lett.* **121** (2018) 021103, [[1803.02830](#)].
- [89] R. Masachs and B. Way, *New islands of stability with double-trace deformations*, *Phys. Rev.* **D100** (2019) 106017, [[1908.02296](#)].
- [90] J. A. Wheeler, *Geons*, *Phys. Rev.* **97** (1955) 511–536.
- [91] O. J. C. Dias, G. T. Horowitz and J. E. Santos, *Gravitational Turbulent Instability of Anti-de Sitter Space*, *Class. Quant. Grav.* **29** (2012) 194002, [[1109.1825](#)].
- [92] G. Martinon, G. Fodor, P. Grandclément and P. Forgàcs, *Gravitational geons in asymptotically anti-de Sitter spacetimes*, *Class. Quant. Grav.* **34** (2017) 125012, [[1701.09100](#)].
- [93] A. Rostworowski, *Higher order perturbations of Anti-de Sitter space and time-periodic solutions of vacuum Einstein equations*, *Phys. Rev.* **D95** (2017) 124043, [[1701.07804](#)].
- [94] G. T. Horowitz and J. E. Santos, *Geons and the Instability of Anti-de Sitter Spacetime*, *Surveys Diff. Geom.* **20** (2015) 321–335, [[1408.5906](#)].
- [95] X. Wen and J.-Q. Wu, *Floquet conformal field theory*, [1805.00031](#).

- [96] A. Baumgartner and M. Spillane, *Phase transitions and conductivities of Floquet fluids*, *JHEP* **09** (2018) 082, [[1802.05285](#)].
- [97] P. Carracedo, J. Mas, D. Musso and A. Serantes, *Adiabatic pumping solutions in global AdS*, *JHEP* **05** (2017) 141, [[1612.07701](#)].
- [98] A. Biasi, P. Carracedo, J. Mas, D. Musso and A. Serantes, *Floquet Scalar Dynamics in Global AdS*, *JHEP* **04** (2018) 137, [[1712.07637](#)].
- [99] R. Auzzi, S. Elitzur, S. B. Gudnason and E. Rabinovici, *Time-dependent stabilization in AdS/CFT*, *JHEP* **08** (2012) 035, [[1206.2902](#)].
- [100] R. Auzzi, S. Elitzur, S. B. Gudnason and E. Rabinovici, *On periodically driven AdS/CFT*, *JHEP* **11** (2013) 016, [[1308.2132](#)].
- [101] N. Deppe, A. Kolly, A. Frey and G. Kunstatter, *Stability of AdS in Einstein Gauss Bonnet Gravity*, *Phys. Rev. Lett.* **114** (2015) 071102, [[1410.1869](#)].
- [102] P. Basu, C. Krishnan and A. Saurabh, *A stochasticity threshold in holography and the instability of AdS*, *Int. J. Mod. Phys. A* **30** (2015) 1550128, [[1408.0624](#)].
- [103] F. V. Dimitrakopoulos, B. Freivogel, M. Lippert and I.-S. Yang, *Position space analysis of the AdS (in)stability problem*, *JHEP* **08** (2015) 077, [[1410.1880](#)].
- [104] O. Evnin and C. Krishnan, *A Hidden Symmetry of AdS Resonances*, *Phys. Rev. D* **91** (2015) 126010, [[1502.03749](#)].
- [105] F. Dimitrakopoulos and I.-S. Yang, *Conditionally extended validity of perturbation theory: Persistence of AdS stability islands*, *Phys. Rev. D* **92** (2015) 083013, [[1507.02684](#)].
- [106] B. Craps, O. Evnin and J. Vanhoof, *Ultraviolet asymptotics and singular dynamics of AdS perturbations*, *JHEP* **10** (2015) 079, [[1508.04943](#)].
- [107] B. Craps, O. Evnin, P. Jai-akson and J. Vanhoof, *Ultraviolet asymptotics for quasiperiodic AdS<sub>4</sub> perturbations*, *JHEP* **10** (2015) 080, [[1508.05474](#)].

- [108] M. Maliborski and A. Rostworowski, *A comment on “Boson stars in AdS”*, [\[1307.2875\]](#).
- [109] M. Maliborski and A. Rostworowski, *Lecture Notes on Turbulent Instability of Anti-de Sitter Spacetime*, *Int. J. Mod. Phys. A* **28** (2013) 1340020, [\[1308.1235\]](#).
- [110] P. Bizoń, M. Maliborski and A. Rostworowski, *Resonant Dynamics and the Instability of Anti-de Sitter Spacetime*, *Phys. Rev. Lett.* **115** (2015) 081103, [\[1506.03519\]](#).
- [111] N. Deppe, *On the stability of anti-de Sitter spacetime*, *Phys. Rev. D* **100** (2019) 124028, [\[1606.02712\]](#).
- [112] F. V. Dimitrakopoulos, B. Freivogel, J. F. Pedraza and I.-S. Yang, *Gauge dependence of the AdS instability problem*, *Phys. Rev. D* **94** (2016) 124008, [\[1607.08094\]](#).
- [113] F. V. Dimitrakopoulos, B. Freivogel and J. F. Pedraza, *Fast and Slow Coherent Cascades in Anti-de Sitter Spacetime*, *Class. Quant. Grav.* **35** (2018) 125008, [\[1612.04758\]](#).
- [114] N. Deppe, A. Kolly, A. R. Frey and G. Kunstatter, *Black Hole Formation in AdS Einstein-Gauss-Bonnet Gravity*, *JHEP* **10** (2016) 087, [\[1608.05402\]](#).
- [115] R. Arias, J. Mas and A. Serantes, *Stability of charged global  $AdS_4$  spacetimes*, *JHEP* **09** (2016) 024, [\[1606.00830\]](#).
- [116] V. E. Hubeny and M. Rangamani, *Unstable horizons*, *JHEP* **05** (2002) 027, [\[hep-th/0202189\]](#).
- [117] A. Buchel and L. Lehner, *Small black holes in  $AdS_5 \times S^5$* , *Class. Quant. Grav.* **32** (2015) 145003, [\[1502.01574\]](#).
- [118] A. Buchel, *Universality of small black hole instability in  $AdS/CFT$* , *Int. J. Mod. Phys. D* **26** (2017) 1750140, [\[1509.07780\]](#).
- [119] A. Buchel and M. Buchel, *On stability of nonthermal states in strongly coupled gauge theories*, [\[1509.00774\]](#).

- [120] R. Brito, V. Cardoso and J. V. Rocha, *Interacting shells in AdS spacetime and chaos*, *Phys. Rev.* **D94** (2016) 024003, [[1602.03535](#)].
- [121] H. P. de Oliveira, L. A. Pando Zayas and C. A. Terrero-Escalante, *Turbulence and Chaos in Anti-de-Sitter Gravity*, *Int. J. Mod. Phys.* **D21** (2012) 1242013, [[1205.3232](#)].
- [122] H. Năstase, *Introduction to the ADS/CFT Correspondence*. Cambridge University Press, 2015.
- [123] P. R. Brady, C. M. Chambers and S. M. C. V. Goncalves, *Phases of massive scalar field collapse*, *Phys. Rev.* **D56** (1997) 6057–6061, [[gr-qc/9709014](#)].
- [124] D. Santos-Oliván and C. F. Sopuerta, *Moving closer to the collapse of a massless scalar field in spherically symmetric anti-de Sitter spacetimes*, *Phys. Rev.* **D93** (2016) 104002, [[1603.03613](#)].
- [125] G. Martinon, *The instability of anti-de Sitter space-time*, [1708.05600](#).
- [126] J. Jałmużna, C. Gundlach and T. Chmaj, *Scalar field critical collapse in 2+1 dimensions*, *Phys. Rev.* **D92** (2015) 124044, [[1510.02592](#)].
- [127] P. Bizoń, *Is AdS stable?*, *Gen. Rel. Grav.* **46** (2014) 1724, [[1312.5544](#)].
- [128] M. W. Choptuik, O. J. C. Dias, J. E. Santos and B. Way, *Collapse and Nonlinear Instability of AdS Space with Angular Momentum*, *Phys. Rev. Lett.* **119** (2017) 191104, [[1706.06101](#)].
- [129] Y. Nakayama, *Holographic interpretation of renormalization group approach to singular perturbations in nonlinear differential equations*, *Phys. Rev.* **D88** (2013) 105006, [[1305.4117](#)].
- [130] F. V. Dimitrakopoulos, B. Freivogel and J. F. Pedraza, *Fast and Slow Coherent Cascades in Anti-de Sitter Spacetime*, [1612.04758](#).
- [131] O. Evnin and P. Jai-akson, *Detailed ultraviolet asymptotics for AdS scalar field perturbations*, *JHEP* **04** (2016) 054, [[1602.05859](#)].

- [132] M. Rangamani, M. Rozali and A. Wong, *Driven Holographic CFTs*, *JHEP* **04** (2015) 093, [[1502.05726](#)].
- [133] R. C. Myers, M. Rozali and B. Way, *Holographic Quenches in a Confined Phase*, *J. Phys. A* **50** (2017) 494002, [[1706.02438](#)].
- [134] A. Biasi, B. Craps and O. Evnin, *Energy returns in global  $AdS_4$* , [1810.04753](#).